Advances in Materials Science and Engineering

Metal Science: Multiscale Modeling, Simulation and Application

Lead Guest Editor: Liancheng Zhao
Guest Editors: David Mooney and Lan Huang

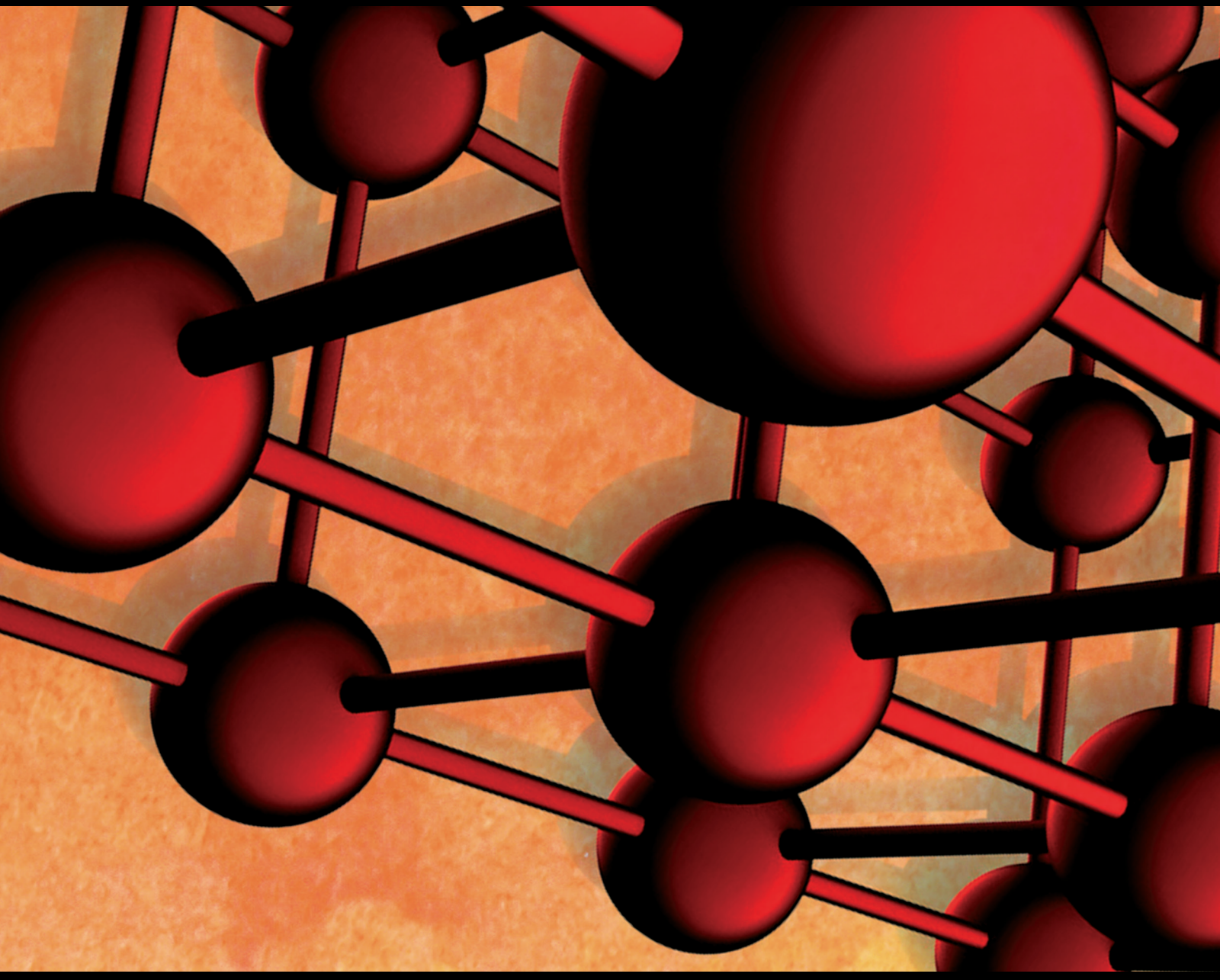

Metal Science: Multiscale Modeling, Simulation and Application

Advances in Materials Science and Engineering

Metal Science: Multiscale Modeling, Simulation and Application

Lead Guest Editor: Liancheng Zhao
Guest Editors: David Mooney and Lan Huang

Contents

Hindawi
Advances in Materials Science and Engineering
Volume 2023, Article ID 5952072, 16 pages
https://doi.org/10.1155/2023/5952072

Research Article

Prediction of Mechanical Properties of Aluminium Alloy Strip Using the Extreme Learning Machine Model Optimized by the Gray Wolf Algorithm

Zhenqiang Xiong, Jiadong Li, Peng Zhao, and Yong Li

The State Key Laboratory of Rolling and Automation, Northeastern University, Shenyang 110819, China

Correspondence should be addressed to Jiadong Li; lijd@ral.neu.edu.cn

Received 21 September 2022; Revised 15 April 2023; Accepted 12 May 2023; Published 4 July 2023

Academic Editor: Alicia E. Ares

Mechanical properties are important indicators for evaluating the quality of strips. This paper proposes a mechanical performance prediction model based on the Gray Wolf Optimization (GWO) algorithm and the Extreme Learning Machine (ELM) algorithm. In the modeling process, GWO is used to determine the optimal weights and deviations of ELM and experiments are used to determine the model's key parameters. The model effectively avoids manual intervention and significantly improves aluminum alloy strips' mechanical property prediction accuracy. This paper uses processed data from the aluminum alloy production plant of Shandong Nanshan Aluminum Co., Ltd. as experimental data. When the prediction deviation is controlled within ±10%, the GWO-ELM model can achieve a correct rate of 100% for tensile strength, 97.5% for yield strength, and 77.5% for elongation on the test set. The RMSE of the tensile strength, yield strength, and elongation of the GWO-ELM model was 5.365, 11.881, and 1.268, respectively. The experimental results show that the GWO-ELM model has higher accuracy and stability in predicting aluminum alloy strips' tensile strength, yield strength, and elongation. The GWO-ELM model effectively avoids the defects of the traditional model. It has a special guiding significance for producing aluminum alloy strips.

1. Introduction

Among the many indicators of hot-rolled alloy products, mechanical properties, which are influenced by the complexity of processing parameters, are one of the important indicators of the quality of hot-rolled alloy products. Therefore, the mechanical properties of alloy products are valued by many manufacturers and researchers. Accurate prediction of the mechanical properties of hot-rolled aluminium alloys has become one of the hot topics in the development and application of aluminium alloys [1, 2]. Up to now, there are two main models in the field of metal property prediction. One of them is the construction of material constitutive models for material property prediction [3]. Jia et al. [4] used experimentally obtained stress-strain data to calculate the material constants involved in the Arrhenius-type constitutive model and the modified Zerilli–Armstrong (MZA) model. Zhang et al. [5] established the constitutive model for the thermal deformation behavior of high-strength aluminium alloy (Al-Zn-Mg-Cu). The results show that the constitutive model can accurately predict the flow behavior of the Al-Zn-Mg-Cu alloy. Although the emergence of the constitutive model enables researchers to reasonably predict the product performance according to the processing technology, the construction of the constitutive model still needs experimental support and reasonable assumptions, which leads to the fact that the constitutive model cannot fully meet the requirements of industrialization. To meet the needs of industrial production, another model emerged along with the maturity of computer technology, which uses intelligent algorithms to analyze large amounts of real production data to obtain more desirable predictions of mechanical properties. Along with the development of computer technology, artificial

intelligence algorithms play an increasingly important role in materials' research. Various machine learning algorithms applied to materials' research have solved many challenging problems [6]. The combination of computer technology and materials' science will likely yield more important achievements in the foreseeable future [7]. Guo et al. [8] proposed a method for multiproperty prediction of materials using the Interior Point Algorithm. The rationality and reliability of the above theory are verified successfully by the experiment using the data of the steel production process. Among the many machine learning algorithms on which statistical models rely, neural network-like algorithms are favored and widely used in the field of material property prediction due to their excellent properties [9, 10]. Niklas et al. [11] needed to develop accurate models to ensure efficient control equipment for superelastic shape memory alloys (SMA). After training, the ANN can successfully calculate model parameters from cyclic tensile stress-strain tests, thereby improving the efficiency of SMA control devices. Lan et al. [12] experimentally established a dataset of the chemical composition, processing parameters, and mechanical properties of the A380 alloy. The Fe/Mn content ratio, Sr content, cooling rate, and porosity content were the input variables, and ultimate tensile strength (UTS) and elongation (El) were used as output parameters. Two ANN models were developed, namely, (1) a back propagation artificial neural network (BP-ANN) model and (2) a back propagation artificial neural network model for particle swarm optimization (PSO-BP-ANN). The results show that the established PSO-BP-ANN model has better reliability and prediction accuracy than the BP-ANN model. Wu et al. [13] established an ANN model to predict the bending deformation in welded thin-walled aluminium alloy tube structures. The model's input variables include the four controllable position parameters of the weld, while the target output is the bending distortion in the x- and y-axis directions. A supervised multilayer feedforward back propagation (BP) neural network is proposed to estimate the bending distortion quickly and accurately. The predicted values of the designed BP neural network are compared with the finite element simulation results. The results show that the proposed BP neural network model can accurately predict the bending distortion caused by welding over a range of welding position parameters. Jaafreh et al. [14] used a multiobjective evolution (MOE) algorithm and machine learning techniques to predict the age-hardening behavior of aluminium alloy under various machining conditions. The results showed that combining the MOE algorithm and the machine learning process can successfully refine features and construct accurate machine learning prediction models compared to other feature selection and preprocessing methods. Sun et al. [15] used ANN methods to develop a correlation model between the thermal processing parameters and mechanical properties of Ti-6Al-4V alloy based on a series of forging and heat treatment experimental data. The correlation model was developed using the ANN method. The results show a reliable correlation between the process parameters and the mechanical properties of the Ti-6Al-4V alloy. Aykut et al. [16] improved the experimental model of surface roughness using ANN and response surface methodology (RSM).

ANN is widely used in various fields of material research [17, 18], but ANN is very time-consuming in the training process. To overcome this shortcoming, the ELM algorithm is proposed. ELM, an emerging single hidden layer neural network algorithm [19], has received attention in material property prediction research due to its fast learning speed and high generalization capability. Cao et al. [20] used ELM optimized by the genetic algorithm (GA) with other numerical models (including finite element model simulation) to determine the critical dimensions of prefabricated gear blanks with complex geometry for comparative analysis. The results showed that the GA-ELM and R-GPLVM predictions were in good agreement with the experimental results. Sui and Lv [21] combined the ELM algorithm-based model with an attribute reduction method. With the attribute reduction method combining information entropy and Gram–Schmidt orthogonal transformation, the process parameters that can effectively affect quality were selected to form a subset of features. Compared with traditional modelling methods, the model has the advantages of a simple structure, low time consumption, and high prediction accuracy. The prediction results show that the model has better adaptability to complex hot rolling processes, and the prediction performance is better than that of the traditional ELM model. Liu et al. [22] proposed a rolling force prediction method based on GA, PSO, and multihidden layer extreme learning machine (MELM), namely, the PSO-GA-MELM algorithm, which uses MELM as the primary model for rolling force prediction. In the modelling process, a genetic algorithm is used to determine the optimal number of hidden layers and nodes and a particle swarm algorithm is used to search for the optimal input weights and biases. Experimental results show that the rolling force prediction model trained by the algorithm has an excellent performance in prediction accuracy and can be used for the prediction of rolling force in the hot strip rolling process.

Although machine learning models, especially neural network type models, have been widely used in the study of steel materials, there has been little research in the prediction of mechanical properties of aluminium alloy materials. The main objective of this study is to develop an optimised ELM model that can accurately predict the mechanical properties of aluminium alloy strips. Firstly, the model is built using a dataset obtained from an aluminium alloy strip production line. Secondly, the ELM model was optimised using the GWO algorithm. Finally, a comparative analysis of the accuracy of the model was carried out. The experimental results show that the model is feasible to be applied to the prediction of mechanical properties of aluminium alloy strips.

2. A Brief Introduction to MGWO, GWO, and ELM

2.1. ELM Algorithm. ELM was born in 2004 to overcome the limitation of the complex and slow iterative structure of traditional neural networks. ELM's single hidden layer

feedforward neural network randomly selects the weights and biases of the number of hidden nodes. ELM has received a lot of attention from scholars since its introduction because, compared with traditional neural networks, ELM as single hidden layer feedforward neural networks (SLFNs) can have faster iteration speed and better generalization while ensuring accuracy [16]. The algorithm principle of ELM algorithm is shown in equations (1)–(7) [19]. The structure of the ELM algorithm is illustrated in Figure 1.

As illustrated in Figure 1, we suppose that there exist N samples (X_i, t_i), where $X_i = [x_{i1}, x_{i2}, x_{i3}, \ldots, x_{in},]^T \in R^n$, $t_i = [t_{i1}, t_{i2}, t_{i3}, \ldots, t_{im},]^T \in R^m$, when the neural network has a hidden layer while that hidden layer has L hidden layer neurons, the output value of the neural network can be expressed as follows:

$$f_L(X_j) = \sum_{i=1}^{L} \beta_i g(W_i \bullet X_j + b_i), j = 1, 2, 3, \cdots, N, \quad (1)$$

where β_i is the output weight between the first i output weight between the neuron in the hidden layer and the neuron in the output layer, $g(\bullet)$ is the activation function, and $g(W_i \bullet X_j + b_i)$ represents the input parameter X_j of the output of the first i output of the hidden layer neuron. $W_i = [w_{i1}, w_{i2}, w_{i3,} \ldots, w_{in}]^T$ is the input weight between the first i input weight between the first input neuron and the hidden layer neuron, and b_i is the output bias of the first i output bias of the first hidden layer neuron, and $W_i \bullet X_j$ denotes W_i as the inner product of X_j of the inner product.

The smaller the error between the predicted and measured values of a single hidden layer neural network, the more accurate the model's prediction results, as shown in the following equation:

$$\sum_{j=1}^{N} \left\| f_L(X_j) - t_j \right\| = 0, \quad (2)$$

i.e., parameters $\beta_i W_i$ and b_i exist as shown in the following equation:

$$f_L(X_j) = \sum_{i=1}^{L} \beta_i g(W_i \bullet X_j + b_i) = t_j, j = 1, 2, 3, \cdots, N. \quad (3)$$

In the matrix form, this can be expressed as shown in the following equation:

$$H\beta = T, \quad (4)$$

of which $H(W_1, W_2, \cdots, W_L, b_1, b_2, \cdots, b_L, X_1, X_2, \cdots, X_L) = \begin{bmatrix} g(W_1 \bullet X_1 + b_1) & \cdots & g(W_L \bullet X_1 + b_L) \\ \vdots & \ddots & \vdots \\ g(W_1 \bullet X_N + b_1) & \cdots & g(W_L \bullet X_N + b_L) \end{bmatrix}_{N \times L}$, $\beta = \begin{bmatrix} \beta_1^T \\ \vdots \\ \beta_L^T \end{bmatrix}_{L \times m}$, $T = \begin{bmatrix} T_1^T \\ \vdots \\ T_L^T \end{bmatrix}_{N \times m}$, H represents the output of the nodes in the hidden layer, and β represents the output weights from the hidden layer to the output layer. T represents the desired output value with high prediction accuracy. As shown in equation (5), to obtain a single hidden layer neural network with the desired prediction accuracy, the parameters β^*, W^*, and b^* are desired to be obtained.

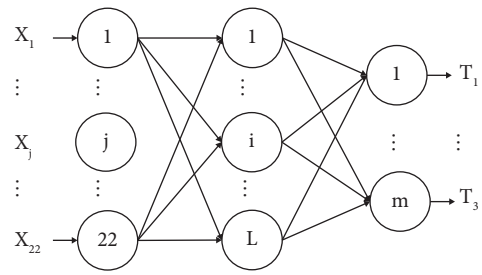

Figure 1: Network structure of the ELM algorithm.

$$\left\| H(W^*, b^*, X_i)\beta^* - T \right\| = \min_{W,b,\beta} \left\| H(W_i, b_i, X_i)\beta_i - T \right\|, \quad (5)$$

where $i = 1, 2, 3, \cdots, L$, is equivalent to making the loss function J obtain its minimum value, as shown in the following equation:

$$J = \min_{W,b,\beta} \sum_{j=1}^{N} \left(\sum_{i=1}^{L} \beta_i g(W_i \bullet X_j + b_i) - t_j \right)^2. \quad (6)$$

The process of training a single hidden layer neural network can be transformed into solving $H\beta = T$, which can solve for the matrix H of the Moore–Penrose generalized inverse matrix $H^\dagger$. Due to the characteristics of the ELM itself, i.e., the input weights W_i and the hidden layer bias b_i are determined randomly. Once the input weights W_i and hidden layer bias b_i are determined, the output matrix of the hidden layer H is uniquely determined. At this point, $H^\dagger$ is the matrix H of the Moore–Penrose generalized inverse, as shown in the following equation:

$$\beta^* = H^\dagger T. \quad (7)$$

2.2. GWO Algorithm. The GWO algorithm is inspired by the hunting behavior of the grey wolf pack and is designed to simulate the group collaboration behavior of the grey wolf pack in the process of predation to achieve the purpose of optimization [23]. The GWO algorithm has an adaptive convergence factor and a feedback mechanism that allows it to avoid falling into the trap of local optimality in the global search process. It, therefore, has higher accuracy and robustness in the problem-solving process.

The grey wolf is a canine predator that prefers to live in packs, with a clear hierarchical division of labor among its members during the hunt. The hierarchical distribution of the grey wolf population is similar to the pyramid's structure, as shown in Figure 2. The pack's leader is located at the first level of the pyramid and is called α. The think tank team of the pack at the second level of the pyramid is called β. β is second only to α in terms of leadership in the pack, and when there is a vacancy in α's position in the pack, β will fill the vacant position and become the new α. The executors of the pack are located at the third level of the pyramid and are

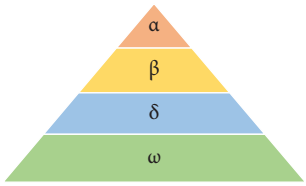

Figure 2: Hierarchy chart of the grey wolf population.

called δ. The wolves at the bottom of the pyramid are called ω and are responsible for executing $\alpha\beta$ and δ's commands. The strict hierarchical distribution is directly reflected in the hunting activities of the grey wolf, which will be led by α. During the hunting process, $\alpha\beta\delta$ and ω will strictly follow their duties and have a clear division of labor and the hunting process can be divided into three main steps, namely, finding and surrounding the prey; harassing and tracking the prey; and attacking the prey.

The algorithm principle of the GWO algorithm is shown in equations (8)–(15) [23]. The grey wolf optimization algorithm abstracts the hunting pattern of a wolf pack into an optimization algorithm. In the process of finding and encircling prey, the grey wolf's process of encircling prey is defined in equations (8) and (9) as follows. Equation (8) represents the distance between the grey wolf and the prey. Here, $\vec{D}$ represents the direction and distance travelled by individual grey wolves. $\vec{C}$ is the parameter used to determine the direction of the wolf pack's search for prey, t represents the number of iterations of grey wolf positions, and $\vec{X}_P(t)$ represents the position that individual grey wolves tend to approach. $\vec{X}(t)$ represents the position of the individual grey wolf when the iteration number is t. Equation (9) represents the iterative formula for the position of the grey wolf, and $\vec{A}$ is the parameter used to adjust the radius of the prey search. $\vec{A}$ and $\vec{C}$ calculation formulas are shown in equations (10) and (11). a is the convergence factor, as shown in equation (12), and a decreases from a maximum value of 2 until it becomes 0 as the number of iterations increases. $\vec{r_1}$ with $\vec{r_2}$ is a random vector with the modulus length set in the range [0, 1].

$$\vec{D} = \left|\vec{C} \bullet \vec{X}_P(t) - \vec{X}(t)\right|, \tag{8}$$

$$\vec{X}(t+1) = \vec{X}_P(t) - \vec{A} \bullet \vec{D}, \tag{9}$$

$$\vec{A} = 2a \bullet \vec{r_1} - a, \tag{10}$$

$$\vec{C} = 2\vec{r_2}, \tag{11}$$

$$a = 2 - \frac{2t}{t_{\max}}. \tag{12}$$

In the practical application of the optimization algorithm, the optimal three solutions are assigned to α, β, and δ according to their fitness, making $\alpha\beta\delta$ the leader of the pack closest to the prey. In turn, the other grey wolves adjust their positions according to the best-positioned grey wolf, calculate their fitness after the position update, and rerank the grey wolves according to their fitness size. The mechanism for individuals in the pack to update their positions is shown in Figure 3. The mathematical model of individual grey wolves updating their positions can be shown as equation (13). Here, $\vec{D}_\alpha \vec{D}_\beta \vec{D}_\delta$ represents the distance relationship between α and β δ individuals and other individuals, respectively, $\vec{X}_\alpha \vec{X}_\beta \vec{X}_\delta$ represents, respectively, the $\alpha\beta\delta$ the current position of the individual, $\vec{C}_1 \vec{C}_2 \vec{C}_3$ represents a random vector, and $\vec{X}$ represents the current position of an individual grey wolf. In a wolf pack ω, the distance and direction of the individual to the target are shown in equations (14) and (15).

$$\begin{cases} \vec{D}_\alpha = \left|\vec{C}_1 \bullet \vec{X}_\alpha - \vec{X}\right|, \\ \vec{D}_\beta = \left|\vec{C}_2 \bullet \vec{X}_\beta - \vec{X}\right|, \\ \vec{D}_\delta = \left|\vec{C}_3 \bullet \vec{X}_\delta - \vec{X}\right|, \end{cases} \tag{13}$$

$$\begin{cases} \vec{X}_1 = \left|\vec{X}_\alpha - A_1 \bullet \vec{D}_\alpha\right|, \\ \vec{X}_2 = \left|\vec{X}_\beta - A_2 \bullet \vec{D}_\beta\right|, \\ \vec{X}_3 = \left|\vec{X}_\delta - A_3 \bullet \vec{D}_\delta\right|, \end{cases} \tag{14}$$

$$\vec{X}(t+1) = \frac{\vec{X}_1 + \vec{X}_2 + \vec{X}_3}{3}. \tag{15}$$

From equations (10) and (12), the value of a will gradually decrease with the progress of iteration and the fluctuation range of parameter $\vec{A}$ will also decrease. The grey wolf algorithm uses the $|\vec{A}|$ and $\vec{C}$ to avoid the solution of the optimization algorithm falling into a local optimum. As shown in Figure 4(a), when $|\vec{A}| > 1$, the grey wolf individual moves away from the target, i.e., a global search is performed. As shown in Figure 4(b), when $|\vec{A}| < 1$, the individual grey wolf will launch a final attack on the prey, i.e., the optimal solution is obtained. From equation (11), it can be seen that C is a random value taking values in the interval [0, 2]. C represents the size of the hindrance for the grey wolf to approach the prey. $C > 1$ means that the grey wolf individual is not easy to approach the target; on the contrary, $C < 1$ means that the grey wolf individual is easy to approach the target and C can maintain randomness during the iterative process and helps the algorithm escape in time when it is about to fall into a local optimum trap. This algorithm feature also contributes to the ease with which the grey wolf optimization algorithm can obtain a global optimum.

2.3. MGWO Algorithm. The MGWO algorithm was proposed by Zhang and Zhou [24] in 2021. The algorithm considers that a with different update strategies can significantly affect the algorithm's performance [25]. The algorithm principle of the MGWO algorithm is shown in equations (16)–(18) [24]. It uses a convergence factor update based on regular exponential changes, as shown in equation (16). In addition, to enhance the balance between global search and local exploitation, the MGWO algorithm proposes a new adaptive shifting strategy [24, 26], whose

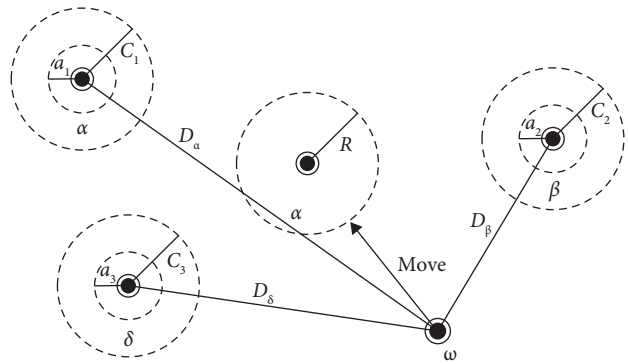

Figure 3: Schematic of the grey wolf location update for the grey wolf algorithm.

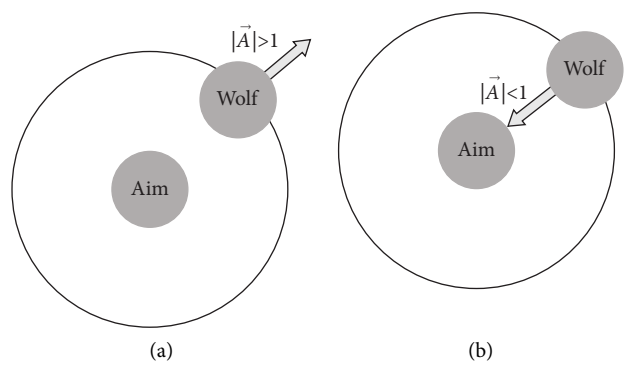

Figure 4: Individual grey wolves (a) moving away from their target and (b) attacking their prey.

mathematical expression is shown in equation (17). Here, the weights W_i of the mathematical expression are shown in equation (18).

$$a = 2e^{(-t/)}t_{\max}, \tag{16}$$

$$\vec{X}(t+1) = \frac{W_1\vec{X}_1 + W_2\vec{X}_2 + W_3\vec{X}_3}{3}\left(1 - \frac{t}{t_{\max}}\right) + \vec{X}_1\frac{t}{t_{\max}}, \tag{17}$$

$$W_i = \frac{\left|\overrightarrow{X_i}\right|}{\left|\overrightarrow{X_1}\right| + \left|\overrightarrow{X_2}\right| + \left|\overrightarrow{X_3}\right|}, \mathrm{i} = 1, 2, 3. \tag{18}$$

3. Proposed GWO-ELM Prediction Model

ELM is an effective mechanism for pattern classification and regression learning. In the ELM algorithm model, the number of hidden layer neurons needs to be determined in advance and the structure of the neural network has a direct impact on the accuracy of the ELM algorithm model, which relies on a large number of hidden layer nodes for good performance. As the number of nodes in the hidden layer increases, the computational cost increases significantly [27]. An excessive number of hidden layer neurons will make an ELM model so complex that it will slow down the prediction speed or even overfit. However, too few hidden layer neurons will result in an ELM model that does not achieve the desired accuracy. To date, there is no accepted and valid theory to guide the selection of the number of hidden layer neurons. In most cases, the determination of the number of hidden layer neurons relies on the experience of the model trainer to obtain the appropriate neural network parameters. If the essential parameters of the algorithm depend too much on manual selection, then the robustness of the model will be reduced. In addition, the weights and biases of the ELM model are randomly generated, which simplifies the algorithm but also has a significant negative impact on the algorithm's accuracy, as the randomness of the parameters makes the model's accuracy highly uncertain.

Mean Absolute Percentage Error (MAPE) mean square error (MSE) and root mean square error (RMSE) will be used to evaluate the performance of the model. The calculation methods of MAPE MSE RMSE and R^2 are shown in equations (19)–(22), respectively [15].

$$MAPE = \frac{100\%}{n}\sum_{i=1}^{n}\left|\frac{\dot{\hat{y}}_i - y_i}{y_i}\right|, \tag{19}$$

$$MSE = \frac{1}{n}\sum_{i=1}^{n}\left(\dot{\hat{y}}_i - y_i\right)^2, \tag{20}$$

$$RMSE = \sqrt{\frac{1}{n}\sum_{i=1}^{n}\left(\dot{\hat{y}}_i - y_i\right)^2}, \tag{21}$$

$$R^2 = \frac{SSR}{SST} = \frac{\sum_{i=1}^{n}\left(\dot{\hat{y}}_i - \overline{y}\right)^2}{\sum_{i=1}^{n}\left(y_i - \overline{y}\right)^2}, \tag{22}$$

where n represents the number of samples to be substituted into the formula for operation, $\dot{\hat{y}}_i$ represents the predicted value, y_i represents the actual value, and $\overline{y}$ represents the mean.

The suitable combination of the number of hidden layer neurons with the input weights and biases becomes the focus of improving the prediction accuracy of ELM. Therefore, this paper introduces the GWO algorithm to optimize the ELM algorithm, forming a new hybrid algorithm named GWO-ELM. The flow of the GWO-ELM algorithm is shown in Figure 5. In the modelling process of the GWO-ELM algorithm, the population size, objective function, and the maximum number of iterations of the GWO algorithm are first determined. Then, the optimal number of hidden layer neurons, the optimal input weights, and optimal bias of the ELM network are determined using the GWO algorithm. The GWO algorithm then determines the optimal number of hidden layer neurons, the optimal input weights, and the ELM network's optimal bias.

The specific steps of the GWO-ELM algorithm are as follows:

(1) We determine the input data. The raw data were preprocessed and randomly divided into training and test sets.

(2) We initialize the GWO algorithm and determine the number of grey wolves in the grey wolf algorithm population, the maximum number of iterations, and the number of parameters to be optimized. We determine the parameters A and C. We take $i = 0$.

(3) We initialize the weights and biases of the ELM, at which point the number of hidden layer neurons is no longer determined empirically but by experimental comparison. At this point, the number of hidden layer neurons is $L = i + 1$.

(4) We calculate the fitness of each individual in the pack to determine the best individual, in which MAPE is used as the individual's fitness. The smaller the error of an individual, the better it is. We determine α, β, δ, and ω in the wolf pack based on the individual error in the pack.

(5) We update the position and parameters of each grey wolf a A and C.

(6) We update the input weight ω and the bias b of the ELM model from the results of step (5) so that the parameters of the ELM model take values closer to the optimal values.

(7) We calculate the fitness of all grey wolves and update $\alpha\beta\delta$ and its fitness. The individual prediction error size determines that individual's leadership position in the wolf pack. That is, the $\alpha\beta\delta$ of wolves is determined according to the error of individual prediction values from small to large.

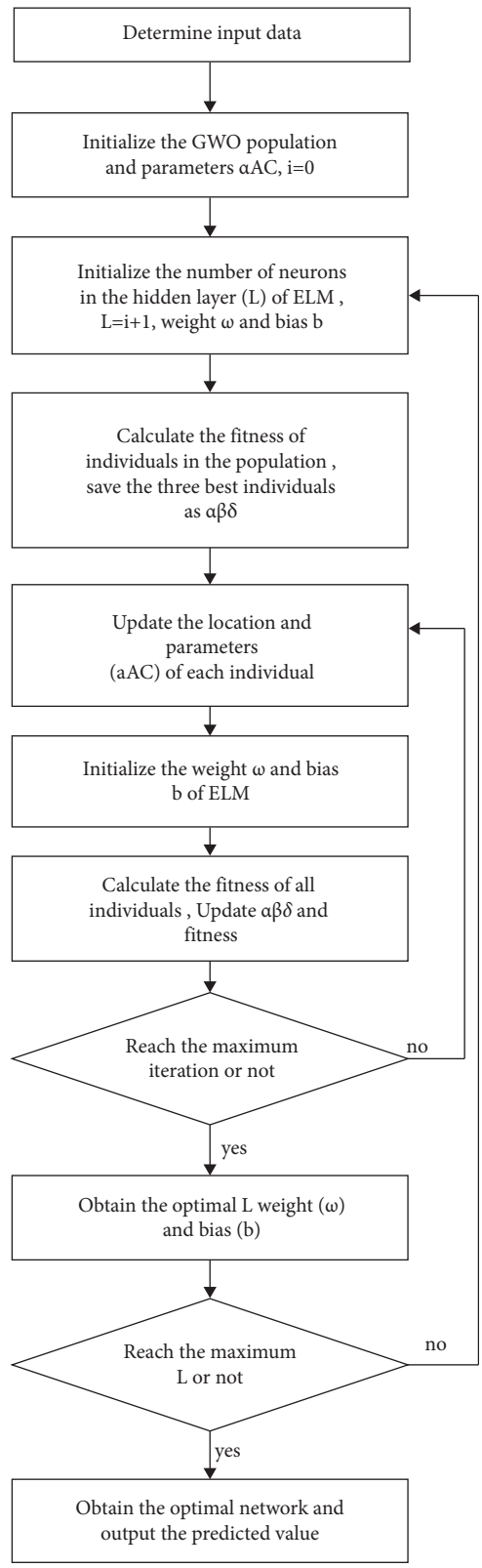

Figure 5: Flow chart of the GWO-ELM algorithm.

(8) We determine whether the maximum number of iterations is reached; if not, we return to step (5); otherwise, the optimal limit learning machine

structure is obtained when the number of neurons in the hidden layer is L.

(9) To determine whether L reaches the maximum number of hidden layer neurons. If it does not reach the maximum number of hidden layer neurons, step (3) is repeated; otherwise, the model's prediction accuracy can be compared when L takes different values. Finally, the optimal ELM network structure can be obtained.

4. Model Structure Building and Experimental Analysis

Extensive experiments were conducted to test the prediction accuracy of the proposed GWO-ELM model and compare and analyze the performance of the GWO-ELM model with that of the conventional ELM model and the MGWO-ELM model.

4.1. Acquisition and Processing of Training Samples. The prediction performance of the extreme learning machine is very dependent on the quality of the input data, and redundant or conflicting data will not result in the desired prediction accuracy [28]. High-quality data are the basis for establishing accurate models. This paper uses the actual production data of Shandong Nanshan Aluminum Industry Co., LTD, as experimental data. The data come from the big data platform database of the enterprise. This data are available and can be obtained as shown in the Data Availability section. The test standard number GB/T 16865-2013 was used to obtain data on material properties. In the experiments of this paper, the correlation between the input and output parameters was first analyzed using correlation analysis algorithms and physical metallurgy principles. Parameters with significant influence on tensile strength, yield strength, and elongation were selected as input parameters for the model, and a total of 22 input parameters were extracted. The input parameters of the model are shown in Table 1. This data are available and can be obtained as shown in the Data Availability section. The output parameters were set to tensile strength, yield strength, and elongation, and the output parameters are shown in Table 2. Table 1 shows the statistics for the mean, standard deviation, and minimum and maximum values for each input parameter. Table 2 shows each output parameter's mean, standard deviation, and minimum and maximum value statistics. After removing the outlier data for the initially identified parameters, the mean values were used to fill in the vacant values. The processed data will be used for model training and testing. A total of 131 production data sets on 6-series aluminium alloys and 5-series aluminium alloys were collected and applied. The main compositions of the aluminium alloys used for the data in this paper are shown in Table 3. Seventy percent of the total data (91 sets) will be assigned to the training set and used to train the model to have the desired prediction accuracy. The remaining data (40 sets) will be allocated to the test set to test the model's performance.

Data processing needs to avoid the adverse impact of the difference in the order of magnitude between different parameters on the prediction results, so the input parameters need to be normalized before input into the model. The input parameters need to be normalized before being fed into the model. The data normalization method is shown in equation (23), the input parameters will be normalized to [0, 1] [29]. Here, x represents the normalized data, $x_{\max}$ and $x_{\min}$ represent the maximum and minimum values of data in the dimension, respectively, and x_i represents the normalized result.

$$x_i = \frac{x - x_{\min}}{x_{\max} - x_{\min}}. \tag{23}$$

4.2. Determination of the Parameters of the GWO-ELM Algorithm. The network structure of the GWO-ELM model is closely related to the data structure. The dimensionality of the input determines the number of neurons in the input layer. The dimensionality of the output determines the number of neurons in the output layer. The input parameter is 22 dimensions, so the number of neurons in the input layer is set to 22; the output parameter is 3 dimensions, so the number of neurons in the output layer is set to 3. In the following experiment, 70% of the data will be used to train the model and the remaining 30% will be used to test the performance of the model. The entire simulation process in this experiment was carried out using Python 3.6. Firstly, the activation function was determined by the experiment [30]. The number of neurons in the hidden layer was tentatively set to 22 to test the model's prediction accuracy with different activation functions. The experimental results are shown in Table 4. The mean square error of the test set and the mean absolute percentage error of the test set were minimized when the activation function was "sigmoid." The mean squared error of the training set for the "sigmoid" activation function is 316.72, the mean squared error of the test set is 594.99, and the total mean squared error of the prediction is 401.68. The mean squared error of the training set for the "sigmoid" activation function and the mean absolute percentage error for the training set are 8.02, the mean absolute percentage error for the test set is 10.45, and the total mean absolute percentage error is 8.76. The ELM algorithm activation function is set to "sigmoid."

Next, experiments are used to determine the optimal number of hidden layer neurons for the ELM algorithm. The number of hidden layer neurons has a large impact on the prediction results of the ELM model, and too many or too few hidden layer neurons will decrease the model's prediction accuracy. In this section, the ELM activation function is "sigmoid" and the other parameters remain unchanged. The number of ELM hidden layer neurons was determined to be in the range [1, 38] based on the dimensionality of the input parameters used in this experiment. The performance of the ELM model with different numbers of hidden layer neurons was compared, and the results are shown in Figure 6. When the number of neurons in the hidden layer was less than 23, for tensile strength, yield

Table 1: Statistical information on input parameters.

Number	Parameter	Unit	Mean	Std	Min	Max
1	Machine speed	(m/min)	21.352	8.735	7.0	48.0
2	Heating temperature-1	(°C)	418.130	100.595	314.9	575.0
3	Heating temperature-2	(°C)	419.368	101.832	314.8	575.1
4	Heating temperature-3	(°C)	419.094	101.684	314.8	575.0
5	Heating temperature-4	(°C)	418.385	101.255	315.1	575.0
6	Heating temperature-5	(°C)	418.247	101.283	314.9	574.9
7	Heating temperature-6	(°C)	417.496	100.936	315.0	575.2
8	Heating temperature-7	(°C)	417.301	101.120	310.4	575.3
9	Heating temperature-8	(°C)	417.449	101.091	310.4	575.7
10	Heating temperature-9	(°C)	417.466	101.057	310.5	575.5
11	Heating temperature-10	(°C)	417.507	101.047	310.5	575.6
12	Heating temperature-11	(°C)	417.398	101.079	310.6	575.4
13	Heating temperature-12	(°C)	412.836	104.010	309.8	574.9
14	Elongation of tension bending straightening 1	(%)	0.312	0.454	0	1.0
15	Preageing temperature 1	(°C)	19.535	4.991	11.0	33.3
16	Preageing temperature 2	(°C)	19.973	5.46918	11.2	38.1
17	Preageing speed	(m/min)	22.267	8.290	8.0	49.0
18	Coiling tension	(N/mm^2)	12.008	0.488	7.0	13.0
19	Depression distance of tension bending straightening	(mm)	0.428	0.273	0.036	0.979
20	Pretension of tension bending straightening	(N/mm^2)	50.088	15.883	17.0	90.0
21	Post-tension of tension bending straightening	(N/mm^2)	50.088	15.883	17.0	90.0
22	Elongation of tension bending straightening 2	(%)	0.312	0.454	0	1.0

Table 2: Statistical information on output parameters.

Number	Parameter	Unit	Mean	Std	Min	Max
1	Tensile strength	MPa	263.789	43.507	204.000	338.667
2	Yield strength	MPa	212.830	61.052	93.667	309.500
3	Elongation	%	14.366	3.460	7.500	26.667

Table 3: Main components of aluminium alloy strip.

	Element	Al (%)	Mg (%)	Si (%)	Fe (%)	Cu (%)	Cr (%)	Mn (%)	Ti (%)	Ga (%)	Others (%)
Mass	6xxx	97.12	1.0122	0.6931	0.5564	0.2391	0.2301	0.084	0.025	0.0166	0.028
percentage	5xxx	94.37	4.7273	0.0969	0.2498	0.0674	0.0335	0.3961	0.0191	0.0141	0.022

Table 4: Comparison of different activation functions.

Name	MSE			MAPE		
	Train set	Test set	All	Train set	Test set	All
Sigmoid	316.72	594.99	401.68	8.02	10.45	8.76
tanh	498.75	1052.36	667.79	10.25	14.29	11.49
Linear	196.76	2544.63	913.65	7.55	13.10	9.25
rbf_l1	18150.11	22051.90	19341.50	49.48	52.97	50.54
rbf_l2	405.53	901.78	557.06	9.38	11.79	10.12

strength, and elongation, the prediction accuracy of the test set increased with the increase of the number of neurons. When the number of neurons in the hidden layer exceeds 23, especially the prediction accuracy of elongation, the prediction accuracy of the test set shows a trend of fluctuation decline. The reason for the previously mentioned phenomenon is that with the increase of the number of hidden layer neurons, the overfitting tendency of the model increases and the overfitting leads to the abnormal increase of the prediction error of the test set. As shown in Figure 6, the prediction accuracy reached its peak when the number of hidden layer neurons was 23.

Next, the population size of the grey wolf algorithm was determined by experiments. The number of iterations was set to 300, and the number of individuals in the population ranged from [10, 100]. The prediction results of the test set

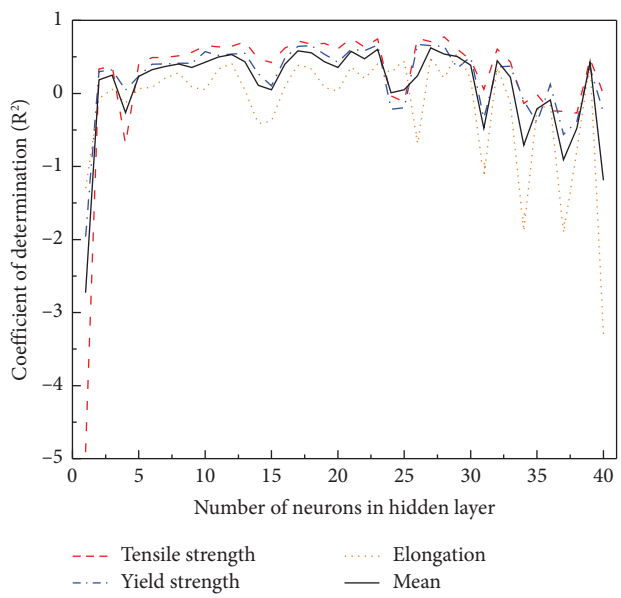

Figure 6: The prediction accuracy of the test set with the number of hidden layer neurons.

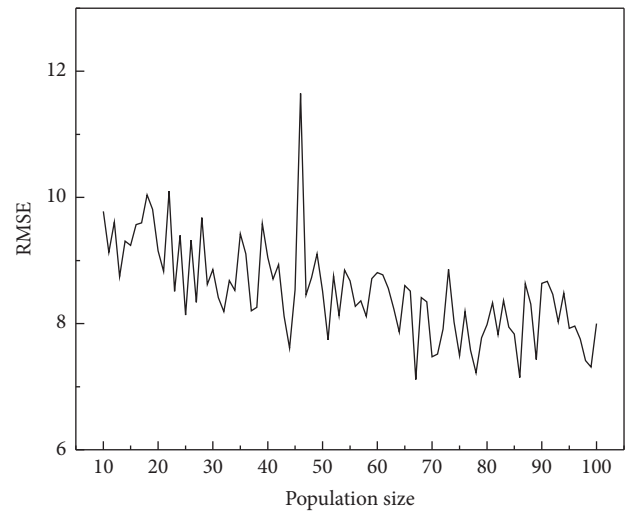

Figure 7: Population size and test set error trends.

with the number of iterations are shown in Figure 7. The prediction results of the test set showed low prediction errors when the population size was 67, 78, and 86. Still, too large population would cause the model training time to be extended, resulting in unnecessary time wastage.

The choice of objective function has a massive impact on the performance of the GWO algorithm. When the model is a multioutput algorithm, the influence of the weights between different objectives on the prediction accuracy of the final algorithm is of interest. To investigate the effect of the objective function weights on the mechanical properties of aluminium alloys, the objective function used in this paper is shown in equation (24). Here, P_T, P_Y, and P_E are the predicted values of tensile strength, yield strength, and elongation, respectively; E_T E_Y E_E are the measured values of tensile strength, yield strength, and elongation, respectively; N is the number of measured values; ji is the penalty coefficient of yield strength and elongation, respectively. The number of iterations of the GWO algorithm is set to 100, and the trends of tensile strength, yield strength, and elongation with the change of penalty coefficients are shown in Figure 8. As an example, Figure 8(a) shows the relationship between the MAPE error of tensile strength and the penalty coefficient. The closer the color was to dark, the smaller the MAPE error and the better the prediction accuracy. Different combinations of the penalty coefficient correspond to different prediction accuracies of mechanical properties. When the combination of penalty coefficients (i, j) is (20, 80), (90, 50), (60, 30), and (90, 80), the prediction error of tensile strength is small. Similarly, after comparing Figures 8(b) and 8(c), the penalty coefficient corresponding to the minimum prediction error of yield strength and elongation can be obtained. The prediction errors of yield strength and elongation of tensile strength are summarized. When the penalty coefficient (i, j) is (20, 80), the prediction errors of three mechanical properties are smaller at the same time.

The trend of variance of MAPE for the three output variables is shown in Figure 9, which indicates that when the penalty coefficients ji are 80 and 20, respectively, the corresponding MAPE variances for tensile strength, yield strength, and elongation are smaller. When the penalty coefficients are 80 and 20, respectively, the predicted values of tensile strength, yield strength, and elongation can maintain a balance of the predicted values of the three mechanical properties while ensuring a small accuracy of their own. The penalty coefficients in the objective function equation (23) ji are chosen as 80, 20. The comparison between the optimal penalty coefficient and the original coefficient is shown in Table 5. The optimal penalty coefficient can not only reduce the MAPE of the test set but also significantly reduce the variance of the prediction errors of the three variables. A lower variance means that the prediction error distribution of the three variables is more balanced.

$$P(P_T, P_Y, P_E) = \frac{1}{n}\left(\sum_{i=1}^{n}\left|\frac{P_T - E_T}{E_T}\right| + j \times \sum_{i=1}^{n}\left|\frac{P_Y - E_Y}{E_Y}\right| + i \times \sum_{i=1}^{n}\left|\frac{P_E - E_E}{E_E}\right|\right) \times 100\%, i, j = 1, 10, 20 \cdots 100. \quad (24)$$

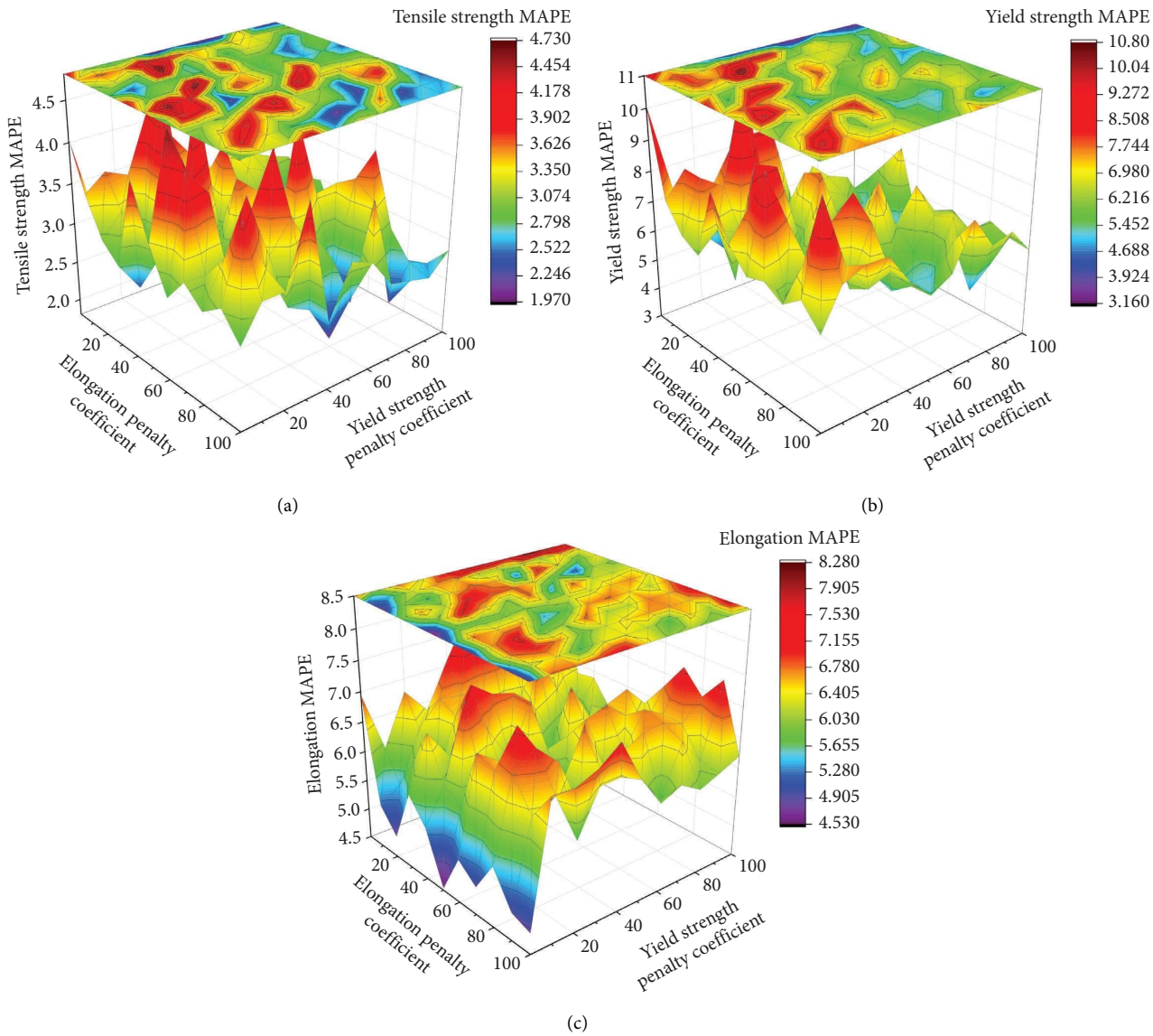

Figure 8: Trend of the test set MAPE with the penalty factors: (a) tensile strength, (b) yield strength, (c) and elongation.

The number of iterations of the GWO algorithm significantly impacts the prediction results, and each iteration will obtain a better value of the ELM algorithm parameters than the previous iteration. The GWO algorithm population size was set to 30, the fitness function was set to equation (24), and $i = 20$, $j = 80$. The relationship between the prediction accuracy of the GWO-ELM model test set and the number of iterations, as well as the model training time and the number of iterations, is shown in Figure 10. As the iterations proceeded, the R^2 of the test set increases gradually and the modelling time increased linearly with the number of iterations. When the number of iterations reaches 3150, the prediction accuracy of tensile strength, yield strength, and elongation converges.

In summary, the parameters of the GWO-ELM algorithm have been determined and are shown in Table 6. When the values of parameters are shown in Table 6, the iterative optimization of weight ω and bias b by the GWO algorithm can be realized. Thus, when the maximum number of iterations is reached, the optimal input weight ω and bias b of the ELM network in the GWO-ELM model are determined.

4.3. Experimentation and Evaluation of Model Performance. In this section, mechanical property prediction experiments demonstrate the excellent prediction accuracy of the proposed GWO-ELM model. The model comparison experiment of the GWO-ELM model, MGWO-ELM model, and traditional ELM model is designed to verify the advantages of the proposed GWO-ELM model. Each model was run through twenty replicates, and the results were averaged to avoid misleading results from model chance.

To ensure a fair comparison, the corresponding parameters for the GWO-ELM model and the ELM model in this experiment are shown in Table 6. The parameters used by the MGWO algorithm are consistent with the GWO

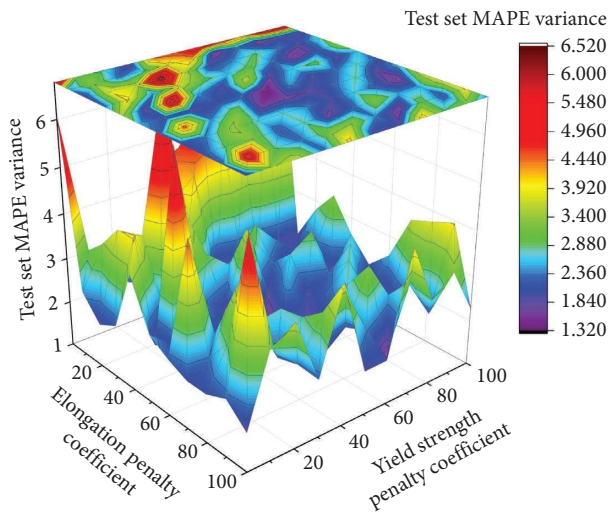

Figure 9: Trend of MAPE variance with the penalty coefficient for the test set of the three output variables.

Table 5: Optimal penalty factor vs. original factor.

i	j	Test set MAPE (%)			Train set MAPE (%)			Variance	
		Tensile strength	Yield strength	Elongation	Tensile strength	Yield strength	Elongation	Test set	Train set
1	1	4.04811	10.09929	6.94424	2.57422	6.30288	8.76849	6.107	6.483
20	80	3.17806	6.50873	6.41047	2.80229	6.35357	7.42699	2.395	3.906

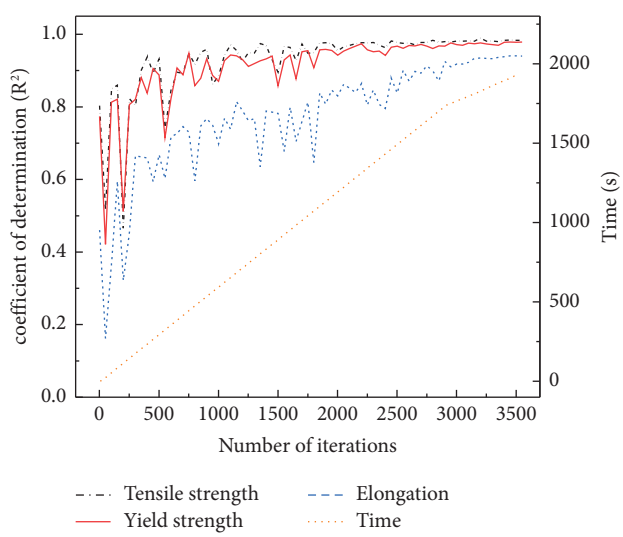

Figure 10: Prediction error and modeling time for the test set.

algorithm. MAPE and RMSE were error measures for the mechanical properties' prediction models. The prediction errors of the three models after twenty replicate experiments for the three mechanical properties are shown in Table 7. Table 7 provides an excellent visual representation of the prediction results of the GWO-ELM model, MGWO-ELM model, and ELM model for the three mechanical properties. In the test set, RMSE errors of tensile strength of the GWO-ELM model, MGWO-ELM model, and ELM model are 5.365, 11.557, and 21.489, respectively. The RMSE errors of yield strength in the GWO-ELM model, MGWO-ELM model, and ELM model are 11.881, 20.465, and 43.313, respectively. The RMSE errors of the elongation in the GWO-ELM model, MGWO-ELM model, and ELM model are 1.268, 1.848, and 5.360, respectively. The above-mentioned result indicates that the GWO-ELM model mentioned in this paper has a significantly higher prediction accuracy than the conventional ELM model for the three mechanical properties of tensile strength, yield strength, and elongation. The MGWO-ELM model outperforms the ELM

Table 6: Optimal parameter configuration for the GWO-ELM model.

Algorithm	Parameters	Configuration
GWO	Number of iterations	3150
	Population size	67
	Penalty coefficient [i, j]	[20, 80]
ELM	Number of neurons (input layer)	21
	Number of neurons (output layer)	3
	Number of neurons (hidden layer)	23
	Activation functions	Sigmoid

Table 7: Comparison of the predictive performance of the three models.

Mechanical properties	Name	RMSE		MAPE		R^2	
		Train set	Test set	Train set	Test set	Train set	Test set
Tensile strength	GWO-ELM	9.052	5.365	1.951	1.703	0.9549	0.9857
	MGWO-ELM	7.939	11.557	1.574	2.316	0.9534	0.9805
	ELM	10.976	21.489	2.702	5.317	0.9386	0.7102
Yield strength	GWO-ELM	15.499	11.881	4.204	2.703	0.9303	0.9662
	MGWO-ELM	16.795	20.465	4.225	5.185	0.9022	0.9804
	ELM	19.163	43.313	6.176	16.165	0.9053	0.3958
Elongation	GWO-ELM	1.424	1.268	7.371	5.994	0.7649	0.9141
	MGWO-ELM	1.355	1.845	6.937	9.244	0.8123	0.9074
	ELM	1.630	5.360	8.864	19.630	0.7384	−0.8312

model but is weaker than the GWO-ELM model. In the test set, for tensile strength, yield strength, and elongation, the MAPE of the GWO-ELM model is 1.703, 2.703, and 5.994 respectively, while the corresponding MAPE of the MGWO-ELM model is 2.316, 5.185, and 9.244 respectively, and that of the ELM model is 5.317, 16.165, and 19.630, respectively. The abovementioned result indicates that the average accuracy of the GWO-ELM model is significantly higher than that of the MGWO-ELM model for the three mechanical properties of tensile strength, yield strength, and elongation. R^2 was used as the evaluation index to evaluate the prediction results of the test set. The R^2 values of tensile strength in GWO-ELM, MGWO-ELM, and ELM models were 0.9857, 0.9805, and 0.7102, respectively. The R^2 values of yield strength in GWO-ELM, MGWO-ELM, and ELM models were 0.9662, 0.9804, and 0.3958, respectively. The R^2 values of elongation in GWO-ELM, MGWO-ELM, and ELM models were 0.9141, 0.9074, and −0.8312, respectively. The abovementioned results show that GWO-ELM and MGWO-ELM achieve an ideal fitting effect in the prediction of tensile strength, yield strength, and elongation, and the performance of the two models is far better than that of the ELM model. In addition, GWO-ELM was better than MGWO-ELM in the prediction of tensile strength and elongation, so the GWO-ELM model was slightly better than MGWO-ELM.

The predicted results of the GWO-ELM model, MGWO-ELM model, and ELM model compared to the actual values after twenty replicate experiments for the three mechanical properties are shown in Figure 11. Both in the training set and the test set, the prediction accuracy of the yield strength and elongation of the tensile strength is higher in the GWO-ELM model and the fit degree of the yield strength and elongation of the tensile strength is higher in the GWO-ELM model. The error distributions of the three model test sets are shown in Table 8. For the three mechanical properties of tensile strength, yield strength, and elongation, the GWO-ELM model has a more obvious advantage in the prediction results of the test set. This is especially true for the tensile and yield strengths. When the prediction deviation is controlled within ±10%, the prediction accuracy of tensile strength in the GWO-ELM model, MGWO-ELM model, and ELM model is 100%, 97.5%, and 80%, respectively. The prediction accuracy of yield strength of the GWO-ELM model, MGWO-ELM model, and ELM model is 97.5%, 92.5%, and 62.5%, respectively. The prediction accuracy of elongation in the GWO-ELM model, MGWO-ELM model, and ELM model is 77.5%, 77.5%, and 37.5%, respectively. Although the prediction accuracy of elongation of GWO-ELM and MGWO-ELM is the same when the error is controlled within ±10%, the prediction accuracy of the GWO-ELM model is better than that of MGWO-ELM when the prediction error is 5%. The abovementioned results indicate that the prediction accuracy of GWO-ELM is more stable than MGWO-ELM and ELM models.

In the prediction results of the test set, the absolute error distribution of the prediction results of tensile strength, yield strength, and elongation in different models is shown in Figure 12. As shown in Figure 12(a), the prediction error range of tensile strength in the GWO-ELM model is smaller than that of the other two models. As shown in Figure 12(b), the prediction error range of yield strength on the GWO-ELM model is smaller than that of the other two models. As shown in

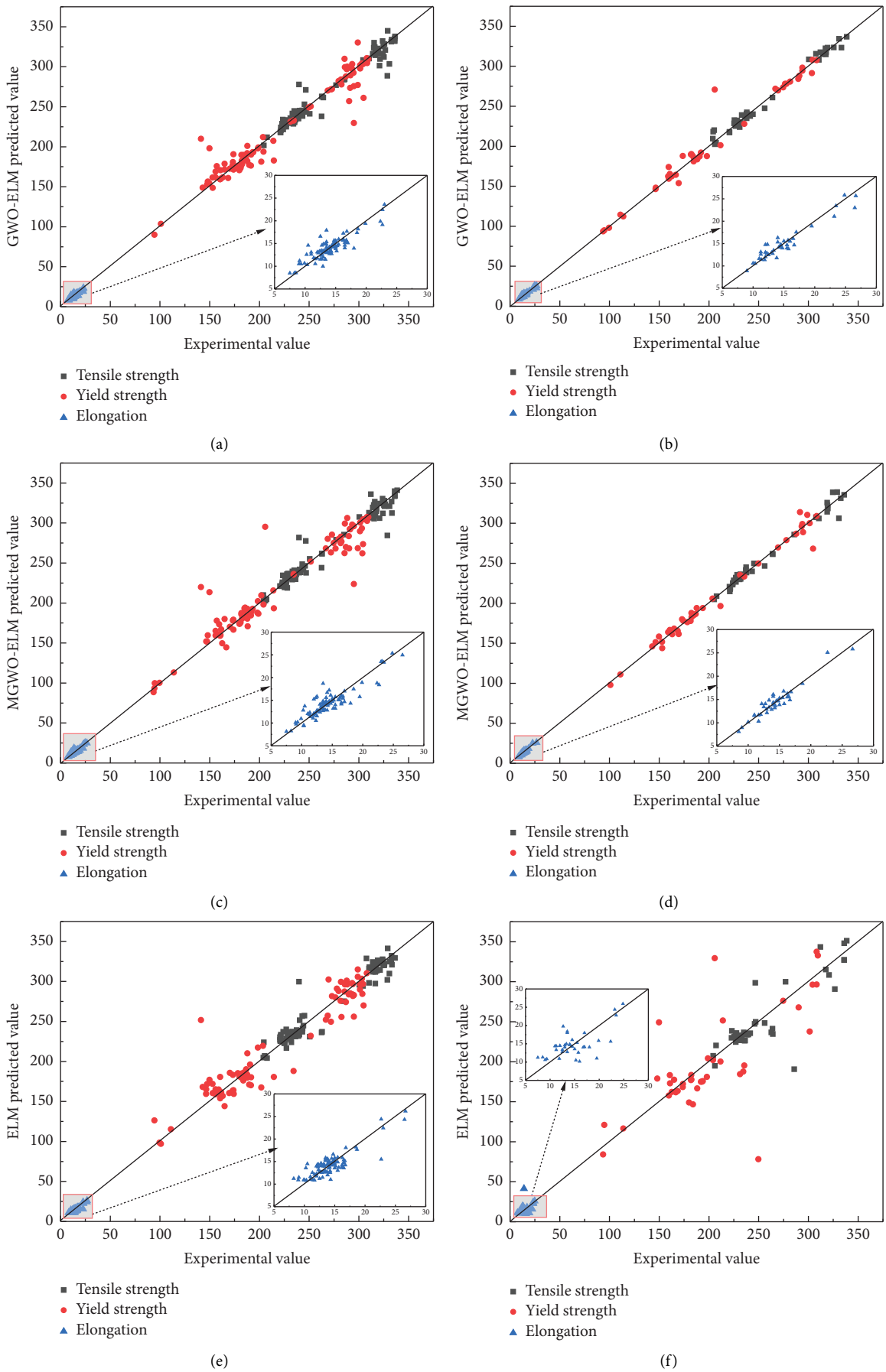

Figure 11: Predicted versus actual values of the (a) GWO-ELM training set, (b) GWO-ELM test set, (c) MGWO-ELM training set, (d) MGWO-ELM test set, (e) ELM training set, and (f) ELM test set.

Table 8: Distribution of prediction errors for the three model test sets.

Mechanical properties	Name	Prediction value deviation (%)				
		[0, 5]	[5, 10]	[10, 15]	[15, 20] set	[20, +∞]
		Correct ratio (%)				
Tensile strength	GWO-ELM	95	5	0	0	0
	MGWO-ELM	95	2.5	0	0	2.5
	ELM	65	15	15	0	5
Yield strength	GWO-ELM	87.5	10	5	2.5	2.5
	MGWO-ELM	62.5	30	2.5	2.5	2.5
	ELM	37.5	25	7.5	7.5	22.5
Elongation	GWO-ELM	57.5	20	12.5	5	5
	MGWO-ELM	42.5	25	10	7.5	15
	ELM	12.5	25	7.5	15	40

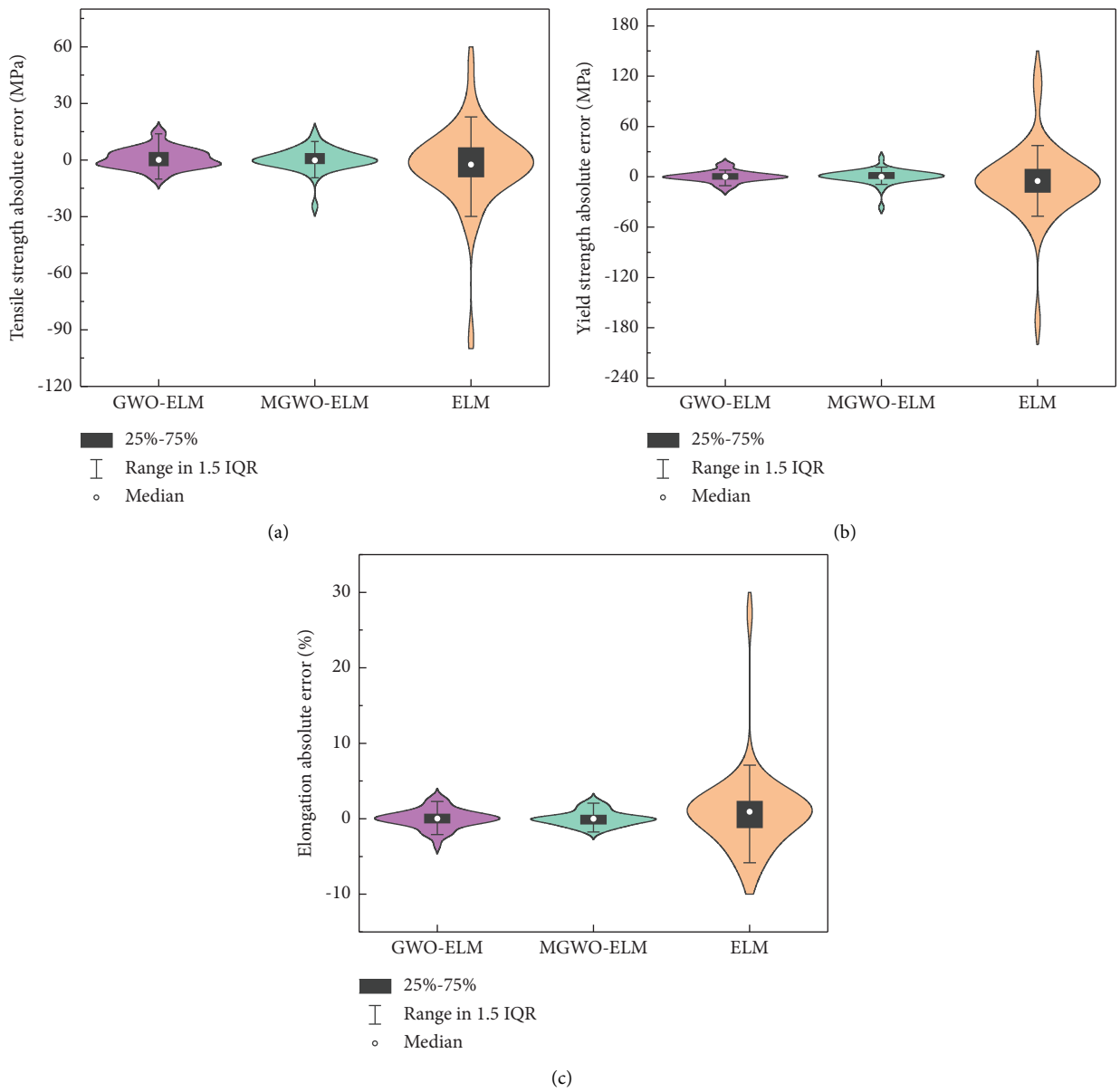

Figure 12: Absolute error distribution of the mechanical properties: (a) tensile strength, (b) yield strength, and (c) elongation.

Figure 12(b), the prediction error range of yield strength in the GWO-ELM model is significantly smaller than that of the other two models. The GWO-ELM model performs better than the MGWO-ELM model in predicting tensile strength and yield strength but not in predicting elongation. As shown in Figure 12(c), the MGWO-ELM model is slightly better than the GWO-ELM model in the prediction of elongation. In general, compared with the other two models, the prediction accuracy of tensile strength, yield strength, and elongation can be higher in the GWO-ELM model.

5. Conclusion

This paper proposes an intelligent optimization algorithm, which has the advantages of a simple structure, short training time, and high prediction accuracy. This algorithm is successfully applied to the prediction of mechanical properties of aluminium alloy strips in this paper and eventually achieves high prediction accuracy, providing a new method for predicting the mechanical properties of aluminium alloy strips, which has broad application prospects.

(1) Preprocessed industrial production data were used to train and test the GWO-ELM model. Through several experiments, the optimal network structure of the ELM algorithm and the optimal parameters of the Grey Wolf algorithm were determined. The weights and biases of the ELM were determined by the GWO algorithm. The optimal GWO-ELM model structure was successfully determined.

(2) After repeated training, the RMSEs of the GWO-ELM model for tensile strength, yield strength, and elongation were 5.365, 11.881, and 1.268, respectively. While the corresponding RMSEs of the MGWO-ELM model were 11.557, 20.465, and 1.845, and the corresponding RMSEs of the ELM model were 21.489 and 43.313. This indicates that the ELM model optimized by the GWO algorithm has higher prediction accuracy.

(3) When the prediction deviation is controlled within ±10%, the prediction accuracy of tensile strength in the GWO-ELM model, MGWO-ELM model, and ELM model is 100%, 97.5%, and 80%, respectively. The prediction accuracy of yield strength of the GWO-ELM model, MGWO-ELM model, and ELM model is 97.5%, 92.5%, and 62.5%, respectively. The prediction accuracy of elongation in the GWO-ELM model, MGWO-ELM model, and ELM model is 77.5%, 77.5%, and 37.5%, respectively. The comprehensive performance of the GWO-ELM model in predicting tensile strength, yield strength, and elongation is better than that of the other two models. The GWO algorithm successfully improves the stability and robustness of the ELM model.

Data Availability

The data used to support the findings of this study are available from the corresponding author upon request.

Conflicts of Interest

All authors declare that they have no conflicts of interest.

Acknowledgments

This work was supported by the Major Project of Science and Technology in Nanning (No. 20191002).

References

[1] G. Maizza, R. Pero, M. Richetta, and R. Montanari, "Continuous dynamic recrystallization (CDRX) model for aluminum alloys," *Journal of Materials Science*, vol. 53, no. 6, pp. 4563–4573, 2018.

[2] X. Li, M. Xu, and Z. Zhang, "Hot Damage Evolution in a High Strength Aluminum alloy during Hot Forming," *A Study Using the Gurson Journal of Materials Research and Technology*, vol. 14, 2021.

[3] D. Diehl, C. Kohler, E. L. Schneider, and T. G. R. Clarke, "Eddy current at high temperatures for in-situ control of heat treatment precipitation in hardening aluminum alloys," *IEEE Sensors Journal*, vol. 20, no. 23, pp. 14514–14520, 2020.

[4] C. H. Jia, C. X. Liu, Y. C. Liu, C. Li, and H. J. Li, "Microstructural evolution and constitutive models of 9CrMoCoB heat-resistant steel during high-temperature deformation," *Journal of Iron and Steel Research International*, vol. 26, pp. 1228–1239, 2019.

[5] H. Zhang, G. Chen, Q. Chen, F. Han, and Z. Zhao, "A physically-based constitutive modelling of a high strength aluminum alloy at hot working conditions," *Journal of Alloys and Compounds*, vol. 743, pp. 283–293, 2018.

[6] M. C. Karthik Rao, L. Malghan Rashmi, F. Kara, S. Arunkumar, S. Rao Shrikantha, and A. Herbert Mervin, "Influence of support vector regression (SVR) on cryogenic face milling," *Advances in Materials Science and Engineering*, vol. 2021, Article ID 9984369, 18 pages, 2021.

[7] G. Pilania, "Machine learning in materials science: from explainable predictions to autonomous design," *Computational Materials Science*, vol. 193, Article ID 110360, 2021.

[8] S. Guo, J. Yu, X. Liu, C. Wang, and Q. Jiang, "A predicting model for properties of steel using the industrial big data based on machine learning," *Computational Materials Science*, vol. 160, pp. 95–104, 2019.

[9] Q. Zou, L. Chen, N. Xiong, S. Zou, and C. Wang, "Prediction and Key Computer Programming of Mechanical Properties of Hot Rolled Plate Based on BP Neural Network," in *Proceedings of the 2009 International Conference on Computational Science and Engineering*, Vancouver, BC, Canada, Auguest 2009.

[10] M. Hu, Q. Tan, R. Knibbe et al., "Prediction of mechanical properties of wrought aluminium alloys using feature engineering assisted machine learning approach," *Metallurgical and Materials Transactions A*, vol. 52, no. 7, pp. 2873–2884, 2021.

[11] N. Lenzen and O. Altay, "Machine learning enhanced dynamic response modelling of superelastic shape memory alloy wires," *Materials*, vol. 15, no. 1, p. 304, 2022.

[12] Q. Lan, X. Wang, J. Sun et al., "Artificial neural network approach for mechanical properties prediction of as-cast A380 aluminum alloy," *Materials Today Communications*, vol. 31, Article ID 103301, 2022.

[13] C. Wu, C. Wang, and J. W. Kim, "Bending deformation prediction in a welded square thin-walled aluminum alloy

tube structure using an artificial neural network," *The International Journal of Advanced Manufacturing Technology*, vol. 117, no. 9-10, pp. 2791–2805, 2021.

[14] R. Jaafreh, U. M. Chaudry, K. Hamad, and T. Abuhmed, "Age-hardening behavior guided by the multi-objective evolutionary algorithm and machine learning," *Journal of Alloys and Compounds*, vol. 893, Article ID 162104, 2022.

[15] Y. Sun, W. Zeng, Y. Han et al., "Determination of the influence of processing parameters on the mechanical properties of the Ti-6Al-4V alloy using an artificial neural network," *Computational Materials Science*, vol. 60, pp. 239–244, 2012.

[16] E. Aykut, A. A. Elmas, and A. Mustafa, "Artificial intelligence-based surface roughness estimation modelling for milling of AA6061 alloy," *Advances in Materials Science and Engineering*, vol. 2021, p. 10, 2021.

[17] F. Kara, M. Karabatak, M. Ayyıldız, and E. Nas, "Effect of machinability, microstructure and hardness of deep cryogenic treatment in hard turning of AISI D2 steel with ceramic cutting," *Journal of Materials Research and Technology*, vol. 9, no. 1, pp. 969–983, 2020.

[18] I. V. Manoj, S. Hargovind, S. Narendranath, P. M. Mashinini, and F.. Kara, "Examination of machining parameters and prediction of cutting velocity and surface roughness using RSM and ANN using WEDM of altemp HX," *Advances in Materials Science and Engineering*, vol. 2022, Article ID 5192981, 9 pages, 2022.

[19] G. B. Huang, Q. Y. Zhu, and C. K. Siew, "Extreme Learning Machine: Theory and Applications," *Neurocomputing*, vol. 70, no. 1, 2005.

[20] Z. Cao, J. Xia, M. Zhang et al., "Optimization of gear blank preforms based on a new R- GPLVM model utilizing GA-ELM," *Knowledge-Based Systems*, vol. 83, 2015.

[21] X. Sui and Z. Lv, "Prediction of the mechanical properties of hot rolling products by using attribute reduction ELM," *The International Journal of Advanced Manufacturing Technology*, vol. 85, no. 5-8, 2016.

[22] J. Liu, X. Liu, and T. Le, "Rolling Force Prediction of Hot Rolling Based on GA-MELM," *Complexity*, vol. 2019, Article ID 3476521, 11 pages, 2019.

[23] H. Faris, I. Aljarah, M. A. Al-Betar, and S. Mirjalili, "Grey Wolf Optimizer: A Review of Recent Variants and Applications," *Neural Computing and Applications*, vol. 30, no. 22, 2018.

[24] Y. Zhang and X. Zhou, "An Improved Grey Wolf Algorithm for Solving Global Optimization Problems," *Journal of University of Shanghai for Science and Technology*, vol. 166, no. 01, pp. 73–82, 2021.

[25] L. Rodríguez, O. Castillo, J. Soria, and J. Soto, "A fuzzy hierarchical operator in the grey wolf optimizer algorithm," *Applied Soft Computing*, vol. 57, 2017.

[26] S. Saremi and Seyedeh Zahra Mirjalili & Seyed Mohammad Mirjalili, "Evolutionary population dynamics and grey wolf optimizer," *Neural Computing and Applications*, vol. 26, no. 5, 2015.

[27] M. Mengcan, C. Xiaofang, and X. Yongfang, "Constrained voting extreme learning machine and its application," *Journal of Systems Engineering and Electronics*, vol. 32, 2021.

[28] S. Wu, G. Cao, X. Zhou, N. Shi, and Z. Liu, "High dimensional data-driven optimal design for hot strip rolling of C-Mn steels," *ISIJ International*, vol. 57, pp. 1213–1220, 2017.

[29] P. Y. Chou, J. T. Tsai, and Jyh-Horng Chou, "Modeling and optimizing tensile strength and yield point on a steel bar using an artificial neural network with taguchi particle swarm optimizer," *IEEE Access*, vol. 4, 2016.

[30] Ö. Erkan, B. Işık, A. Çiçek, and F. Kara, "Prediction of damage factor in end milling of glass fibre reinforced plastic composites using artificial neural network," *Applied Composite Materials*, vol. 20, no. 4, pp. 517–536, 2013.

Hindawi
Advances in Materials Science and Engineering
Volume 2022, Article ID 1898124, 15 pages
https://doi.org/10.1155/2022/1898124

Research Article

Investigation of Nonlinear Vibrational Analysis of Circular Sector Oscillator by Using Cascade Learning

Naveed Ahmad Khan,[1] **Muhammad Sulaiman**,[1] **Jamel Seidu**,[2] **and Fahad Sameer Alshammari**[3]

[1]*Department of Mathematics, Abdul Wali Khan University, Mardan 23200, Pakistan*
[2]*School of Railways and Infrastructure Development, University of Mines and Technology (UMaT) Essikado, Sekondi-Takoradi, Ghana*
[3]*Department of Mathematics, College of Science and Humanitiesin Alkharj, Prince Sattam Bin Abdulaziz University, Al-Kharj 11942, Saudi Arabia*

Correspondence should be addressed to Jamel Seidu; jseidu@umat.edu.gh

Received 28 May 2022; Accepted 8 August 2022; Published 5 September 2022

Academic Editor: Liancheng Zhao

This paper analyzed the model of swinging oscillation of a solid circular sector arising in hydrodynamical machines, electrical engineering, heat transfer applications, and civil engineering. Nonlinear differential equations govern the mathematical model for frequency oscillation of the system. Furthermore, a computational strength of Cascade neural networks (CNNs) is utilized with backpropagated Levenberg–Marquardt (BLM) algorithm to study the oscillations in angular displacement (θ), velocity (θ'), and acceleration (θ''). A data set for the supervised learning of the CNN-BLM algorithm for different angles (α) and radius (R) are generated by Runge–Kutta (RK-4) method. The BLM algorithm further interprets the dataset with log-sigmoid as an activation function for the solutions' validation, testing, and training. The results obtained by the design scheme are compared with Akbari–Ganji's (AG) method. The rapid convergence and quality of the solutions are validated through performance indicators such as mean absolute deviations (MAD), root means square error, and error in Nash–Sutcliffe efficiency (ENSE). The statistics demonstrate the design scheme's applicability and efficiency to highly singular nonlinear problems.

1. Introduction

Nonlinear oscillation and its behavior is an important topic in applied physics, mathematics, and mechanical engineering that has piqued the interest of many scientists from the dawn of human recognition of the equations of motion [1]. In vibrations theory, an extremely unique and important place is held by oscillatory systems that contain fundamental nonlinearities. On the other hand, it is of the utmost significance to comprehend their behavior, not only from an academic standpoint but also in view of the countless potential applications [2–4]. The systems of complex nonlinear and chaotic responses are characterized by a unique equilibrium position, a strong nonlinearity described by a monotone increasing mooring restoring force, and a fluid structure [5–7]. The dynamical systems, including spherical pendulum, harmonic oscillator model of aromaticity, spring systems, symmetric, and biased hardening duffing oscillators, produce the nonlinear and modulated responses of multidegree exhibits the periodic vibration, saturation, thermal resonance, and waves [8, 9]. Fox and Goulbourne [10, 11] carried out experiments to study primary and superharmonic resonances on the nonlinear oscillation of dielectric elastomers subjected to applied static pressure and dynamic voltage. A. Alibakhshi [12] investigated the static and dynamic response of the free and forced vibrations of a micro/nanobeam made of a hyperelastic material incorporating strain-stiffening, size effect, and moderate rotation.

The oscillation of a rigid rod over a circular surface is considered a classical oscillator whose mathematical model

was first investigated by Gaylord [13] in 1979. Nonlinearity is an inherent property of every differential equation that describes a physical or biological phenomenon. Solving linear differential equations is quite straightforward and has been successfully implemented. On the other hand, the methods for solving nonlinear differential equations (NDEs) are not as readily available. Generally, NDEs do not have a precise solution. In general, finding exact and semianalytical solutions for such problems is challenging because of the nonlinearity in the elastic and damping components of the governing equations (14). NDEs have been the subject of all-embracing studies in various branches of nonlinear science and engineering. Poincare and Lyaponuv [15] were credited for being the first to solve the differential equations governing nonlinear processes. Their approaches were based on the existence of a values (large or small) parameter in the nonlinear equations, which allows the solution to be expanded as a power series whose components are generated by the integer powers of that small parameter. Using the series in the nonlinear model and equating the coefficients of the small parameters with like powers results in a system of linear ordinary differential equations whose solution caused the final result of the governing equation in closed form. This basic concept allowed the research community to solve numerous nonlinear scientific problems with a small or large parameter. The procedure was named the perturbation method. The method's only flaw is that it requires the existence of a small parameter in the equations, even though we know that the proposed parameter does not exist in many types of differential equations. A series of analytical and semiexact techniques that do not require a small parameter was proposed in the middle of the twentieth century to overcome the problem. Some well-known techniques used for the numerical and analytical solution of nonlinear problems are Adomian decomposition method (ADM) [16, 17], energy balance method (EBM) [18], variational iteration method (VIM) [19–21], extended direct algebraic method (EDAM) [22], Adams–Bashforth method [23], differential transform method [24], Hamiltonian approach [25, 26], Backlund method [27] rational harmonic balance method [28], min-max approach (MMA) [29, 30], power series technique [31], one-step hybrid block method [32], amplitude-frequency formulation (AFF) [33, 34], and modified homotopy perturbation method (MHPM) [35–37]. Ebrahimi Khah [38] studied the motion of a rigid rod rocking back over a circular surface using He's energy balance method. Galerkin method and modal analysis technique is utilized by G. Sheng [39, 40] to study the dynamic stability and nonlinear vibrations of the stiffened functionally graded (FG) cylindrical shell in a thermal environment. Reference [41] investigates the vibration analysis of a rigid rod using the Hamiltonian approach. Abul-Ez [42] employed the hybridization of the iteration perturbation method and variational iteration method to study the duffing oscillation of nonlinear oscillators. The above-cited literature shows that all of these techniques have been effectively applied to study the solutions and behavior of the nonlinear oscillatory models, but besides their advantages, it is observed with keen interest that such methods are gradient-based and require prior information about the problem. Prior information includes the choice of a small parameter, initial guess, continuity, and differentiability of the function. To overcome these drawbacks, gradient-free stochastic computing techniques based on the approximation ability of artificial neural networks are designed.

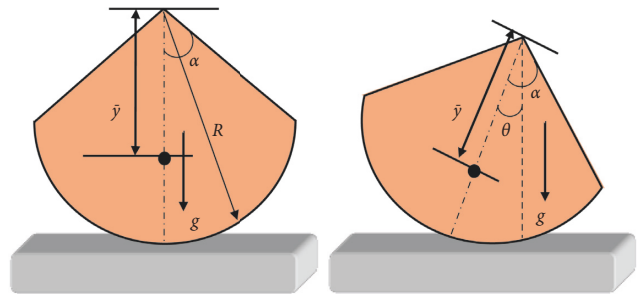

Figure 1: Geometric interpretation of a homogenous circular sector object over a solid surface.

The researcher's community has been widely employing the concepts of artificial neural network-based numerical computing techniques for exploring and exploiting linear/nonlinear mathematical systems. Some recent applications of the black-box stochastic methodologies include the approximate solutions for a mathematical model of chaotic base secure communication systems [43], nonlinear problems arising in heat transfer [44], thermal radiations of nanofluid [45, 46], nonlinear restoring moment and damping effects of ships [47], and wire coating dynamics [48]. These reported articles motivate authors to utilize the computational strength of artificial neural networks (ANNs) for the numerical treatment and analysis of nonlinear oscillation over a circular sector. The innovative insights of the presented study are summarized as follows:

(i) A mathematical model for the oscillation of a homogenous solid circular sector object is analyzed to study the influence of variations in angles and radius on angular frequency, velocity, and acceleration.

(ii) A novel application of artificial intelligence-based cascade neural networks via backpropagated Levenberg–Marquardt algorithm is presented effectively for the numerical solution of the nonlinear oscillator.

(iii) Approximate solutions for different scenarios of the nonlinear problem obtained by the design CNN-BLM algorithm are compared with analytical solutions by Ranga–Kutta method and Akbari–Ganji's method.

(iv) The proposed algorithm is executed multiple times to test the results' convergence, accuracy, and effectiveness. The performance of CNN-BLM is further validated by mean absolute deviations (MAD), root means square errors, and errors in Nash–Sutcliffe efficiency (ENSE).

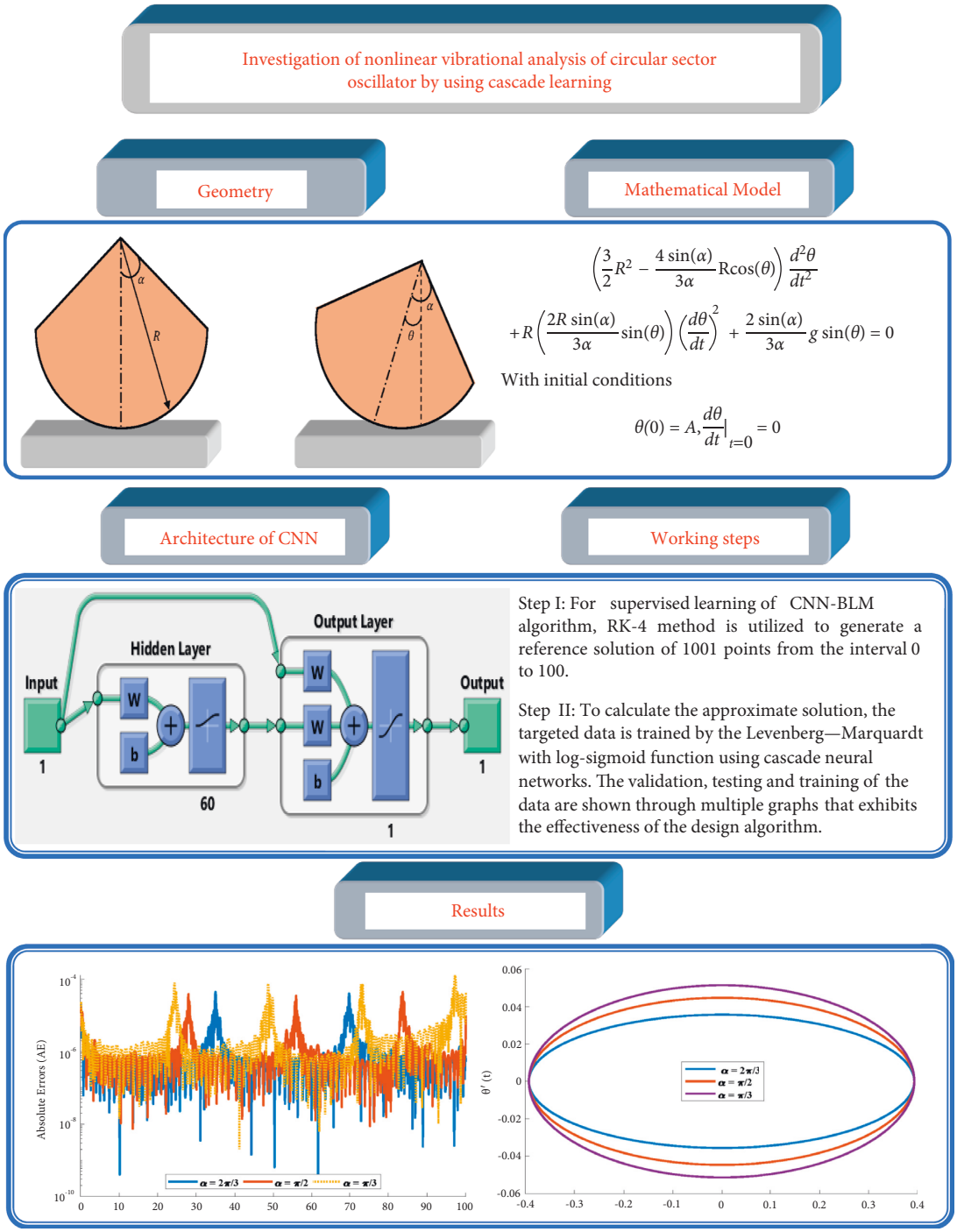

Figure 2: A detailed graphical illustration of the physical problem with its mathematical model, the solution strategy based on the architecture of cascade learning, and the optimization framework of the Levenberg–Marquardt algorithm to measure the influence of R and α on displacement, velocity, and acceleration of the circular sector.

2. Swinging Oscillation of a Solid Circular Sector Object

In this section, an oscillation of homogenous circular sector of angle α and radius (R) over a solid surface is considered as shown in Figure 1. The circular object is allowed to roll on a fixed solid surface producing an oscillatory motion (back and forth) with no sliding effect, it is evident that α will

Table 1: Different cases of equation (3) based on variations in radius and angular displacement of a circular sector with $A = \pi/8$ and $g = 9.8\,\mathrm{ms}^{-2}$.

Angular displacement				
Scenarios	Radius	Case I	Case II	Case III
1	15	$\alpha = 2\pi/3$	$\alpha = \pi/2$	$\alpha = \pi/3$
2	10	$\alpha = 2\pi/3$	$\alpha = \pi/2$	$\alpha = \pi/3$
3	05	$\alpha = 2\pi/3$	$\alpha = \pi/2$	$\alpha = \pi/3$

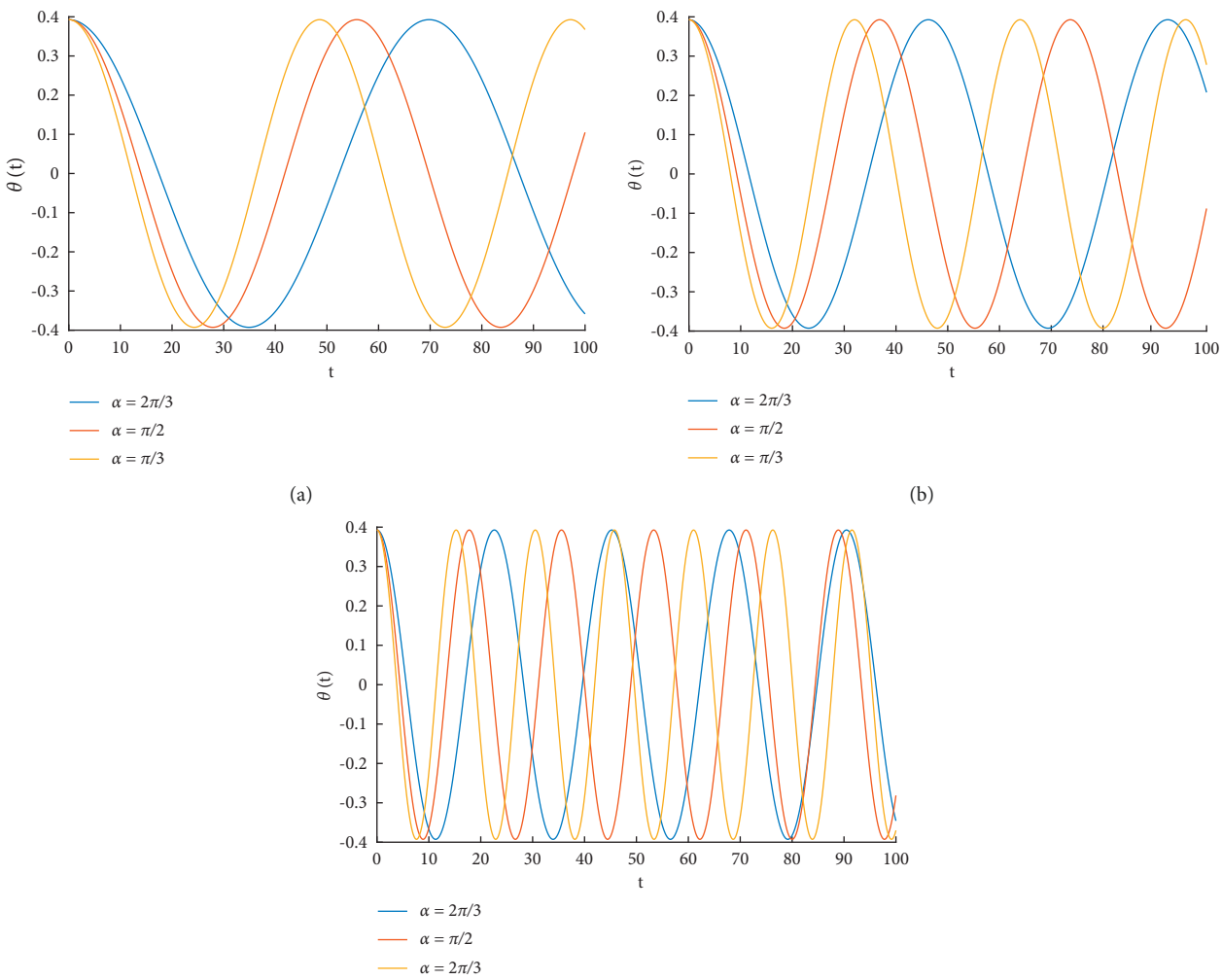

Figure 3: Influence of variations in R and α on an angular displacement of a circular sector.

Table 2: Comparison of approximate solutions obtained by the proposed algorithm for the influence of variations in α with $R = 15$ on an angular displacement of a homogenous circular sector.

	Case I			Case II			Case III		
t	Numerical	AGM	CNN-BLMA	Numerical	AGM	CNN-BLMA	Numerical	AGM	CNN-BLMA
0	0.39269908	**0.39269908**	0.392687276	0.39269908	**0.39269908**	0.392686548	0.39269908	**0.39269908**	0.392681150
10	0.24512253	0.24501045	**0.245122185**	0.17012305	0.16964486	**0.170122142**	0.10875275	0.10762438	**0.108752428**
20	−0.08993096	0.09371990	**−0.089931250**	−0.24887845	−0.25944763	**−0.248879413**	−0.33471506	−0.35104698	**−0.334714661**
30	−0.35555274	0.36692738	**−0.355552929**	−0.38187454	−0.38749464	**−0.381874167**	−0.29201803	−0.27870234	**−0.292017486**
40	−0.35254525	0.35162485	**−0.352544182**	−0.08143699	−0.05286683	**−0.081436623**	0.17597552	0.20864948	**0.175975984**
50	−0.08307460	0.06065639	**−0.083074398**	0.31332380	0.33172291	**0.313323484**	0.38631310	0.37789019	**0.386315754**
60	0.25054818	0.26978783	**0.250548338**	0.34991634	0.33408668	**0.349915015**	0.03769972	−0.00330218	**0.037698188**
70	0.39263866	0.39135302	**0.392621108**	−0.01205181	−0.04827707	**−0.012052894**	−0.36626688	−0.39470691	**−0.366268070**
80	0.23961867	0.21847002	**0.239617147**	−0.36004875	−0.38611530	**−0.360049029**	−0.23945080	−0.18427538	**−0.239449924**
90	−0.09675804	−0.12620233	**−0.096759026**	−0.29838583	−0.26304319	**−0.298385305**	0.23706674	0.29236833	**0.237067580**
100	−0.35844921	−0.37955984	**−0.358447834**	0.10482796	0.16555209	**0.104818684**	0.36732664	0.33439609	**0.367367867**

change, and the system will satisfy the following nonlinear differential equation [49, 50]:

$$\left(\frac{3}{2\lambda} - 2\cos(\theta)\right)\theta + \sin(\theta)\dot{\theta}^2 + \frac{\lambda g}{R}\sin(\theta) = 0. \quad (1)$$

Introducing the dimensionless geometrical parameter

$$\lambda = \frac{\overline{y}}{R} = \frac{2\sin(\alpha)}{3\alpha}, \quad (2)$$

Table 3: Comparison of approximate solutions obtained by the proposed algorithm for different cases of scenarios 2 and 3 of angular displacement of a homogenous circular sector.

	Case I		Case II		Case III		Case I		Case II		Case III	
t	Numerical	CNN-BLMA	Numerical	CNN-BLMA	Numerical	CNN-BLMA	Numerical	CNN-BLMA	Numerical	CNN-BLMA	Numerical	CNN-BLMA
0	0.392699082	0.392685093	0.392699082	0.392670786	0.392699082	0.392661944	0.39269908	0.392624275	0.39269908	0.39259210	0.39269908	0.39256229
10	0.083388890	0.083389783	−0.053232122	−0.053235250	−0.151961836	−0.151961785	−0.36749090	−0.367653662	−0.36374462	−0.36345803	−0.22287067	−0.22264354
20	−0.358208978	−0.358210302	−0.378788375	−0.378796623	−0.278995466	−0.279004381	0.29461331	0.294685021	0.28024739	0.28022323	−0.14975320	−0.14978926
30	−0.234800091	−0.234800409	0.155649427	0.155648690	0.363640049	0.363652579	−0.18251243	−0.182477435	−0.15297185	−0.15299577	0.38443195	0.38481916
40	0.260262179	0.260262109	0.337907757	0.337907826	−0.000819025	−0.000819677	0.04540274	0.045441209	0.00077900	0.00061557	−0.28550774	−0.28569189
50	0.343613202	0.343612501	−0.246351630	−0.246347082	−0.363030749	−0.363041240	0.09803384	0.098023706	0.15154292	0.15147925	−0.06938614	−0.06961510
60	−0.115291291	−0.115290537	−0.272637949	−0.272634926	0.280132157	0.280142714	−0.22786478	−0.227850757	−0.27917225	−0.27905960	0.35986908	0.35952351
70	−0.391351734	−0.391304302	0.318824563	0.318825376	0.150454989	0.150457157	0.32678376	0.326762802	0.36317118	0.36298554	−0.33516516	−0.33536112
80	−0.050882422	−0.050882087	0.187321504	0.187318255	−0.392695353	−0.392577931	−0.38266277	−0.382575699	−0.39269606	−0.39197161	0.01440356	0.01442215
90	0.370322679	0.370323421	−0.368151155	−0.368156176	0.153465671	0.153473754	0.38920766	0.389280863	0.36431245	0.36406319	0.31975532	0.32062675
100	0.207666340	0.207662784	−0.087977218	−0.087990333	0.277853197	0.278105162	−0.34571116	−0.345711854	−0.28131805	−0.28162897	−0.37007441	−0.37007000

Table 4: Comparison of absolute errors in solutions obtained by CNN-BLM algorithm with Akbari–Ganji's method for different scenarios of equation (3).

Scenario 1							Scenario 2			Scenrio 3		
	Case I		Case II		Case III		Case I	Case II	Case III	Case I	Case II	Case III
t	AGM	CNN-BLMA	AGM	CNN-BLMA	AGM	CNN-BLMA	CNN-BLMA	CNN-BLMA	CNN-BLMA	CNN-BLMA	CNN-BLMA	CNN-BLMA
0	$0.00E+00$	$1.18E-05$	$0.00E+00$	$1.25E-05$	$0.00E+00$	$1.79E-05$	$1.40E-05$	$2.83E-05$	$3.71E-05$	$7.48E-05$	$1.07E-04$	$1.37E-04$
10	$1.12E-04$	$\mathbf{1.36E-07}$	$4.78E-04$	$\mathbf{6.49E-07}$	$1.13E-03$	$\mathbf{1.42E-08}$	$8.93E-07$	$3.13E-06$	$5.09E-08$	$1.63E-04$	$2.87E-04$	$2.27E-04$
20	$3.79E-03$	$\mathbf{9.30E-08}$	$1.06E-02$	$\mathbf{6.91E-07}$	$1.63E-02$	$\mathbf{6.06E-07}$	$1.32E-06$	$8.25E-06$	$8.92E-06$	$7.17E-05$	$2.42E-05$	$3.61E-05$
30	$1.14E-02$	$\mathbf{3.35E-07}$	$5.62E-03$	$\mathbf{3.73E-07}$	$1.33E-02$	$\mathbf{1.38E-07}$	$3.18E-07$	$7.37E-07$	$1.25E-05$	$3.50E-05$	$2.39E-05$	$3.87E-04$
40	$9.20E-04$	$\mathbf{5.13E-07}$	$2.86E-02$	$\mathbf{3.39E-07}$	$3.27E-02$	$\mathbf{2.49E-07}$	$7.00E-08$	$6.93E-08$	$6.52E-07$	$3.85E-05$	$1.63E-04$	$1.84E-04$
50	$2.24E-02$	$\mathbf{2.57E-07}$	$1.84E-02$	$\mathbf{5.25E-07}$	$8.42E-03$	$\mathbf{2.98E-06}$	$7.01E-07$	$4.55E-06$	$1.05E-05$	$1.01E-05$	$6.37E-05$	$2.29E-04$
60	$1.92E-02$	$\mathbf{2.99E-07}$	$1.58E-02$	$\mathbf{6.24E-07}$	$4.10E-02$	$\mathbf{5.34E-07}$	$7.54E-07$	$3.02E-06$	$1.06E-05$	$1.40E-05$	$1.13E-04$	$3.46E-04$
70	$1.29E-03$	$\mathbf{1.67E-05}$	$3.62E-02$	$\mathbf{6.55E-08}$	$2.84E-02$	$\mathbf{1.33E-06}$	$4.74E-05$	$8.13E-07$	$2.17E-06$	$2.10E-05$	$1.86E-04$	$1.96E-04$
80	$2.11E-02$	$\mathbf{5.31E-07}$	$2.61E-02$	$\mathbf{3.25E-07}$	$5.52E-02$	$\mathbf{4.38E-07}$	$3.35E-07$	$3.25E-06$	$1.17E-04$	$8.71E-05$	$7.24E-04$	$1.86E-05$
90	$2.94E-02$	$\mathbf{7.00E-07}$	$3.53E-02$	$\mathbf{7.83E-07}$	$5.53E-02$	$\mathbf{5.88E-07}$	$7.42E-07$	$5.02E-06$	$8.08E-06$	$7.32E-05$	$2.49E-04$	$8.71E-04$
100	$2.11E-02$	$\mathbf{5.37E-07}$	$6.07E-02$	$\mathbf{9.28E-06}$	$3.29E-02$	$\mathbf{4.26E-05}$	$3.56E-06$	$1.31E-05$	$2.52E-04$	$6.99E-07$	$3.11E-04$	$1.92E-06$

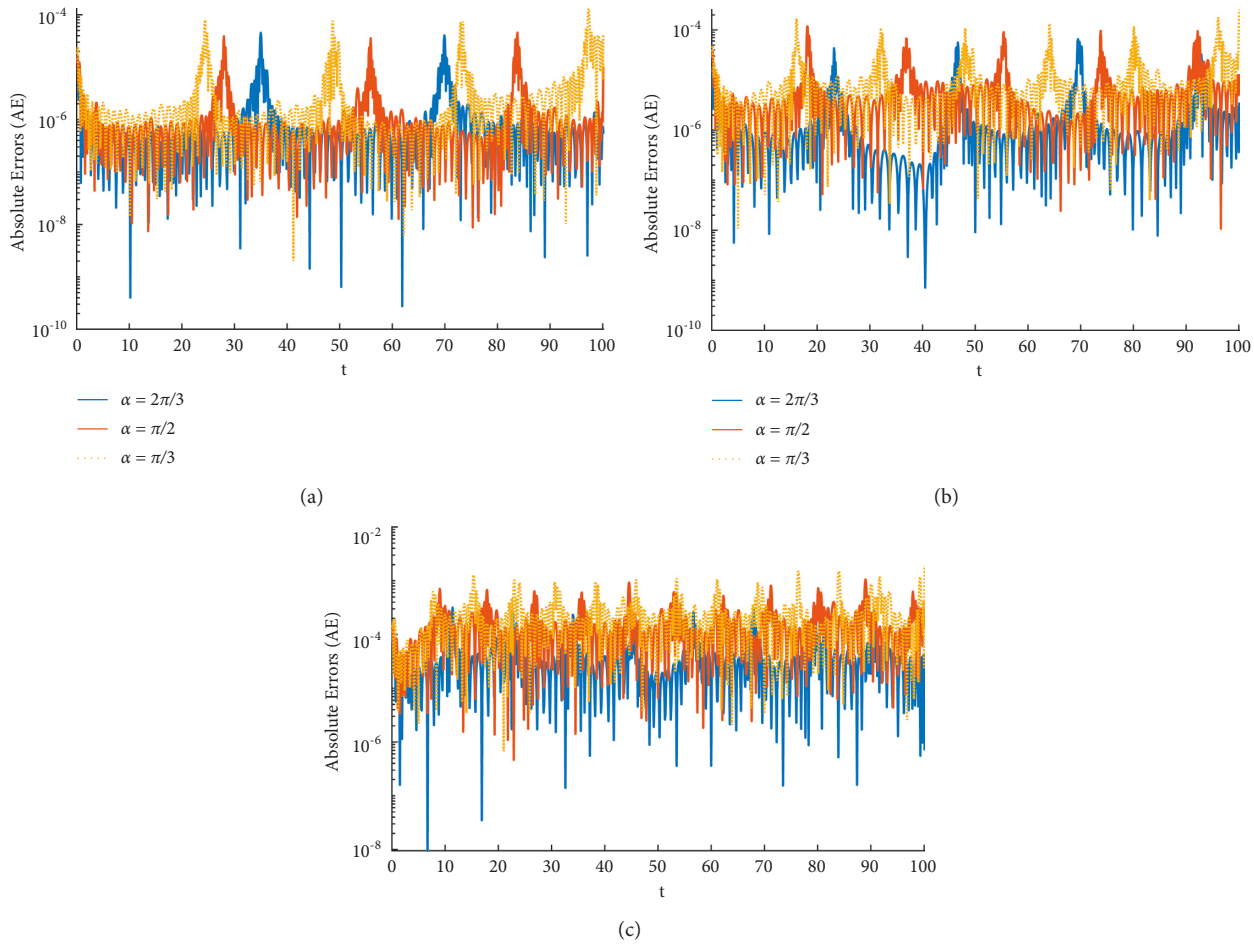

Figure 4: Absolute errors in solutions of CNN-BLM algorithm for different cases of scenarios 1, 2, and 3.

where $\overline{y} = 2R\sin(\alpha)/3\alpha$ is the height of the mass center. Using (2) in (1) will give

$$\left(\frac{3}{2}R^2 - \frac{4\sin(\alpha)}{3\alpha}R\cos(\theta)\right)\frac{d^2\theta}{dt^2} + R\left(\frac{2R\sin(\alpha)}{3\alpha}\sin(\theta)\right)\left(\frac{d\theta}{dt}\right)^2 + \frac{2\sin(\alpha)}{3\alpha}g\sin(\theta) = 0. \tag{3}$$

Subjected to the initial conditions

$$\theta(0) = A, \left.\frac{d\theta}{dt}\right|_{t=0} = 0, \tag{4}$$

where A is vibrational amplitude, θ denotes the angular displacement, and t is the dimensionless time variable.

3. Design Methodology

3.1. Cascade Neural Networks. An artificial neural network (ANN) is a collection of interconnected, basic components known as neurons with multiple inputs and a single output, and each neuron represents a mapping. The output of a neuron is a function of the sum of its inputs which is generated with the help of the activation function. A neural network architecture that only contains the input and output layer is called perceptron [51]. The sum of weighted signals in perceptron is transmitted directly to the output layer from the input layer. In neural network modeling, multilayer perceptron (MLP), also called feed-forward neural network (FNN) comes with an additional layer between the input and output layer known as the hidden layer. In MLP, the signals that enter the hidden layer are processed by the transfer function to obtain the desired results. In FNN, the connection between the input and output layer is indirect while in perceptron, they possess a direct relation. The direct network between input and output layers formulated by the combination of MLP and perceptron is named as cascade neural networks (CNNs) [52]. The basic structure of CNN is based on two ideas. First, is to build an architecture of cascade by adding new neurons with their connection to all inputs and previously hidden neurons without changing configuration at each layer. The second idea is to minimize the residual error by training only the newly created neurons by fitting their weights. The network is updated with new neurons and the performance increases.

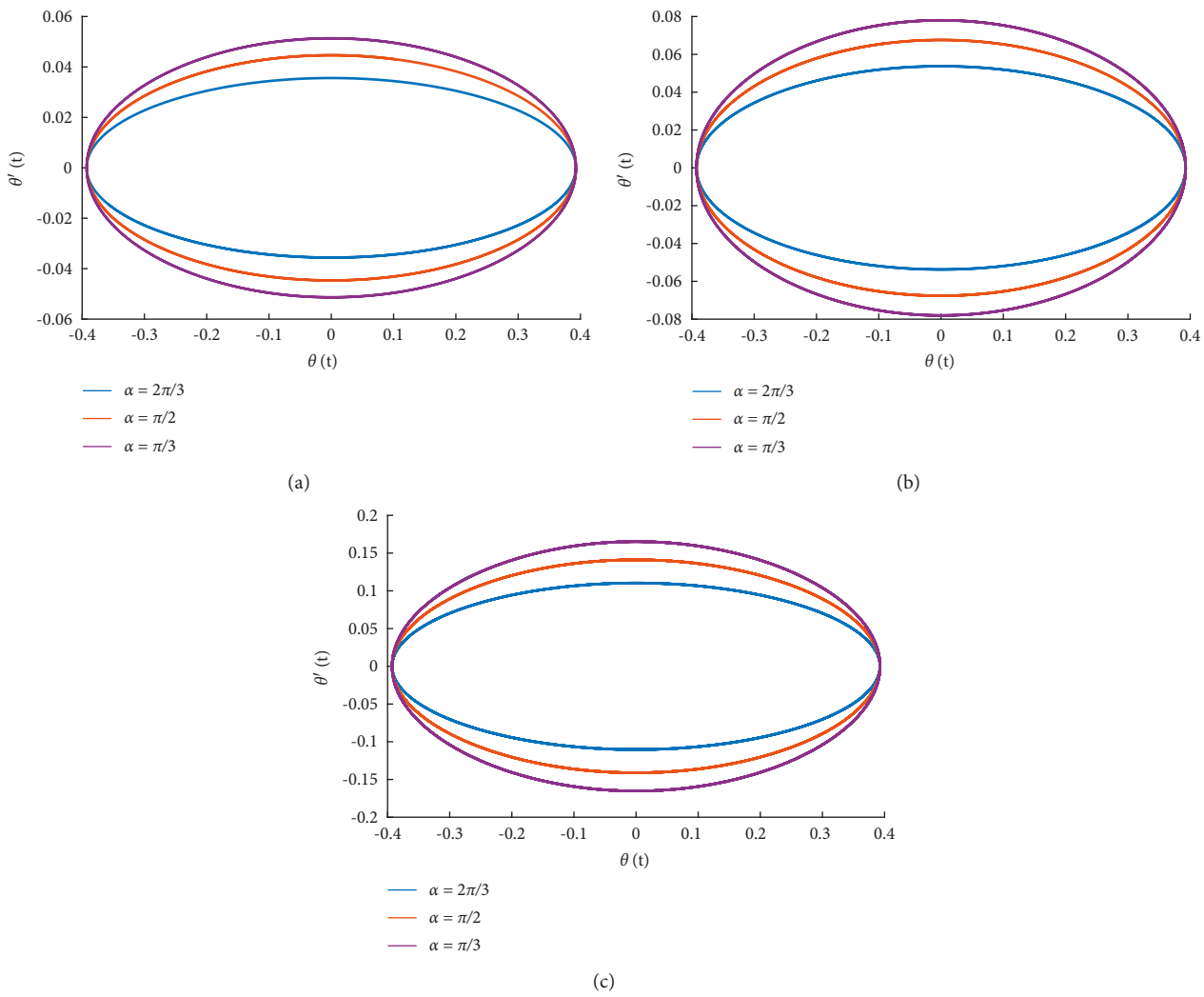

Figure 5: Stability analysis in terms of angular velocity and acceleration by CNN-BLM algorithm for different cases of scenarios 1, 2, and 3.

Initially, the cascade neural networks start the process with m inputs and a single targeted date without hidden neurons. The output neuron is connected to each input using weights such as $(w_1, w_2 \ldots, w_m)$ with a standard sigmoid function. The Log-sigmoid is one of the best nonlinear normalized functions, which is differentiable and continuous; therefore, it gives a smooth gradient preventing jumps in the output values. The output of the network is presented as

$$y = f(\mathbf{x}; \mathbf{w}) = \frac{1}{\left(1 + \exp\left(-w_0 - \sum_i^m w_i x_i\right)\right)}. \quad (5)$$

The new neurons formed are added to the network, and each neuron is connected to hidden neurons. A suitable algorithm trains the neurons for output. The basic advantage of CNN is that no structure for the network is predefined, it automatically built its architecture from the training data. Secondly, the learning process of CNN is fast compared to other networks because each neuron is trained independently.

3.2. Learning Procedure and Performance Measures. This section discusses the working and training procedure of neurons in CNN architecture. The learning strategy of the neurons in CNN is based on two phases. Initially, a network is presented with inputs of the reference data set of 1001 points generated by the Ranka–Kutta method. Secondly, the inputs and the weights in CNN are trained by an appropriate algorithm Levenberg–Marquardt with a log-sigmoid activation function for the output. The architecture of CNN along with the workflow of the design algorithm is shown in Figure 2.To examine the accuracy and effectiveness of the results of the CNN-BLM algorithm for oscillations of the nonlinear circular sector, performance indices are defined in terms of mean square error (MSE) of fitness function of the model, regression R^2, absolute errors (AE), mean absolute deviations (MAD), root mean square error (RMSE), and error in Nash–Sutcliffe efficiency (ENSE). Formulation of these indices is given as [53]

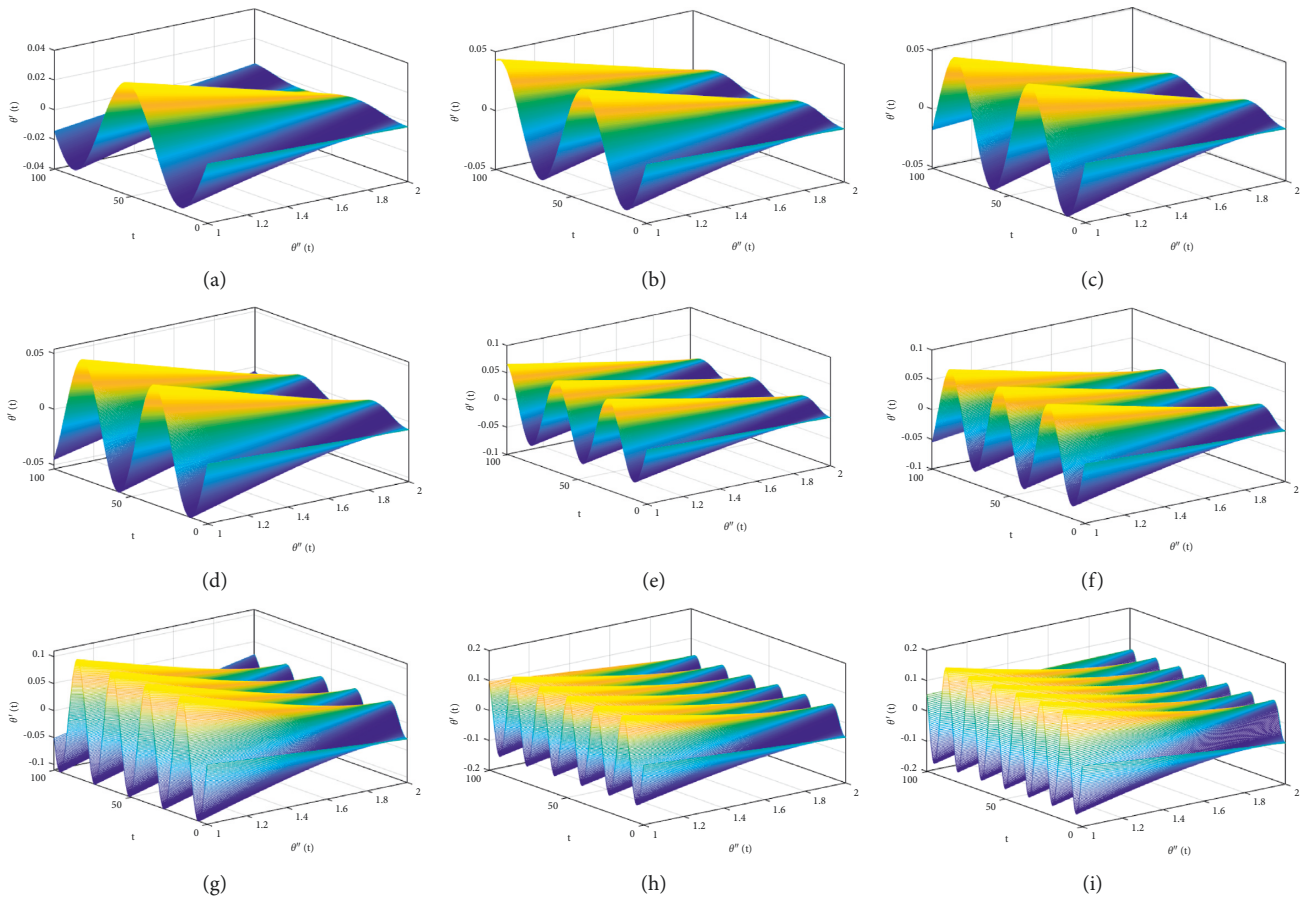

Figure 6: Surface plots for the comparison of angular velocity and acceleration of different cases and scenarios of oscillation in the homogenous circular sector.

$$
\begin{aligned}
\mathrm{MSE} &= \frac{1}{k}\sum_{j=1}^{k}\left(\theta_j(t)-\widehat{\theta}_j(t)\right)^2,\\
R^2 &= 1-\frac{\sum_{j=1}^{k}\left(\widehat{\theta}_j(t)-\overline{\theta}_j(t)\right)^2}{\sum_{j=1}^{k}\left(\theta_j(t)-\overline{\theta}_j(t)\right)^2},\\
\mathrm{AE} &= \left|\theta_j(t)-\overline{\theta}_j(t)\right|,\\
\mathrm{MAD} &= \frac{1}{k}\sum_{m=1}^{n}\left|\theta_j(t)-\overline{\theta}_j(t)\right|,\\
\mathrm{NSE} &= \left\{1-\frac{\sum_{j=1}^{k}\left(\theta_j(t)-\overline{\theta}_j(t)\right)^2}{\sum_{j=1}^{k}\left(\left(\theta_j(t)-\widehat{\theta}_j(t)\right)\right)^2}, \widehat{\theta}(x)=\frac{1}{k}\sum_{j=1}^{k}\theta_j(t),\right.\\
ENSE &= 1-NSE,
\end{aligned}
\tag{6}
$$

here, n shows the number of grid points, θ_j, $\overline{\theta}_j$ and $\widehat{\theta}_j$ are the reference, approximate, and mean of solution at jth input. The desired value of MSE, AE, MAD, RMSE, and ENSE for perfect fitting is equal to zero while the value of R^2 and NSE should be one.

4. Numerical Experimentation and Discussion

In this section, the artificial intelligence-based stochastic numerical technique is implemented on a nonlinear mathematical model of oscillations in a circular section given by equations (3)–(4) to study the angular displacement, velocity, and acceleration. Different cases of the problem based on variations in R and α are given in Table 1.

Approximate solutions for angular displacement of solid circular sector obtained by the designs scheme for different values of radius and angle are shown in Figure 3. It can be seen that by reducing the angle with a constant semicircular radius, the frequency of oscillation increases. Also, reducing the semicircular radius R causes an increase in the frequency of the oscillation. It is worthy to note that the frequency of oscillation determined by the design scheme is higher than the frequency obtained by Akbari–Ganji's (AG) method for different cases of scenario 1 as shown in Table 2. Table 3 compares the proposed algorithm's approximate solutions with numerical solutions by the RK-4 method. Results of CNN-BLM for different scenarios of (3) overlap the analytical solution with minimum absolute errors, as shown in Table 4.

Table 5: Statistics of performance function in terms of mean square error for the influence of variations in R and α in equation (3).

R	Case I			Case II			Case III		
	Min	Mean	Std	Min	Mean	Std	Min	Mean	Std
15	$3.60E-12$	$1.05E-09$	$2.15E-09$	$1.54E-11$	$1.16E-10$	$2.57E-10$	$1.04E-10$	$3.67E-10$	$3.05E-10$
10	$3.00E-11$	$2.03E-10$	$2.13E-10$	$2.07E-10$	$1.09E-09$	$1.97E-09$	$3.67E-10$	$3.32E-09$	$7.16E-09$
5	$3.52E-09$	$1.80E-08$	$3.31E-08$	$5.26E-08$	$2.56E-07$	$6.29E-07$	$1.17E-07$	$5.06E-07$	$8.12E-07$

Table 6: Results of the gradient in terms of minimum, the mean, and standard deviation for different cases and scenarios of the problem.

R	Case I			Case II			Case III		
	Min	Mean	Std	Min	Mean	Std	Min	Mean	Std
15	$2.77E-09$	$2.77E-09$	$9.86E-07$	$6.52E-10$	$3.30E-08$	$7.88E-08$	$2.86E-09$	$5.91E-08$	$1.84E-07$
10	$4.94E-09$	$1.90E-07$	$2.99E-07$	$4.34E-09$	$2.51E-07$	$6.01E-07$	$3.63E-09$	$2.14E-07$	$6.84E-07$
5	$2.19E-08$	$2.95E-07$	$4.62E-07$	$2.28E-08$	$3.10E-07$	$4.53E-07$	$7.90E-09$	$3.52E-07$	$5.46E-07$

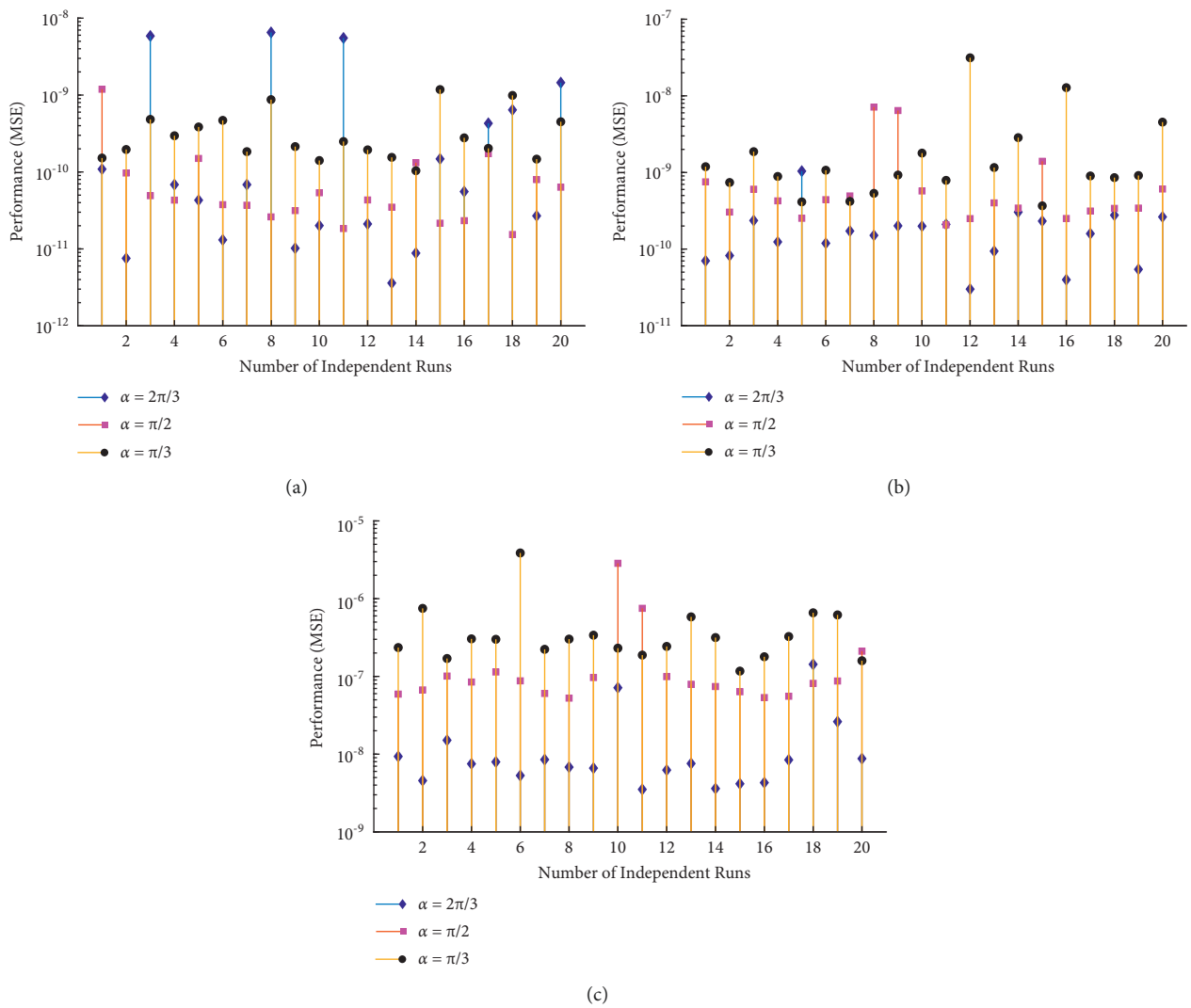

Figure 7: Values of performance function in terms of mean square error for different scenarios and cases of equation (3).

To study the smoothness of solutions, absolute errors for 1001 points are plotted in Figure 4. For scenario 1, the mean values of absolute errors lie around 10^{-6} to 10^{-9} while the maximum values of absolute errors lie around 10^{-4} to 10^{-5} at $t = 25, 30, 35, 50, 70, 85$ and 100. Similarly, the mean absolute errors for scenario 2 and 3 lies around 10^{-5} to 10^{-8}

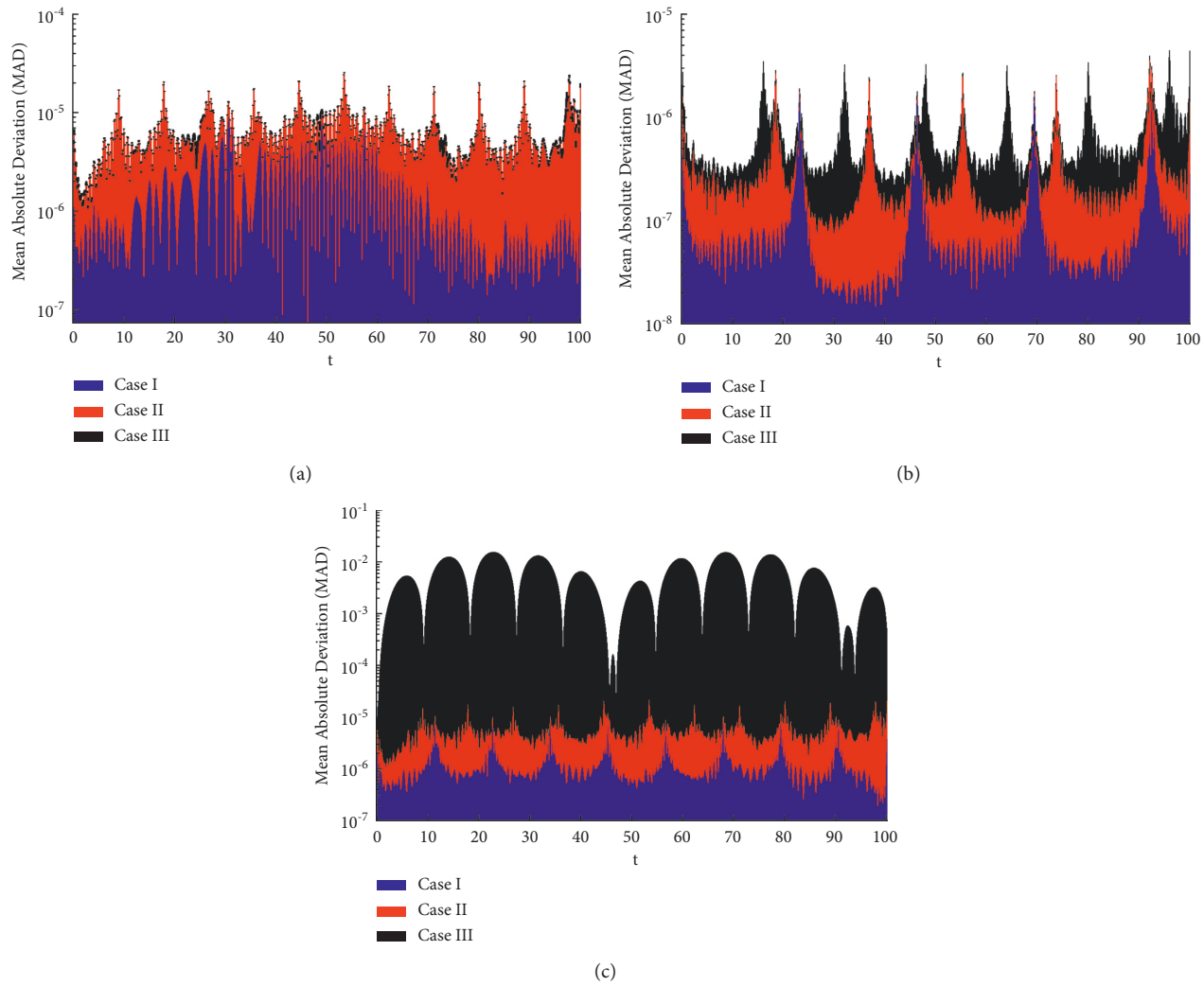

Figure 8: Behavior of values of mean absolute deviations for different scenarios and cases of equation (3).

Table 7: Statistics of root mean square error in our solutions for different cases and scenarios of the homogenous circular sector.

R	Case I			Case II			Case III		
	Min	Mean	Std	Min	Mean	Std	Min	Mean	Std
15	$1.01E-06$	$4.74E-05$	$5.26E-05$	$6.24E-06$	$5.27E-05$	$3.25E-05$	$1.55E-07$	$1.07E-06$	$1.80E-06$
10	$1.24E-07$	$1.02E-06$	$1.52E-06$	$4.10E-07$	$2.35E-06$	$2.69E-06$	$5.69E-07$	$3.70E-06$	$4.45E-06$
5	$1.63E-06$	$1.17E-05$	$9.40E-06$	$6.24E-06$	$5.27E-05$	$3.25E-05$	$3.06E-05$	$4.33E-03$	$3.24E-03$

Table 8: Results of ENSE obtained by the design scheme during 20 independent runs.

R	Case I			Case II			Case III		
	Min	Mean	Std	Min	Mean	Std	Min	Mean	Std
15	$7.46E-11$	$7.52E-08$	$1.41E-07$	$6.79E-09$	$4.11E-07$	$7.57E-07$	$3.84E-12$	$8.45E-10$	$4.52E-09$
10	$7.21E-09$	$5.60E-06$	$5.25E-05$	$3.03E-11$	$1.86E-09$	$8.37E-09$	$4.83E-11$	$4.42E-09$	$1.65E-08$
5	$5.18E-10$	$3.57E-08$	$9.72E-08$	$5.18E-10$	$3.57E-08$	$9.72E-08$	$2.00E-08$	$1.22E-04$	$5.97E-04$

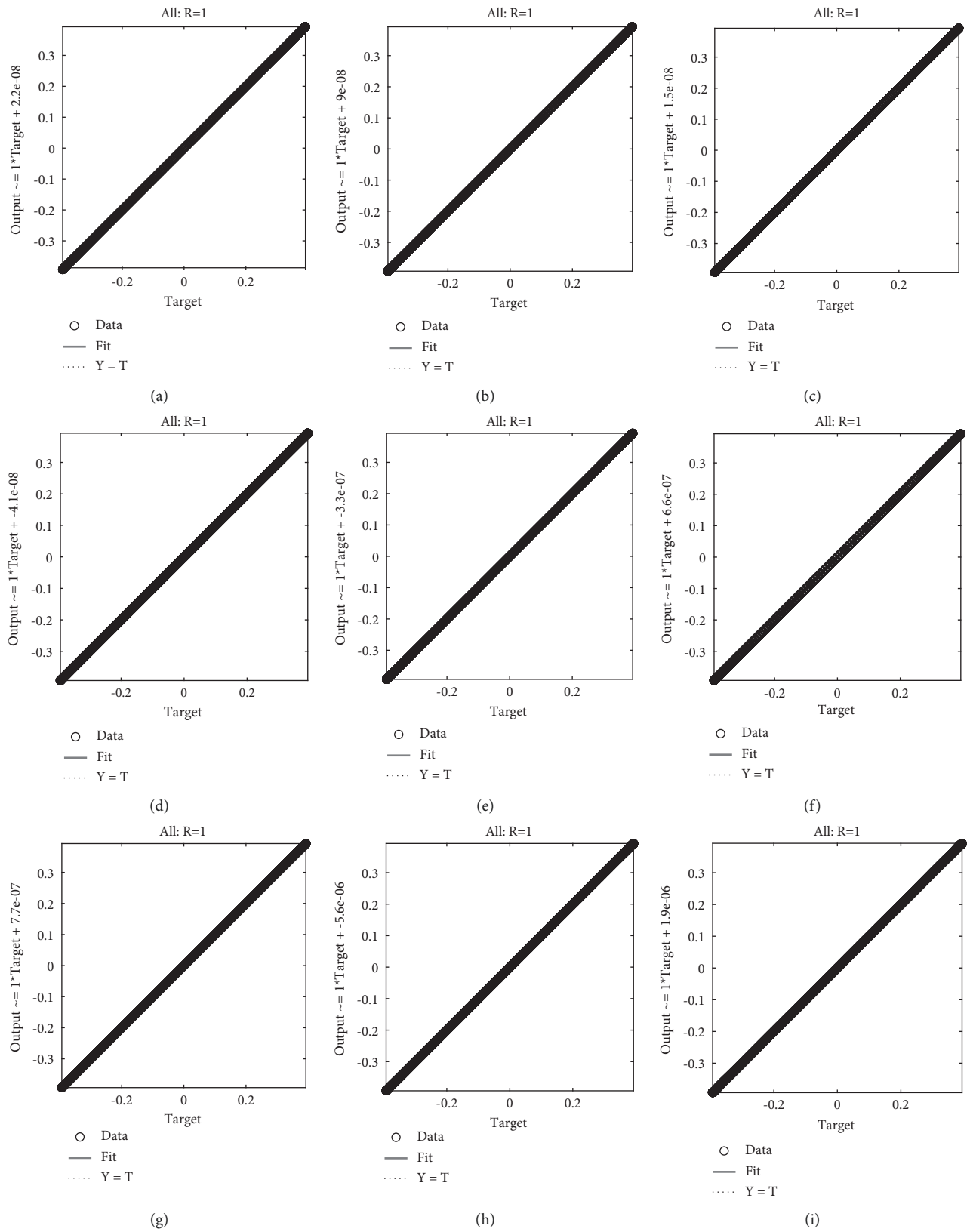

Figure 9: Regression analysis for each case of scenarios 1, 2, and 3 of a homogenous circular sector.

and 10^{-4} to 10^{-7}, respectively. Furthermore, to study the angular displacement and velocity, graphs of θ against θ' are shown though Figure 5. Apart from the graphs of the solutions, Figure 5 depicts that the oscillation trends are somehow harmonic and stable. It can be seen that velocity reaches its peak when the angle (α) or semicircular (R) decreases. Surface plots are shown through Figure 6 for angular velocity and acceleration in the homogenous circular sector. The oscillations are all stable because neither successive increases in the amplitudes are noticed in the displacement time diagram, nor open curves have been detected in the phase plane.To study the performance of the design scheme, the CNN-BLM algorithm is executed for 20 independent runs. Results of performance function in terms of mean square errors are dictated in Tables 5 and 6 and plotted through Figure 7. Mean values of MSE lie around 10^{-7} to 10^{-10}. Figure 8 shows the convergence of mean absolute deviations of the solutions at each step size. It can be seen that the mean value of MAD for each case lies around 10^{-8} to 10^{-9}. Tables 7 and 8 dictates the statistics of root mean square error (RMSE) and error in Nash–Sutcliffe efficiency (ENSE) in terms of minimum, mean and standard deviations. Additionally, regression plots are shown in Figure 9. It can be seen that the values of regression for each case are equal to unity which shows the efficiency, correctness, and accuracy of the results obtained by the CNN-BLM algorithm for oscillations in the homogenous circular sector.

5. Conclusions

In this paper, an artificial intelligent strength of cascade neural networks with backpropagated Levenberg–Marquardt algorithm is utilized to study the swinging oscillation of a solid circular sector over a solid surface. The governing relation of the system was presented in the form of the differential equation. The proposed algorithm is implemented to study the effect of variations in semicircular radius R and semicircular angle (α) on angular displacement, velocity, and acceleration of the system. The results dictate that by reducing the angle with a constant semicircular radius, the frequency of oscillation increases, in these cases, higher velocities are achievable and the phase-plane ellipse height is greater. In addition, reducing the semicircular radius R also causes an increase in the frequency of the oscillation. The approximate solution for angular displacement obtained by the CNN-BLM algorithm is compared with analytical solutions and approximate solutions by Akbari–Ganji's (AG) method. Absolute errors demonstrate the effectiveness of the results as the solutions by the CNN-BLM algorithm overlap the numerical solution up to 8 and 9 decimal places. Statistics of MAD, RMSE, MSE, and ENSE lie between 10^{-5} to 10^{-6}, 10^{-6} to 10^{-7}, 10^{-9} to 10^{-12}, and 10^{-9} to 10^{-11} which reflects the accuracy of solutions and validates the worth, efficiency, and stability of the proposed algorithm.

In the future, the authors aim to implement cascade neural networks to study the solutions of nonlinear fractional differential equations modeling physical problems such as biochemical reactors, skin cancer, tumor growth, physiological temperature regulations, drying processes, and chaotic behaviors in warless communications.

Data Availability

The data that support the findings of this study are available from the corresponding author upon reasonable request.

Conflicts of Interest

The authors declare that they have no conflicts of interest.

Authors' Contributions

All authors equally contributed to this manuscript and approved the final version.

References

[1] A. Lashkarboluki, H. Hosseini, and D. D. Ganji, "Investigating the solutions of two classical nonlinear oscillators by the AG method," *International Journal of Algorithms, Computing and Mathematics*, vol. 7, no. 3, pp. 110–128, 2021.

[2] V. Arnold, "Variational principles," in *Mathematical Methods of Classical Mechanics*, pp. 55–74, Springer, Berlin/Heidelberg, Germany, 1989.

[3] Z. Shah, E. Bonyah, E. Alzahrani, R. Jan, and N. Aedh Alreshidi, "Chaotic phenomena and oscillations in dynamical behaviour of financial system via fractional calculus," *Complexity*, vol. 2022, Article ID 8113760, 14 pages, 2022.

[4] V. Babitsky, V. Krupenin, and J. Angeles, "Vibration of strongly nonlinear discontinuous systems. Foundations of engineering mechanics," *Applied Mechanics Reviews*, vol. 55, no. 4, pp. 65–B66, 2002.

[5] J. M. T. Thompson, "Complex dynamics of compliant offshore structures," *Proceedings of the Royal Society of London. A. Mathematical and Physical Sciences*, vol. 387, pp. 407–427, 1983.

[6] F. A. Papoulias and M. M. Bernitsas, "Autonomous oscillations, bifurcations, and chaotic response of moored vessels," *Journal of Ship Research*, vol. 32, no. 03, pp. 220–228, 1988.

[7] W. Szemplińska-Stupnicka and J. Bajkowski, "The subharmonic resonance and its transition to chaotic motion in a non-linear oscillator," *International Journal of Non-Linear Mechanics*, vol. 21, no. 5, pp. 401–419, 1986.

[8] J. W. Miles, "Stability of forced oscillations of a spherical pendulum," *Quarterly of Applied Mathematics*, vol. 20, no. 1, pp. 21–32, 1962.

[9] P. R. Sethna and A. K. Bajaj, "Bifurcations in dynamical systems with internal resonance," *Journal of Applied Mechanics*, vol. 45, no. 4, pp. 895–902, 1978.

[10] J. Fox and N. Goulbourne, "On the dynamic electromechanical loading of dielectric elastomer membranes," *Journal of the Mechanics and Physics of Solids*, vol. 56, no. 8, pp. 2669–2686, 2008.

[11] J. Fox and N. Goulbourne, "Electric field-induced surface transformations and experimental dynamic characteristics of dielectric elastomer membranes," *Journal of the Mechanics and Physics of Solids*, vol. 57, no. 8, pp. 1417–1435, 2009.

[12] A. Alibakhshi, S. Dastjerdi, M. Malikan, and V. A. Eremeyev, "Nonlinear free and forced vibrations of a hyperelastic

micro/nanobeam considering strain stiffening effect," *Nanomaterials*, vol. 11, p. 3066, 2021.

[13] A. H. Nayfeh, D. T. Mook, and P. Holmes, "Nonlinear oscillations," *Journal of Applied Mechanics*, vol. 47, no. 3, p. 692, 1980.

[14] D. Kumar, J. Singh, and D. Baleanu, "A hybrid computational approach for Klein–Gordon equations on Cantor sets," *Nonlinear Dynamics*, vol. 87, no. 1, pp. 511–517, 2017.

[15] A. M. Lyapunov and J. A. Walker, "The general problem of the stability of motion," *Journal of Applied Mechanics*, vol. 61, no. 1, pp. 226-227, 1994.

[16] G. Adomian, "Solving Frontier problems of physics: the decomposition method, with a preface by Yves Cherruault," *Fundamental Theories of Physics*, p. 1, Kluwer Academic Publishers Group, Dordrecht, 1994.

[17] M. Najafi, H. Massah, and M. Daemi, "On the application of Adomian decomposition method and oscillation equations," in *Proceedings of the 9th WSEAS International Conference on Applied Mathematics (MATH'06)*, Istanbul, Turkey, May 2006.

[18] J. H. He, "Preliminary report on the energy balance for nonlinear oscillations," *Mechanics Research Communications*, vol. 29, no. 2-3, pp. 107–111, 2002.

[19] J. H. He, "Variational iteration method–a kind of non-linear analytical technique: some examples," *International Journal of Non-Linear Mechanics*, vol. 34, no. 4, pp. 699–708, 1999.

[20] D. Younesian, Z. Saadatnia, and H. Askari, "Analytical solutions for free oscillations of beams on nonlinear elastic foundations using the variational iteration method," *Journal of Theoretical and Applied Mechanics*, vol. 50, pp. 639–652, 2012.

[21] S. Rehman, A. Hussain, J. U. Rahman, N. Anjum, and T. Munir, "Modified Laplace based variational iteration method for the mechanical vibrations and its applications," *Acta Mechanica et Automatica*, no. 2, pp. 98–102, 2022.

[22] H. Mehmet Baskonus, W. Gao, H. Rezazadeh et al., "New classifications of nonlinear Schrödinger model with group velocity dispersion via new extended method," *Results in Physics*, vol. 31, Article ID 104910, 2021.

[23] M. Arfan, K. Shah, A. Ullah, M. Shutaywi, P. Kumam, and Z. Shah, "On fractional order model of tumor dynamics with drug interventions under nonlocal fractional derivative," *Results in Physics*, vol. 21, Article ID 103783, 2021.

[24] M. Gubes, H. A. Peker, and G. Oturanç, "Application of differential transform method for el nino southern oscillation (enso) model with compared adomian decomposition and variational iteration methods," 2013, https://arxiv.org/abs/1307.7514.

[25] S. Liao and S. Sherif, "Beyond perturbation: introduction to the homotopy analysis method," *Applied Mechanics Reviews*, vol. 57, no. 5, pp. B25–B26, 2004.

[26] S. Liao, "Homotopy analysis method: a new analytical technique for nonlinear problems," *Communications in Nonlinear Science and Numerical Simulation*, vol. 2, pp. 95–100, 1997.

[27] H. Rezazadeh, M. Odabasi, K. U. Tariq, R. Abazari, and H. M. Baskonus, "On the conformable nonlinear Schrödinger equation with second order spatiotemporal and group velocity dispersion coefficients," *Chinese Journal of Physics*, vol. 72, pp. 403–414, 2021.

[28] M. Hosen, M. Chowdhury, M. Ali, and A. Ismail, "A new analytical technique for solving nonlinear non-smooth oscillators based on the rational harmonic balance method," *Proceedings of the Second International Conference on the Future of ASEAN (ICoFA) 2017–Volume 2*, pp. 453–463, Springer, Singapore, 2018.

[29] S. Ganji, D. D. Ganji, A. Davodi, and S. Karimpour, "Analytical solution to nonlinear oscillation system of the motion of a rigid rod rocking back using max–min approach," *Applied Mathematical Modelling*, vol. 34, no. 9, pp. 2676–2684, 2010.

[30] M. Mohammadian, "Nonlinear free vibration of damped and undamped bi-directional functionally graded beams using a cubic-quintic nonlinear model," *Composite Structures*, vol. 255, Article ID 112866, 2021.

[31] G. Sobamowo and A. Yinusa, "Power series-aftertreatment technique for nonlinear cubic duffing and double-well duffing oscillators," *Journal of Computational and Applied Mechanics*, vol. 48, pp. 297–306, 2017.

[32] M. Farhan, Z. Omar, F. Mebarek-Oudina et al., "Implementation of the one-step one-hybrid block method on the nonlinear equation of a circular sector oscillator," *Computational Mathematics and Modeling*, vol. 31, no. 1, pp. 116–132, 2020.

[33] Z. Y. Ren, "The frequency-amplitude formulation with $\omega 4$ for fast insight into a nonlinear oscillator$\omega 4$ for fast insight into a nonlinear oscillator," *Results in Physics*, vol. 11, pp. 1052-1053, 2018.

[34] H. L. Zhang, "Application of He's amplitude–frequency formulation to a nonlinear oscillator with discontinuity," *Computers & Mathematics with Applications*, vol. 58, no. 11-12, pp. 2197-2198, 2009.

[35] S. A. Pasha, Y. Nawaz, and M. S. Arif, "The modified homotopy perturbation method with an auxiliary term for the nonlinear oscillator with discontinuity," *Journal of Low Frequency Noise, Vibration and Active Control*, vol. 38, no. 3-4, pp. 1363–1373, 2019.

[36] A. Beléndez, C. Pascual, M. Ortuño, T. Beléndez, and S. Gallego, "Application of a modified He's homotopy perturbation method to obtain higher-order approximations to a nonlinear oscillator with discontinuities," *Nonlinear Analysis: Real World Applications*, vol. 10, no. 2, pp. 601–610, 2009.

[37] S. E. Ghasemi, A. Zolfagharian, and D. Ganji, "Study on motion of rigid rod on a circular surface using MHPM," *Propulsion and Power Research*, vol. 3, pp. 159–164, 2014.

[38] H. E. Khah and D. Ganji, "A study on the motion of a rigid rod rocking back and cubic-quintic duffing oscillators by using He's energy balance method," *International Journal of Nonlinear Science*, vol. 10, pp. 447–451, 2010.

[39] G. Sheng and X. Wang, "The dynamic stability and nonlinear vibration analysis of stiffened functionally graded cylindrical shells," *Applied Mathematical Modelling*, vol. 56, pp. 389–403, 2018.

[40] H. Ahmadi and K. Foroutan, "Nonlinear vibration of stiffened multilayer FG cylindrical shells with spiral stiffeners rested on damping and elastic foundation in thermal environment," *Thin-Walled Structures*, vol. 145, Article ID 106388, 2019.

[41] Y. Khan, Q. Wu, H. Askari, Z. Saadatnia, and M. Kalami-Yazdi, "Nonlinear vibration analysis of a rigid rod on a circular surface via Hamiltonian approach," *Mathematical and Computational Applications*, vol. 15, no. 5, pp. 974–977, 2010.

[42] M. Abul-Ez, G. M Ismail, and M. M El-Moshneb, "Analytical solutions for free vibration of strongly nonlinear oscillators," *Information Sciences Letters*, vol. 4, p. 7, 2015.

[43] N. A. Khan, M. Sulaiman, A. J. Aljohani, M. A. Bakar, and Miftahuddin, "Mathematical models of CBSC over wireless channels and their analysis by using the LeNN-WOA-NM

algorithm," *Engineering Applications of Artificial Intelligence*, vol. 107, Article ID 104537, 2022.

[44] N. A. Khan, M. Sulaiman, P. Kumam, and F. K. Alarfaj, "Application of Legendre polynomials based neural networks for the analysis of heat and mass transfer of a non-Newtonian fluid in a porous channel," *Advances in Continuous and Discrete Models*, vol. 2022, pp. 7–32, 2022.

[45] N. A. Khan, M. Sulaiman, C. A. Tavera Romero, and F. S. Alshammari, "Analysis of nanofluid particles in a duct with thermal radiation by using an efficient metaheuristic-driven approach," *Nanomaterials*, vol. 12, no. 4, p. 637, 2022.

[46] M. Rooman, M. A. Jan, Z. Shah, P. Kumam, and A. Alshehri, "Entropy optimization and heat transfer analysis in MHD Williamson nanofluid flow over a vertical Riga plate with nonlinear thermal radiation," *Scientific Reports*, vol. 11, pp. 18386–18414, 2021.

[47] N. A. Khan, M. Sulaiman, C. A. Tavera Romero, G. Laouini, and F. S. Alshammari, "Study of rolling motion of ships in random beam seas with nonlinear restoring moment and damping effects using neuroevolutionary technique," *Materials*, vol. 15, no. 2, p. 674, 2022.

[48] N. A. Khan, M. Sulaiman, P. Kumam, and A. J. Aljohani, "A new soft computing approach for studying the wire coating dynamics with Oldroyd 8-constant fluid," *Physics of Fluids*, vol. 33, no. 3, Article ID 036117, 2021.

[49] J. Lu, L. Ma, and Y. Sun, "Analysis of the nonlinear differential equation of the circular sector oscillator by the global residue harmonic balance method," *Results in Physics*, vol. 19, Article ID 103403, 2020.

[50] H. Mirgolbabaee, S. Tahernejad Ledari, N. Mohammad Zadeh, and D. Domiri Ganji, "Investigation of the nonlinear equation of the circular sector oscillator by Akbari-Ganji's method," *Journal of Taibah University for Science*, vol. 11, no. 6, pp. 1110–1121, 2017.

[51] X. Du, K. Farrahi, and M. Niranjan, "Transfer learning across human activities using a cascade neural network architecture," in *Proceedings of the 23rd international symposium on wearable computers*, pp. 35–44, London, U.K, September 2019.

[52] B. Warsito, R. Santoso, H. Yasin, and Suparti, "Cascade forward neural network for time series prediction," *Journal of Physics: Conference Series*, vol. 1025, Article ID 012097, 2018.

[53] Y. Zhang, J. Lin, Z. Hu, N. A. Khan, and M. Sulaiman, "Analysis of third-order nonlinear multi-singular emden–fowler equation by using the LeNN-WOA-NM algorithm," *IEEE Access*, vol. 9, pp. 72111–72138, 2021.

Hindawi
Advances in Materials Science and Engineering
Volume 2022, Article ID 2713524, 9 pages
https://doi.org/10.1155/2022/2713524

Research Article

Mechanical Properties and Accuracy Evaluation of 3D Printing Based on Value in the Munsell Color System

Jianping Huang,[1] Wanxiang Ye,[2] Guihua Ye,[2] Qi Jia,[3] Kelun Li,[3] Jiawen Kong,[3] Heng Bo Jiang,[3] Qing Lan,[1] and Liming Yu[1]

[1]*Department of Stomatology, Affiliated Hospital of Guangdong Medical University, First Clinical Medical College, Guangdong Medical University, Zhanjiang, Guangdong, China*
[2]*Department of Stomatology, Dongguan Hospital of Integrated Traditional Chinese and Western Medicine, Dongguan, Guangdong, China*
[3]*The Conversationalist Club, School of Stomatology, Shandong First Medical University, Jinan, Shandong, China*

Correspondence should be addressed to Heng Bo Jiang; hengbojiang@foxmail.com and Liming Yu; 365664822@qq.com

Received 13 May 2022; Accepted 2 June 2022; Published 29 June 2022

Academic Editor: Lan Huang

Aim. Printing parameters have been studied extensively to improve printing performance, while resins have been studied to a lesser extent. Therefore, we explore the impact of value in the Munsell color system on the mechanical properties and accuracy of printed products. *Materials and Methods*. Resins having different values were prepared by mixing transparent resin and color pastes. We used plate models for mechanical measurement, crown-and bridge models for accuracy measurement, and disc models for color measurement. *Results*. The Group E resin, which had the lowest value, had the minimum ultimate flexural strength (61.199 MPa) and a relatively low elastic modulus (19.015 MPa). Excluding the *d* index, no significant difference in accuracy was observed. In terms of the *d* index of trueness, the result of the Group E resin was significantly low. The relative errors of trueness were less than 0.0727 μm. The relative errors of precision were less than 0.0093 μm. *Conclusion*. The value of a resin affects the mechanical properties and accuracy of printed products. It is better to secure flexural strength by using a lower-value resin. High-value resins have relatively low accuracies.

1. Introduction

Three-dimensional (3D) printing, also called additive manufacturing, refers to the fabrication of objects through the material deposition. 3D printing is widely used in aerospace, industrial, medical, and multiple other domains [1]. In dentistry, 3D printing can help reduce the time required for cumbersome tasks such as dental restoration and the fabrication of denture bases [2]. In recent years, 3D printing has evolved rapidly, and many related technologies have emerged, including vat photopolymerization, material extrusion, powder bed fusion, and material jetting. Among these 3D printing technologies, vat photopolymerization is the earliest 3D printing technique [3, 4].

Digital light processing (DLP) is a vat photopolymerization technique in which a 3D object is built in a layer-by-layer fashion through localized photopolymerization of liquid resins [5]. The DLP technique has the advantages of high printing speed and high precision of finished products. Owing to its high accuracy, this technique is used to manufacture complex or sophisticated medical devices [6].

Photocurable resins are mainly composed of a resin matrix and a photoinitiator system [7]. Photoinitiator systems usually consist of photoinitiators and coinitiators, which significantly influence the degree of conversion of photocurable dental resins. Under a light of appropriate wavelength and intensity (UV or visible light), the photoinitiator is activated, and it interacts with the coinitiator to

polymerize [8]. Owing to differences in the ability of resins of different colors to absorb different light sources, the final cured product is influenced by the color of the light source used to illuminate the resin. Therefore, the use of resins of different colors may affect the quality of 3D-printed products. Lee et al. [9] used spectrophotometry to study the effect of layer thickness and printing orientation on the color of 3D printing resins. The results indicated that different layer thicknesses and print orientations significantly affect the color stability and dyeability of resins. Moreover, the degree of discoloration of a print resin varies with time. Other factors that influence the quality of 3D-printed products fabricated using the DLP technique include exposure time, wavelength of light, and amount of power supplied [5].

The Munsell color system was the first system for systematically representing the color in three dimensions. This color system allows for accurate color specification and matching in science, art, and industries by defining a coordinate system for all color perceptions [10]. The Munsell color system usually describes color through the three dimensions of value, chroma, and hue. As a standard system for color specification, it has been widely used in color science. In dentistry, the Munsell color system can be used to define the color range of natural human teeth. In recent years, several scholars have used the Munsell color system to evaluate the accuracy of tooth color or the optimal parameters of 3D printers [11, 12]. The Munsell color system has an increasingly important role in dentistry.

In the dental field, 3D-printed products with superior mechanical properties and accuracy can help with the maintenance of normal prosthesis function under the action of chewing stress [13]. In this study, we aim to combine the Munsell color system with a DLP 3D printer to explore the effect of the value dimension of color on the mechanical properties and accuracy (including trueness and precision) of 3D-printed products. The results can provide a color reference for the clinical production of restorative implants. Moreover, the results of this study can be used to identify the experimental reference conditions for color factors, which can be used in other studies, and minimize the influence of color factors on experimental results. In the experiment conducted herein, we establish two null hypotheses: the value of the resin will not affect the mechanical properties of DLP 3D-printed products, and the value of the resin will not affect the accuracy of DLP 3D-printed products.

2. Materials and Methods

2.1. Preparation of Resin. Clear resin (Basic Clear, Anycubic, China) was used as the starting material in this study. We used small amounts of black and white pigments (Black/White, Xin Jia Yi, China) to obtain black and white resins, respectively (light from the light source of the DLP printer can pass through these resins to ensure that they were not left uncured). The prepared black and white resins were mixed homogeneously in the volume ratios of 1 : 2, 1 : 1, and 2 : 1 to investigate the relationship between the color parameters and the mechanical properties and accuracy of the material in the two intervals of black and white. All mixing processes were carried out under shaded conditions with slow shaking to prevent resin denaturation and reduce bubble generation. We named the black resin and white resin with volume ratios of 0 : 1, 1 : 2, 1 : 1, 2 : 1, and 1 : 0 and the clear resin without any added pigment as A, B, C, D, E, and F, respectively, in this study, and their parameters are listed in Table 1.

2.2. CAD Design and 3D Printing. The three types of disc models (for color measurement) based on ISO-4660 [14], a plate model (for mechanical properties) based on ISO-20795-1 [15], and a crown-and-bridge model (for accuracy evaluation) based on ISO-12836 [16] were designed using AutoCAD (v.2021, Autodesk, USA), as shown in Figure 1. The five models were exported in standard tessellation language (STL) format with the highest accuracy and highest number of point clouds that the software can provide. The models were then imported into a slicing software suite (Photon Workshop v. 2.1, Anycubic, China) and sliced using a specific slice parameter by referring to the recommendations of the 3D printer manufacturer (layer thickness, 0.01 mm; normal exposure time 1.50 s; off time, 2.00 s).

The slice files were subsequently imported into the 3D printer and printed at room temperature (approximately 25°C). Six units of each of the five models were printed at the same time. The models were subjected to postprocessing immediately after printing, which included cleaning, drying, and placing the models in an ultraviolet light box for additional polymerization (crown-and-bridge model, plate model, and disc model; 10 min). The light box delivered a wavelength of 400–405 nm and a power of 15 W. Additionally, the plate models were polished using P500 and P1200 grinding papers to a thickness of approximately 3.3 mm. Photographs of the fabricated models are shown in Figure 1.

2.3. Color Measurement. According to ISO-4660, three types of disc models were printed for color measurement. (1.6 mm × 1.4 mm; 0.8 mm × 1.4 mm; 2.4 mm × 1.4 mm). These models were placed on a flat surface against matt white and black backgrounds. The models were properly aligned with the center of the color spectrophotometer's receiver (CM-26 dG, KONICA MINOLTA, JPN) to obtain accurate readings. All procedures were carried out under shaded conditions. The results were recorded using a 2° standard observer and the CIE standard illuminant D65.

2.4. Mechanical Properties. According to ISO-20795-1, we compared the ultimate flexural strength and elastic modulus of six groups of resins with those of the plate models. A universal testing machine (Z010, ZwicRoell, GER) with a constant displacement rate of 5 mm/min and a distance of 50 mm between the supports shall was used in this study. The approximate dimensions of the plate models were 60 mm × 10 mm × 3.3 mm ($N = 6$).

By referring to the data in Table 1, we selected a curve in the same group of samples as the representative curve of this group, which reflect the data in the table more intuitively. The elastic

Table 1: Groups with resins of different values.

Groups	Volume ratio of black and white resin	Value (L^*)		a^*		b^*		Transparency	Disc thickness
		White background	Black background	White background	Black background	White background	Black background		
A	0 : 1	82.95	50.67	−2.39	−2.54	10.00	−0.85	34.06	0.8
		79.46	53.37	−2.38	−3.14	11.89	0.26	28.57	1.6
		74.33	55.29	−2.21	−3.46	12.85	1.68	22.11	2.4
B	1 : 2	67.21	38.90	−0.56	−0.77	8.47	−1.13	29.90	0.8
		56.61	38.50	0.00	−0.78	7.31	−1.29	20.06	1.6
		48.85	37.37	0.30	−0.81	6.10	−0.13	13.11	2.4
C	1 : 1	63.79	36.33	−0.39	−0.23	7.69	−1.34	28.91	0.8
		53.67	34.89	0.21	−0.23	6.82	−1.59	20.58	1.6
		45.39	33.78	0.58	−0.24	5.54	−1.58	13.64	2.4
D	2 : 1	67.46	33.50	−0.67	0.11	7.49	−1.40	35.11	0.8
		51.06	31.41	0.22	0.10	7.02	−1.36	21.36	1.6
		42.47	30.12	0.71	0.26	5.00	−1.94	14.17	2.4
E	1 : 0	63.75	30.88	−0.82	0.22	7.23	−0.78	33.85	0.8
		50.21	29.36	−0.16	0.41	7.14	−1.10	22.43	1.6
		39.27	27.25	0.34	0.45	5.41	−1.05	13.65	2.4
F	Clear resin	86.93	36.27	−2.23	−0.14	8.32	−0.94	51.54	0.8
		84.44	35.62	−2.34	−0.20	10.78	−0.38	50.13	1.6
		82.48	35.85	−2.56	−0.42	11.45	0.20	48.02	2.4

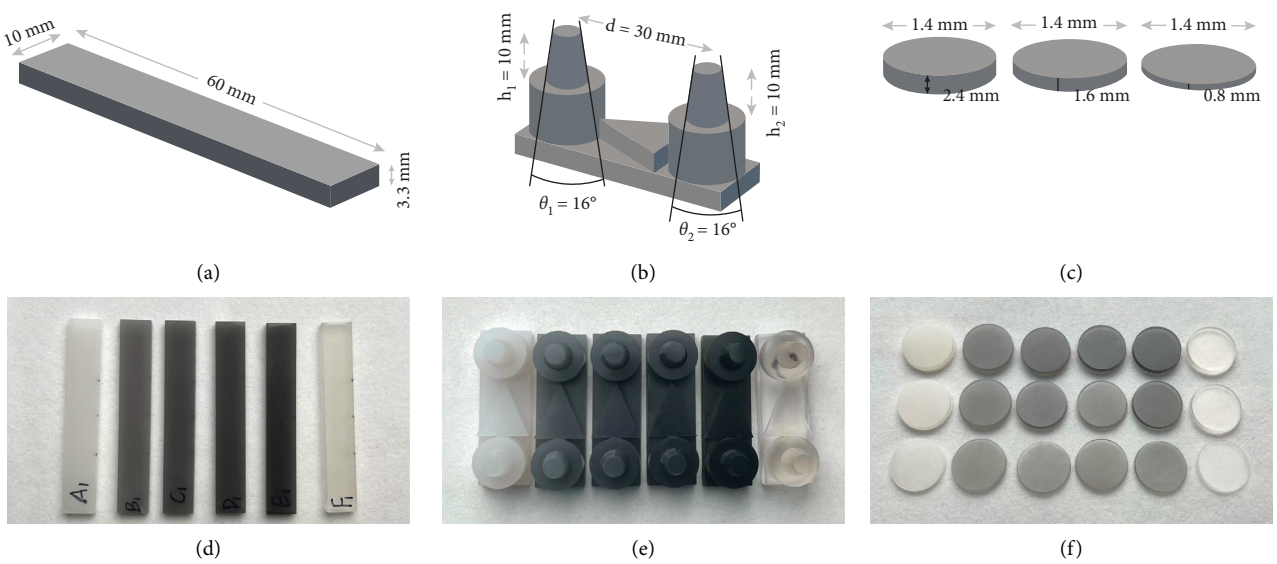

Figure 1: Schematics and actual photographs of plate model (a and d), crown-and bridge model (b and e), and disc model (c and f).

modulus was determined from the slope of the initial linear part of the strength-strain curves (Figure 2).

The ultimate flexural strength was calculated using the following equation:

$$\text{Ultimate flexural strength} = \frac{3Fl}{2wt^2}, \quad (1)$$

where F is the maximum load exerted on the specimen in Newtons; l is the distance between the supports in millimeters (50 mm in this study); w is the width of the specimen in millimeters; t is the thickness of the specimen in millimeters.

2.5. Accuracy Evaluation. According to ISO-12836, we used the crown-and-bridge models to evaluate the accuracy of printing resins of different values. A coordinate measuring machine (CMM, Axiom too CNC, Aberlink, UK) with a probe head (PH10T, Aberlink, UK) was used to measure the indexes of the models (scale resolution: 0.5 μm). The probe diameter (TP20, Standard Force, M2, Renishaw, UK) was 1 mm. The model was held tightly in a vise to prevent any change in its coordinates during measurement. All measurement processes were conducted by the same operator by manually selecting the coordinates to be measured; then, the machine automatically ran the final measurement to eliminate the effect of the strength of human measurements on the results. The planes, lines, and cones constructed during the measurement process were almost always placed at the

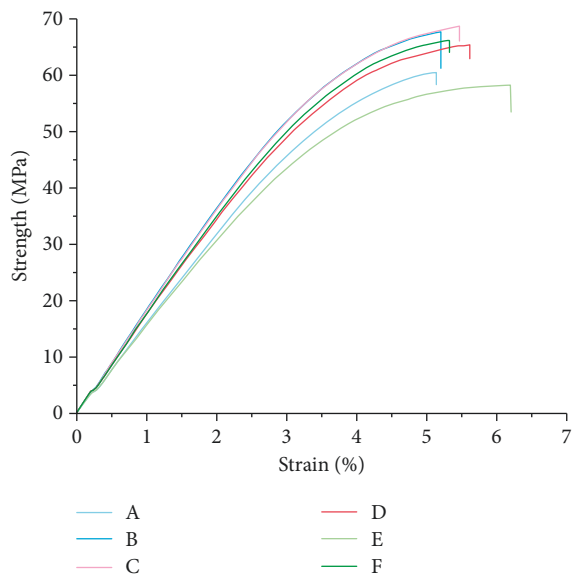

Figure 2: Strength-strain curves of resins having different values.

same position on each model to eliminate the effect of choice of measurement range on the results. Each angle of the probe was calibrated before each group of measurements. All measurement processes were conducted at 20°C, as recommended by the manufacturer. The following indexes were used: cone height (h_1, h_2), cone angle (θ_1, θ_2), and cone distance (d). The gold standard is shown in Figure 1, and its value is the same as that designed using AutoCAD ($N = 6$).

The trueness, precision, and their errors were calculated using the following equations: [17].

$$\text{Truness} = |(b_R - b_M)|, \tag{2}$$

$$\text{Precision} = |(b_A - b_M)|, \tag{3}$$

$$\Delta b_M = \left|\frac{(b_R - b_M)}{b_R}\right|, \tag{4}$$

$$\Delta S(b_M) = \left|\frac{S(b_M)}{b_R}\right|, \tag{5}$$

where b_R is the standard reference values of the indexes (height, angle, and distance) of the model (*in this study, height = 10 mm, angle = 16°, and distance = 30 mm*); b_M is the measured values of the indexes (height, angle, and distance) and angle of the model; b_A is the is the average of the measured values of the indexes (height, angle, and distance) of the model; Δb_M is the relative error of trueness; $\Delta S(b_M)$ is the relative error of precision; $S(b_M)$ is the standard deviation of measured values of the indexes (height, angle, and distance) of the model.

2.6. Statistical Analysis. All data were subjected to a one-way analysis of variance (ANOVA) and Tukey's multiple comparison post hoc test (Origin Pro 2022, Origin Lab, USA). ∗ denotes $p < 0.05$, ∗∗ denotes $p < 0.01$, and ∗∗∗ denotes $p < 0.001$.

Table 2: Mean ± standard deviation of mechanical properties of resins having different values.

Groups	Ultimate flexural strength (MPa)	Elastic modulus (MPa)
A	64.274 ± 1.036	18.645 ± 0.872
B	65.786 ± 2.689	20.393 ± 0.665
C	66.054 ± 2.445	19.870 ± 0.624
D	64.320 ± 1.358	19.782 ± 0.438
E	61.199 ± 2.191	19.015 ± 0.827
F	65.118 ± 1.824	19.820 ± 0.727

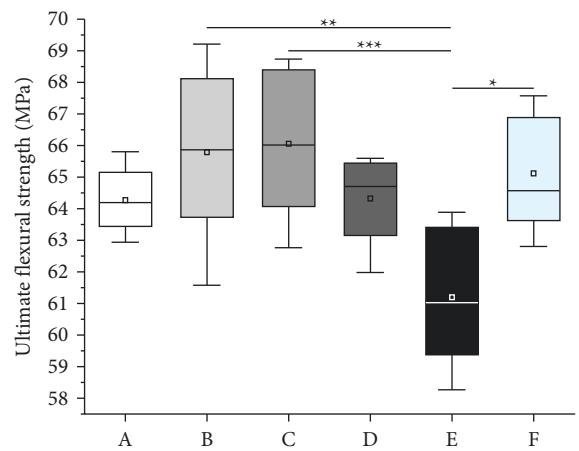

Figure 3: Ultimate flexural strength of resins having different values. $^{*}p < 0.05$, $^{**}p < 0.01$, and $^{***}p < 0.005$.

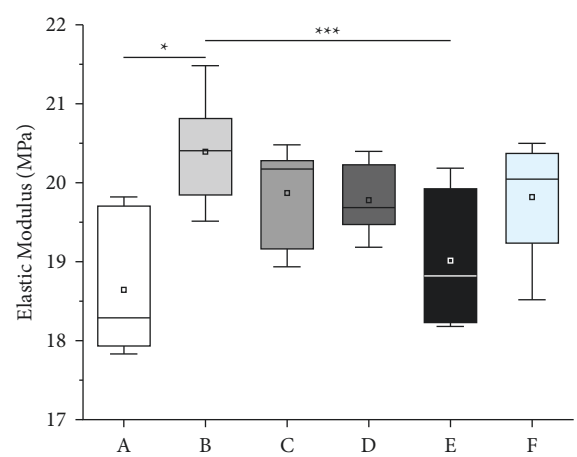

Figure 4: Elastic moduli of resins having different values. $^{*}p < 0.05$, $^{**}p < 0.01$, and $^{***}p < 0.005$.

3. Results

3.1. L^*, a^*, and b^* of Resins of Different Values. The L^*, a^*, and b^* values of discs of three different thicknesses and composed of resins having different values are listed in Table 2. For discs of the same thickness, as the proportion of

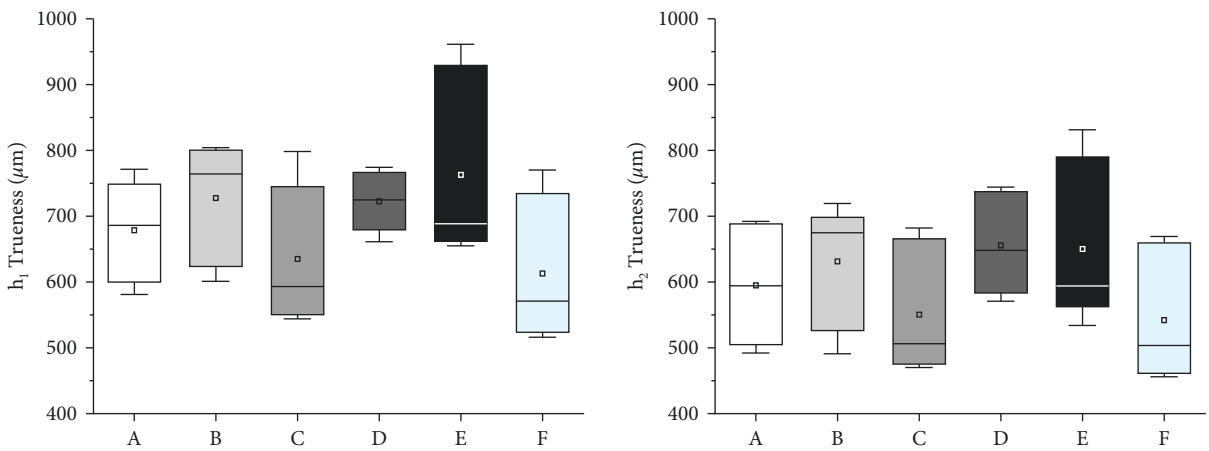

Figure 5: Boxplots of trueness for height (h).

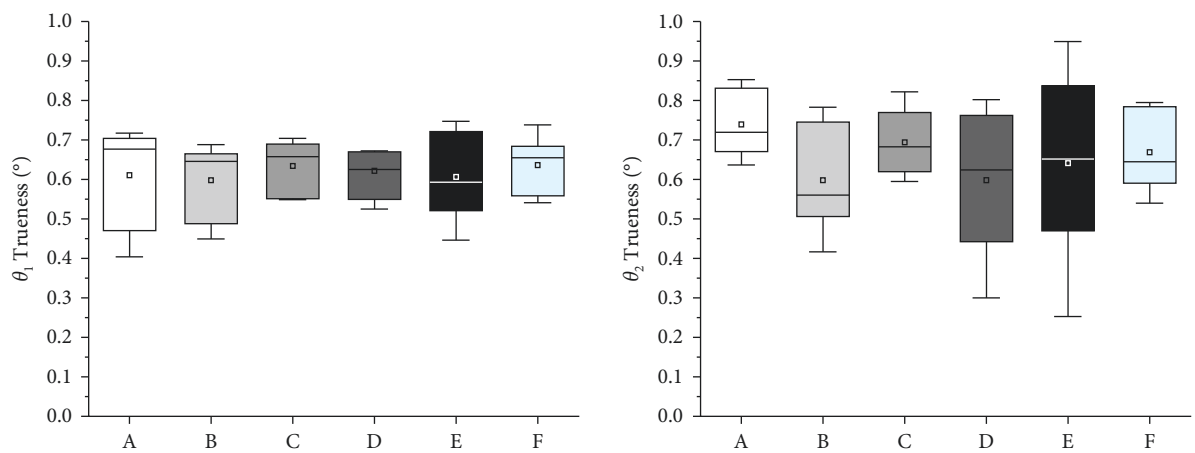

Figure 6: Boxplots of trueness for angle (θ).

black resin increased, L decreased. Except for the case of Group A on a black background, L decreased as the disc thickness increased. Based on the three-layer thicknesses, the transparency of Group A resins was higher than that of resins belonging to other groups (except Group F). The transparency of the Group F resin (clear resin) was significantly higher than those of the other groups.

3.2. Mechanical Properties of Resin of Different Values. Figure 3 and Table 2 show and summarize, respectively, the ultimate flexural strength of the six resins having different values. Except for the Group A resin, the ultimate flexural strengths of the resins belonging to the other groups decreased as their value decreased. Group E resins, which had the lowest value, had the minimum ultimate flexural strength (61.199 MPa), which was significantly lower than those of Groups B ($p < 0.01$), C ($p < 0.005$), and E ($p < 0.05$). The ultimate flexural strength of the gray resin was higher in the higher-value groups (B and C), while the ultimate flexural strength of Group A resins, which had the highest value, was less than those of Group B and C resins.

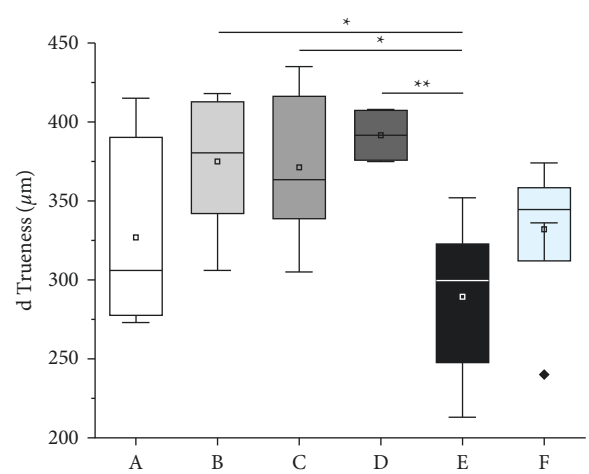

Figure 7: Boxplots of trueness for distance (d). $^{*}p < 0.05$, $^{**}p < 0.01$, $^{***}p < 0.005$.

Additionally, the ultimate flexural strength of the clear resin was relatively high, second only to those of Group B and C resins.

Table 3: Mean trueness ± standard deviation (SD) of crown-and bridge models of resins having different values.

Groups	h_1 (μm)	h_2 (μm)	θ_1 (°)	θ_2 (°)	d (μm)
A	678.500 ± 81.186	594.667 ± 91.101	0.611 ± 0.130	0.739 ± 0.087	326.833 ± 59.449
B	727.167 ± 88.984	631.333 ± 93.146	0.598 ± 0.098	0.598 ± 0.136	375.00 ± 42.019
C	634.500 ± 103.732	550.167 ± 96.013	0.634 ± 0.068	0.694 ± 0.086	371.167 ± 46.275
D	722.167 ± 50.070	655.500 ± 79.644	0.621 ± 0.064	0.598 ± 0.196	391.500 ± 14.405
E	762.500 ± 138.963	650.167 ± 122.156	0.606 ± 0.111	0.642 ± 0.238	289.333 ± 47.886
F	612.667 ± 107.224	541.833 ± 97.315	0.636 ± 0.073	0.669 ± 0.100	332.00 ± 47.079

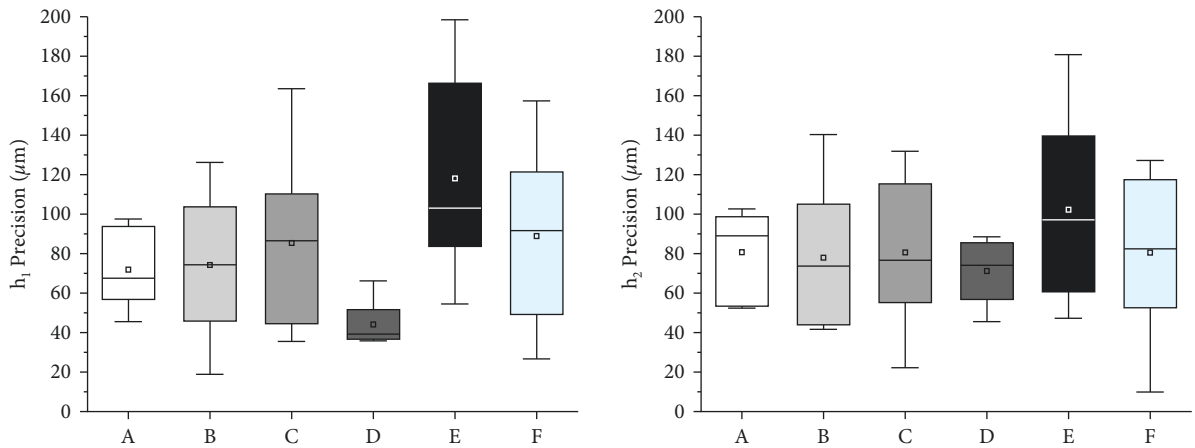

Figure 8: Boxplots of precision for height (h).

Figure 4 and Table 2 show and summarize, respectively, the elastic modulus of the six resins having different values. Similar to the results of ultimate flexural strength, the elastic modulus of the resins belonging to groups other than Group A basically decreased as their value decreased. The elastic modulus of the clear resin was relatively high, second only to those of groups B and C. The Group B resin had the highest elastic modulus (20.393 MPa), significantly higher than that of Group A (18.645 MPa, $p < 0.05$) and E (19.015 MPa, $p < 0.005$) resins. However, unlike that, Group A, with the highest value, has the lowest elastic modulus (18.645 MPa), and Group E was just above it (19.015 MPa).

3.3. Accuracy of Crown-and-Bridge Models of Different Values. Figures 5–7 and Table 3 show and summarize, respectively, the trueness of the different indexes of the crown-and-bridge model. In terms of the trueness of h and θ, there were no significant differences ($p > 0.05$). However, as for the trueness of d, the trueness of the Group E resin, which had the highest value, was significantly lower than that of Group B ($p < 0.05$), C ($p < 0.05$), and D ($p < 0.01$) resins. As summarized in Table 3, the mean trueness of d for the Group E resin was 289.333, which was the lowest and represents the best trueness. There is a deviation in the trueness value of the Group F resin, and this deviation did not affect the overall statistics.

Figures 8–10 and Table 4 show and summarize, respectively, the precision of the different indexes of the crown-and-bridge model. In terms of precision, none of the groups exhibited significant differences ($p > 0.05$). The measurements of h (118.000, 102.222) and θ (0.170) of Group E resin are highest, which is also higher in the measurement of d (35.553).

Tables 5 and 6 list the relative errors of trueness and precision. The relative errors of trueness are less than 0.0727. The relative errors of precision are less than 0.0093. Overall, the relative errors of precision are lower than those of trueness. Moreover, both types of relative errors exhibit the same trend.

4. Discussion

Based on the results of our study, the null hypothesis that value does not affect the mechanical properties and accuracy of DLP 3D-printed products was rejected. The experiment conducted herein was qualitative. The trend of each data group changed with the variables, and the pros and cons of these changes warrant attention. Moreover, the magnitude of value or the existence of a significant difference between groups may not accurately reflect the results of this study.

According to Table 1, the sample with the lowest value (Group E) has the lowest ultimate flexural strength. Additionally, the elastic modulus of the Group E resin is lower. Tahayeri et al. [18] pointed out that to deeply cure lower-value resins, higher laser intensities are required. Therefore, the curing depth of the black samples may be worse than those of the other samples under the same printing parameters and postprocessing conditions, leading to incomplete curing of black samples and easier bending and breaking. In terms of the mechanical property results, we recommend longer postcuring times for low-brightness printed products to increase the curing depth. Meanwhile,

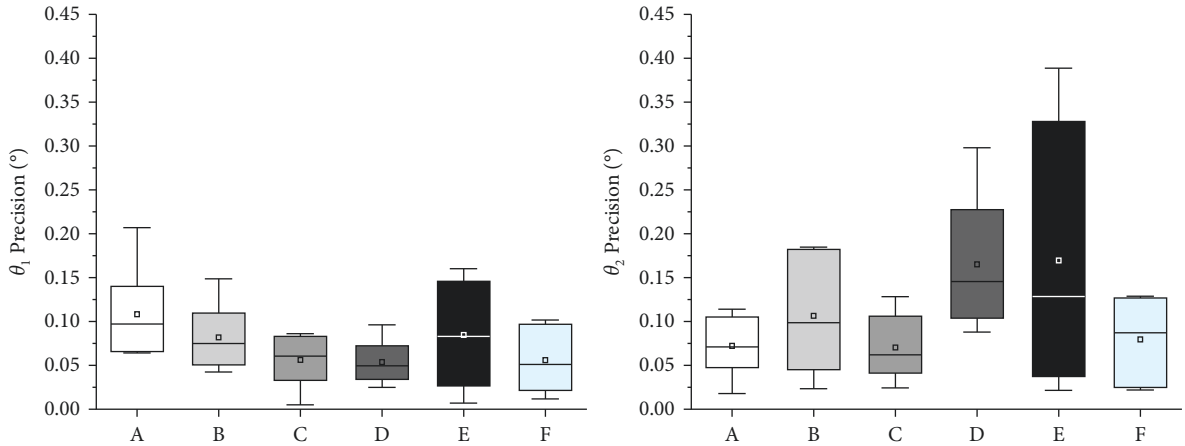

Figure 9: Boxplots of precision for angle (θ).

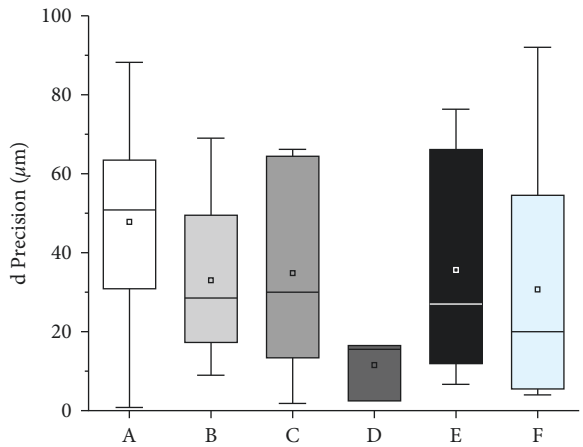

Figure 10: Boxplots of precision for distance (d).

Table 4: Mean precision ± standard deviation (SD) of the crown-and bridge models of resins having different values.

Groups	h_1 (μm)	h_2 (μm)	θ_1 (°)	θ_2 (°)	d (μm)
A	71.833 ± 19.977	80.667 ± 22.157	0.108 ± 0.053	0.072 ± 0.035	47.778 ± 28.194
B	74.111 ± 36.431	77.889 ± 37.366	0.082 ± 0.039	0.106 ± 0.070	33.000 ± 21.420
C	85.333 ± 44.969	80.556 ± 37.836	0.056 ± 0.030	0.070 ± 0.037	34.833 ± 26.179
D	44.000 ± 11.595	71.167 ± 16.293	0.053 ± 0.025	0.165 ± 0.076	11.500 ± 6.986
E	118.000 ± 51.009	102.222 ± 48.815	0.085 ± 0.061	0.170 ± 0.148	*35.556 ± 27.858*
F	88.889 ± 44.895	80.444 ± 41.287	0.056 ± 0.039	0.079 ± 0.049	30.667 ± 32.983

we recommend using a lower-value resin to ensure flexural strength.

The b^* value reflects the measurement along the yellow-blue axis, and the larger the b^* value is, the more yellow the color is [19]. The wavelength of the light emitted by our printer is 405 nm, which represents blue-violet light. As summarized in Table 1, the b^* value of the Group A resin is higher than that of the resins belonging to the other groups, and its mechanical properties are relatively poor in both aspects. This result can possibly be ascribed to the fact that there exists more opaque yellow pigmentation in the resin, which limits the absorption of blue-violet light, thus resulting in poorer mechanical properties. Tahayeri et al. [18] reported that the highest laser intensity was used to print gray resin. This implied that the gray resin absorbed the highest amount of light, which confirmed that it had the best mechanical properties in our experiment.

In addition, Tahayeri et al. [18] reported that the highest and lowest accuracies were achieved when using the white and black resins, respectively. In this study, we did not achieve the highest accuracy when using the white resin but achieved the lowest accuracy when using the black resin. This may be explained by the higher opaque pigmentation of the black resin. Therefore, it is reasonable to assume that the poor printing accuracy achieved when using the black resin may be due to the penetration of light to a depth greater than

Table 5: Relative errors of trueness.

Groups	h_1 (μm)	h_2 (μm)	θ_1 (°)	θ_2 (°)	d (μm)
A	0.0679	0.0595	0.0382	0.0462	0.0109
B	0.0727	0.0631	0.0374	0.0374	0.0125
C	0.0635	0.0550	0.0396	0.0434	0.0124
D	0.0722	0.0656	0.0388	0.0374	0.0131
E	0.0763	0.0650	0.0379	0.0401	0.0096
F	0.0613	0.0542	0.0398	0.0418	0.0111

Table 6: Relative errors of precision.

Groups	h_1 (μm)	h_2 (μm)	θ_1 (°)	θ_2 (°)	d (μm)
A	0.0020	0.0022	0.0068	0.0022	0.0009
B	0.0036	0.0037	0.0051	0.0044	0.0007
C	0.0045	0.0037	0.0035	0.0023	0.0009
D	0.0011	0.0016	0.0033	0.0048	0.0002
E	0.0051	0.0049	0.0053	0.0093	0.0009
F	0.0045	0.0041	0.0035	0.0031	0.0011

the layer thickness corresponding to our setting. Notably, according to the results of a statistical analysis of accuracy (trueness and precision) in this study, a significant difference was found only in the case of the d index of the Group E resin. This may be ascribed to the relatively small degree of dispersion of the d index, which is reflected in the fact that the value and range of the d index along the vertical axis are smaller than those of the other indexes. Moreover, it can be inferred from Tables 5 and 6 that the relative errors of the d index are smaller than those of the other indexes. Considering this aspect, the difference between Group E and the other groups in terms of the d index is not too large. In addition, in terms of the indexes other than the d index, the mean value and dispersion of group E are larger than those of the other groups. Therefore, we believe that the accuracy of the resins with high values is poor. However, the other groups did not exhibit clear maxima and trends in accuracy, and the value range of our study was limited. For this reason, wider value ranges should be studied and discussed in the future.

Interestingly, during the printing process, we found that the printed plate model was thicker than the set value. The height cones of the printed crown-and bridge model were lower than the respective set values. This result may be ascribed to changes in laser intensity during the printing process. When the printer cures thinner layers (thin objects), the metal plate that carries the printed product reflects a greater proportion of the laser light. As the number of cured layers increases (thick object), the reflective effect of the metal plate on the laser decreases.

Although the process of designing and 3D printing dental products is well established and highly individualized, differences in printing parameters and materials used can interfere with the quality of the printed products [20]. In this study, we investigated the influence of photosensitive resin color (value) on the mechanical properties and accuracy of 3D-printed products. We aimed to improve our understanding of the effect of material color on the performance of printed products and provide a color reference for producing clinical dental restorations. However, value accounts for a minor part of the Munsell color system, and more studies must be conducted to explore the Munsell color system in the context of 3D printers. Layer thickness, build direction, angle, intensity, laser speed, curing process, and printing technique are all factors that affect the accuracy of printed models [21]. Aretxabaleta et al. [22] stated that the highest fidelity and accuracy can be achieved with the shortest production time when the printer layer thickness is set to 100 μm. Meanwhile, Alshamrani et al. [23] indicated that the 3D printing layer thickness of 100 μm led to higher flexural strength than those achieved with the layer thicknesses of 25 μm and 50 μm. These results illustrate the need for optimizing the printing parameters. For this reason, we will explore the settings of other parameters in the future.

During the preparation of the plate models, we added support to the 3D-printed samples to satisfy the thickness requirement. When we removed these supports, we attempted to ensure that the models were not stressed. However, some stress may have been induced in them, which would affect their mechanical properties. Another limitation of our study is the print angle. The construction angle of the 3D-printed models in this study was 0°. Osman et al. [24] achieved the best accuracy with the build angle of 135° in their study of the accuracy of 3D printing build orientation on the size of the restoration under DLP processing. Therefore, future studies may consider investigating the effect of value when evaluating the effect of different construction angles.

5. Conclusion

Based on the results of this study, the following conclusions were drawn:

(1) The value of a resin affects the mechanical properties and accuracy of the 3D-printed products.

(2) It is better to secure flexural strength using a lower-value resin.

(3) High-value resins have relatively low accuracy.

Data Availability

The data used to support the findings of this study are included in this article.

Conflicts of Interest

The authors declare that they have no financial or personal relationships with other people or organizations that can inappropriately influence our work.

Authors' Contributions

Jianping Huang and Liming Yu were responsible for the conceptualization; Guihua Ye contributed to the methodology; Qing Lan conducted the validation; Wanxiang Ye and Qi Jia conducted the formal analysis; Kelun Li and Heng Bo Jiang were responsible for data curation; Jianping Huang, Wanxiang Ye, and Jiawen Kong wrote and prepared the

original draft; Heng Bo Jiang, Jianping Huang, and Liming Yu wrote, reviewed, and edited the article. All authors have read and agreed to the published version of the manuscript.

Acknowledgments

This article was supported by the Natural Science Foundation of Guangdong Science and Technology Department (2019A1515110724); Guangdong Medical Science and Technology Fund (A2020151); Guangdong Traditional Chinese Medicine Bureau Fund (20222102); Science and Technology Fund of Dongguan (20211800906063); and "Clinical medicine plus" Science and Technology Collaboration Platform and Project of the Affiliated Hospital of Guangdong Medical University (CLP2021B012).

References

[1] G. Oberoi, S. M Nitsch, K Janjić, and A. S. H. Müller, "3D printing-encompassing the facets of dentistry," *Frontiers in Bioengineering and Biotechnology*, vol. 6, p. 172, 2018.

[2] P. Vasamsetty, T. Pss, D. Kukkala, M. Singamshetty, and S. Gajula, "3D printing in dentistry - e," *Materials Today Proceedings*, vol. 26, pp. 838–841, 2020.

[3] R. Ranjan, D. Kumar, M. Kundu, and S. Chandra Moi, "A critical review on Classification of materials used in 3D printing process," *Materials Today Proceedings*, vol. 61, pp. 43–49, 2022.

[4] D. Khorsandi and A. P. S. S. M. S. A. A. A. F. A. R. M. B. V. F. R. P. Fahimipour, "3D and 4D printing in dentistry and maxillofacial surgery: printing techniques, materials, and applications," *Acta Biomaterialia*, vol. 122, pp. 26–49, 2021.

[5] W. Moon and S. B.-S. Y.-S. R. J.-Y. S. H. Kim, "Dimensional accuracy evaluation of temporary dental restorations with different 3D printing systems," *Materials*, vol. 14, no. 6, p. 1487, 2021.

[6] J. Schweiger, D. Edelhoff, and J.-F. Güth, "3D printing in digital prosthetic dentistry: an overview of recent developments in additive manufacturing," *Journal of Clinical Medicine*, vol. 10, no. 9, p. 2010, 2021.

[7] A. Bagheri and J. Jin, "Photopolymerization in 3D printing," *ACS Applied Polymer Materials*, vol. 1, no. 4, pp. 593–611, 2019.

[8] J. F. Besegato, E. I. A. C. R. V Jussiani, and F. M. B. L. S. C. C. M. G. Salomão, "Effect of light-curing protocols on the mechanical behavior of bulk-fill resin composites," *Journal of the Mechanical Behavior of Biomedical Materials*, vol. 90, pp. 381–387, 2019.

[9] E.-H. Lee, J.-S. Ahn, Y.-J. Lim, H.-B. Kwon, and M.-J. Kim, "Effect of layer thickness and printing orientation on the color stability and stainability of a 3D-printed resin material," *The Journal of Prosthetic Dentistry*, 2022.

[10] S. Cochrane, "The Munsell Color System: a scientific compromise from the world of art," *Studies In History and Philosophy of Science Part A*, vol. 47, pp. 26–41, 2014.

[11] J. Liu, H. Su, W. Hu, L. Zhang, and D. Tao, "A minimal Munsell value error based laser printer model," *Neurocomputing*, vol. 204, pp. 231–239, 2016.

[12] J.-Y. Chang and W.-C. T.-K. J.-C. P.-S. J.-H. C.-C. Chen, "Evaluating the accuracy of tooth color measurement by combining the Munsell color system and dental colorimeter," *The Kaohsiung Journal of Medical Sciences*, vol. 28, no. 9, pp. 490–494, 2012.

[13] B. Henriques and M. J. C. M. R. M. D. F. S. Gasik, "Mechanical and thermal properties of hot pressed CoCrMo-porcelain composites developed for prosthetic dentistry," *Journal of the Mechanical Behavior of Biomedical Materials*, vol. 30, pp. 103–110, 2014.

[14] International Standard (Iso), *4660 - Rubber, Raw Natural — Colour index Test*, International Organization for Standardization, Geneva, Switzerland, 2020.

[15] International Standard (Iso), - *Dentistry — Base Polymers —Part 1: Denture Base Polymers*, International Organization for Standardization, Geneva, Switzerland, 20795-1.

[16] International Standard (Iso) 12836, *Dentistry —Digitizing Devices for CAD/CAM Systems for Indirect Dental Restorations— Test Methods for Assessing Accuracy*, International Organization for Standardization, Geneva, Switzerland, 2015.

[17] S. H. Uhm, J. H. Kim, H. B. Jiang et al., "Evaluation of the accuracy and precision of four intraoral scanners with 70% reduced inlay and four-unit bridge models of international standard," *Dental Materials Journal*, vol. 36, no. 1, pp. 27–34, 2017.

[18] A. Tahayeri and M. A. P. D. A. C. S. J. L. L. E. Morgan, "3D printed versus conventionally cured provisional crown and bridge dental materials," *Dental Materials*, vol. 34, no. 2, pp. 192–200, 2018.

[19] Chap 3, *Phillips Science of Dental Materials*, Elsevier Health Sciences, Amsterdam, Netherlands.

[20] W. Piedra-Cascón, V. R. Krishnamurthy, W. Att, and M. Revilla-León, "3D printing parameters, supporting structures, slicing, and post-processing procedures of vat-polymerization additive manufacturing technologies: a narrative review," *Journal of Dentistry*, vol. 109, Article ID 103630, 2021.

[21] F. Emir, G. Ceylan, and S. Ayyıldız, "In vitro accuracies of 3D printed models manufactured by two different printing technologies," *European Oral Research*, vol. 55, no. 2, pp. 80–85, 2021.

[22] M. Aretxabaleta, A. Unkovskiy, B. Koos, S. Spintzyk, and A. B. Xepapadeas, "Accuracy evaluation of additively and subtractively fabricated palatal plate orthodontic appliances for newborns and infants-an in vitro study," *Materials*, vol. 23, no. 15, p. 4103, 2021.

[23] A. A. Alshamrani, R. Raju, and A. Ellakwa, "Effect of printing layer thickness and postprinting conditions on the flexural strength and hardness of a 3D-printed resin," *BioMed Research International*, vol. 2022, Article ID 8353137, 9 pages, 2022.

[24] R. Osman, N. Alharbi, and D. Wismeijer, "Build angle: does it influence the accuracy of 3D-printed dental restorations using digital light-processing Technology?" *The International Journal of Prosthodontics*, vol. 30, no. 2, pp. 182–188, 2017.

Hindawi
Advances in Materials Science and Engineering
Volume 2022, Article ID 9597155, 8 pages
https://doi.org/10.1155/2022/9597155

Research Article

Prediction of Mg Alloy Corrosion Based on Machine Learning Models

Zhenxin Lu,[1] Shujing Si,[1] Keying He,[1] Yang Ren,[1] Shuo Li,[1] Shuman Zhang,[1] Yi Fu,[1] Qi Jia,[2] Heng Bo Jiang,[2] Haiying Song,[1] and Mailing Hao[1]

[1]*School of Stomatology, Shandong Liming Polytechnic Vocational College, Tai'an, Shandong 271000, China*
[2]*The Conversationalist Club, School of Stomatology, Shandong First Medical University, Jinan, Shandong 250000, China*

Correspondence should be addressed to Heng Bo Jiang; hengbojiang@foxmail.com, Haiying Song; songluzhe@foxmail.com, and Mailing Hao; haoml1965@outlook.com

Received 4 May 2022; Accepted 25 May 2022; Published 8 June 2022

Academic Editor: Lan Huang

Magnesium alloy is a potential biodegradable metallic material characterized by bone-like elastic modulus, which has great application prospects in medical, automotive, and aerospace industries owing to its bone-like elastic modulus, biocompatibility, and lightweight properties. However, the rapid corrosion rates of magnesium alloys seriously limit their applications. This study collected magnesium alloys' corrosion data and developed a model to predict the corrosion potential, based on the chemical composition of magnesium alloys. We compared four machine learning algorithms: random forest (RF), multiple linear regression (MLR), support vector machine regression (SVR), and extreme gradient boosting (XGBoost). The RF algorithm offered the most accurate predictions than the other three machine learning algorithms. The input effects on corrosion potential have been investigated. Moreover, we used feature creation (transforming chemical component characteristics into atomic and physical characteristics) so that the input characteristics were not limited to specific chemical compositions. From this result, the model's application range was widened, and machine learning was used to verify the accuracy and feasibility of predicting corrosion of magnesium alloys.

1. Introduction

Magnesium alloys have excellent application prospects in the medical, automotive, and aerospace industries owing to their bone-like elastic modulus, biocompatibility, and lightweight properties [1–4]. However, the rapid corrosion rates of magnesium alloys seriously limit their broad application [5, 6]. Therefore, developing corrosion-resistant magnesium alloys is vital to increase their application potential.

Alloying is an efficient way to improve the properties of metals since various properties can be enhanced by introducing alloying elements into Mg [7, 8]. Moreover, studying the chemical composition of a magnesium alloy is a vital technique for controlling its corrosion rate. Many scholars have added alloying elements (such as Ca [9, 10], Zn [11, 12], Al [13], Mn [14, 15], Sr [16], and Sn [17, 18]) to increase corrosion resistance of magnesium alloys. However, the corrosion-resistant magnesium alloys depend on local optimization conducted through repeated experiments and constant adjustment of the alloy concentration. Thus, optimizing the alloy composition is vital by testing every possibility. However, this process is costly and requires many human and material resources. Most previous studies have only focused on binary and ternary alloys and have not examined the effects of various elements.

The application of machine learning in studying the alloy has increased in recent years [19, 20]. Machine learning uses experimental data to develop a mathematical model and establish the quantitative relationship between the target attributes and features. This model is used to predict the target alloy properties with different compositions. Machine learning has been widely studied for predicting the corrosivity of low-alloy steels [21–23]. Further, machine learning exhibits excellent prediction accuracy, robust fitting, and analysis

Table 1: Chemical composite features, environment features, and target attributes.

Features		Unit	Descriptions	Data range
Material	Elements	wt%	Al content	0.015–17.000
			Zn content	0.001–30.000
			Mn content	0.002–1.000
			Si content	0.001–1.110
			Fe content	0.001–0.040
			Cu content	0–10.000
			Ca content	0–4.000
			Sr content	0–1.960
			Sn content	0–9.140
Environmental	Cl ion	$mol \cdot L^{-1}$	Chloride ion concentration	0.087–1.026
Target property	I_{corr}	$A \cdot cm^{-2}$	Corrosion current	0–0.167
	E_{corr}	V	Corrosion potential	−2.027–−1.117

ability. However, the prediction of the corrosion rate of a magnesium alloy by machine learning has not been reported.

This study collected corrosion data from the published literature and developed a prediction model for the chemical composition, corrosion potential, and corrosion of magnesium alloys using machine learning. Feature creation was used to broaden the model's applicability.

2. Datasets and Machine Learning

2.1. Corrosion Data and Pretreatment. This study collected material data from the published literature. A total of 164 different alloy compositions were considered, consisting of a primary test environment (chloride ion concentration) and two target properties (corrosion potential and current density). In Table 1, each row of corrosion data has nine material characteristics, one environmental characteristic, and the associated corrosion potential. Table S1 presents the current density.

Most studies did not provide the content of trace alloying components in the chemical composition analysis of magnesium alloy, and these studies marked the components lower than the detection threshold. We used the average value of the original data to fill in the missing values and enhance the accuracy of the machine learning. We selected the logarithm of 10 as the target attribute of the current density since the value of the current density was too small. Finally, all the materials, environmental characteristics, and target attributes were standardized.

2.2. Feature Creation. Predicting the corrosion of magnesium alloys with other materials is impossible because the material characteristics of the model only contained nine elements. Therefore, we applied the feature creation method proposed by Diao et al. [24] to the model's generalization ability and application range. The physical properties of atoms were used to predict the material characteristics. We selected 16 atomic and physical characteristics (Table 2) to replace magnesium alloy's chemical composition. The physical attributes, corresponding to each element, were obtained from the WebElements periodic table [25]. The following equation defines the feature creation method:

$$X = f_{A_1}X^{A_1} + f_{A_2}X^{A_2} + \ldots + f_{A_n}X^{A_n}, \quad (1)$$

Table 2: Atomic and physical characteristics used in feature creation.

Physical property	Descriptions
V	Molar volume
K	Bulk modulus
λ	Thermal conductivity
Mp	Melting point
ΔH_f	Enthalpy of fusion
ΔH_v	Enthalpy of vaporization
ΔH_a	Enthalpy of atomization
R_a	Atomic radius
R_m	Covalent radius of a single molecule
R_v	Van der Waals radii
R_c	Covalent radius
EN_p	Pauling electronegativity
EN_s	Sanderson electronegativity
EN_a	Allred–Rochow electronegativity
E_1	First ionization energy
E_2	Second ionization energy

Table 3: Optimization parameters of each algorithm (other parameters are default).

Models	Parameters	
	E_{corr}	I_{corr}
RF	n_estimators = 150	n_estimators = 183
SVR	Kernel = rbf, C = 100, gramma = 0.1	Kernel = rbf, C = 100, gramma = 0.1
XGBoost	Booster = gbtree, learning_rate = 0.2, n_estimators = 10	Booster = gbtree, learning_rate = 0.3, n_estimators = 10

where X represents one of the physical characteristics of an atom; f_{A_n} stands for the mass fraction of elements; and A_n and X^{A_n} denote the corresponding feature.

2.3. Experimental Procedure. The acquired data were grouped into a training set (70%) and a testing set (30%). The training set was used to optimize the parameters of the prediction model. However, a testing set was used to identify the model's prediction accuracy. Random forest (RF), support vector machine regression (SVR), multiple linear regression (MLR), and extreme gradient boosting

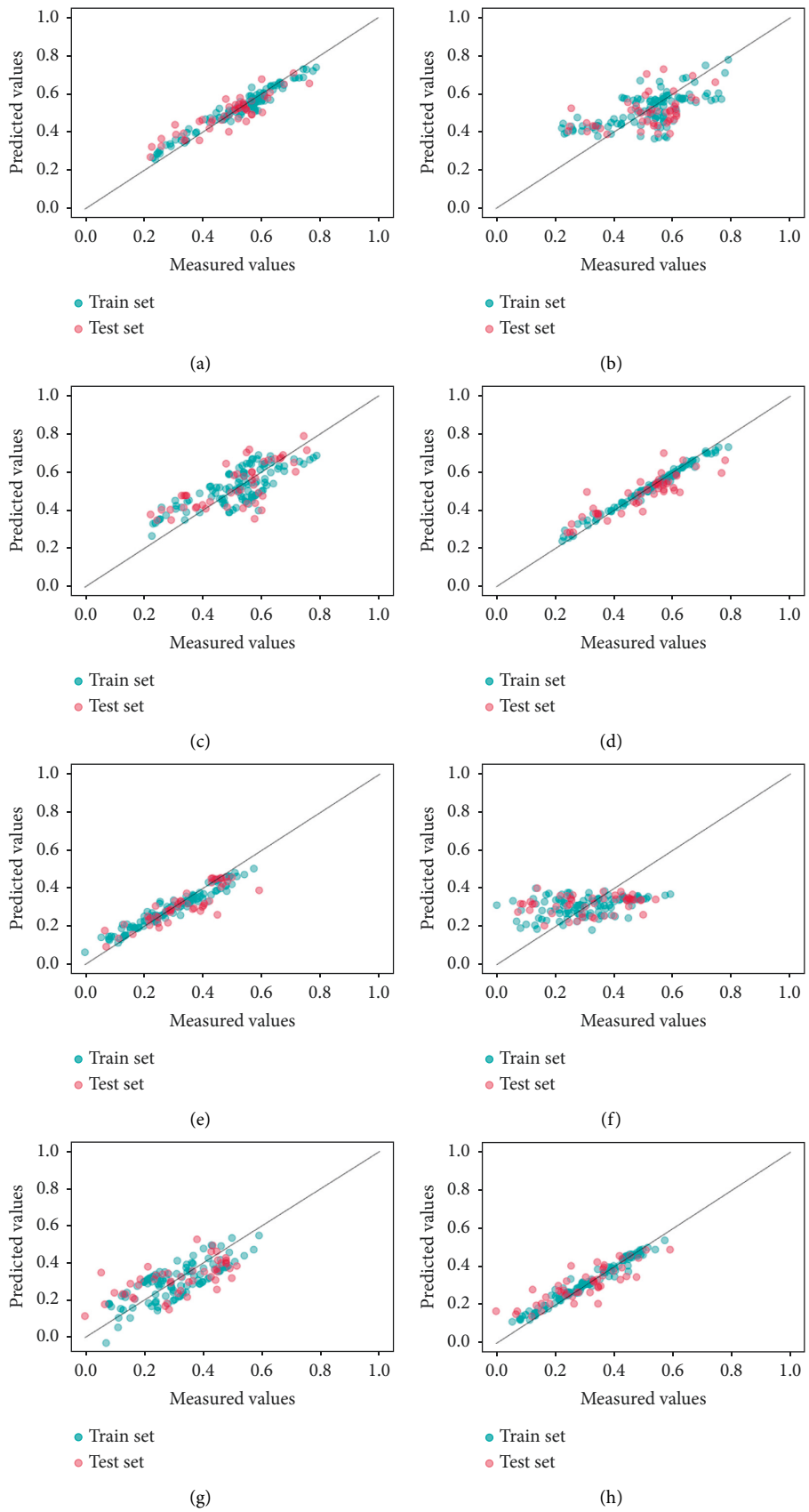

Figure 1: Prediction results for corrosion potential and current density corresponding to the four algorithms. (a–d) Prediction results for corrosion potential by the RF, MLR, SVR, and XGBoost algorithms, respectively. (e–h) Prediction results for current corrosion by RF, MLR, SVR, and XGBoost algorithms, respectively.

Table 4: Prediction accuracy of each algorithm (the R^2 and MAE calculation results for each optimized model in the training set and testing set).

Models	E_{corr}				I_{corr}			
	R^2		MAE		R^2		MAE	
	Training set	Testing set	Training set	Testing set	Training set	Testing set	Training set	Testing set
RF	0.900	0.790	0.025	0.042	0.850	0.730	0.029	0.041
MLR	0.430	0.140	0.079	0.093	0.160	0.040	0.092	0.043
SVR	0.590	0.500	0.067	0.078	0.600	0.400	0.068	0.090
XGBoost	0.970	0.740	0.013	0.049	0.950	0.690	0.020	0.053

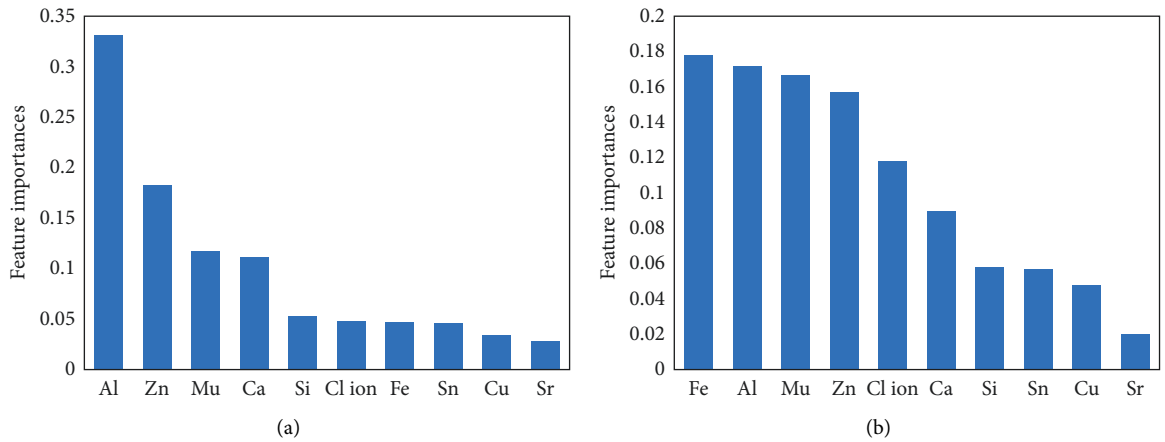

Figure 2: Importance of the input characteristics corresponding to (a) corrosion potential and (b) corrosion current prediction models.

(XGBoost) were used to train the collected data. The optimum parameters of the model were determined using the grid search approach and k-fold cross-validation ($k = 5$). Moreover, we compared the training results of each algorithm and selected the algorithm with the highest accuracy for prediction. The above calculations were performed using Python software and the scikit-learn toolkit for all algorithms, except the XGBoost, which used the XGBoost library [26].

2.4. Evaluation of Model Performance. The ratio of the information, captured by the model, to the information in the actual label was measured. The closer the model is to 1.00, the better the model fit is. The mean absolute error (MAE), which was the average of the absolute error between the predicted value and the actual value, was used to measure the model accuracy. These models are calculated as follows:

$$R^2 = 1 - \frac{\sum_{i=1}^{n} (y_i - \hat{y}_i)^2}{\sum_{i=1}^{n} (y_i - \overline{y_i})^2},$$
$$\mathrm{MAE} = \frac{1}{n} \sum_{i=1}^{n} \left| (y_i - \hat{y}_i)^2 \right|, \quad (2)$$

where y_i represents the measured value; $\hat{y}_i$ stands for the predicted value; and $\overline{y_i}$ is the average value of the measured value.

3. Results and Discussion

3.1. Modeling and Application of Forecasting Models. The optimal parameters corresponding to the prediction models of the four algorithms are listed in Table 3.

Figure 1 shows the prediction results for the corrosion potential and current density, which correspond to the four algorithms. The prediction results were drawn as functions of the measured data, which are equal to the measured data for a perfect prediction model. All the data points fall on the diagonal lines; the closer the data points to the diagonal lines, the more accurate the prediction results. The MLR model had a poor fitting effect on the corrosion potential and current density. The model indicates that the influences of the different elements on the corrosion potential and current density in magnesium alloys are complex, and no superficial linear relationships are established. Moreover, the fitting effect for the SVM on the two target attributes was poor. Both RF and XGBoost models are two integrated techniques that combine two decision trees to improve the model ability and offer excellent fitting effects. Table 4 lists the R^2 and MAE calculation results for each optimized model in the training and testing sets. Both the MLR and SVM models had small R^2 and large MAE values in the testing set and training set, respectively, showing that the fitting effects of MLR and SVM were poor. Although the XGBoost model fitted the training dataset well, it performed poorly on the testing set, which might be due to overfitting. Therefore, the RF model was used in the subsequent analysis.

Table 5: Prediction accuracy of each algorithm (the R^2 and MAE calculation results for each optimized model in the training set and testing set).

Models	E_{corr}				I_{corr}			
	R^2		MAE		R^2		MAE	
	Training set	Testing set	Training set	Testing set	Training set	Testing set	Training set	Testing set
RF	0.850	0.660	0.028	0.056	0.790	0.610	0.030	0.070
MLR	0.470	0.260	0.069	0.100	0.210	0.140	0.080	0.093
SVR	0.520	0.350	0.071	0.089	0.450	0.370	0.080	0.085
XGBoost	0.940	0.530	0.022	0.063	0.950	0.480	0.019	0.078

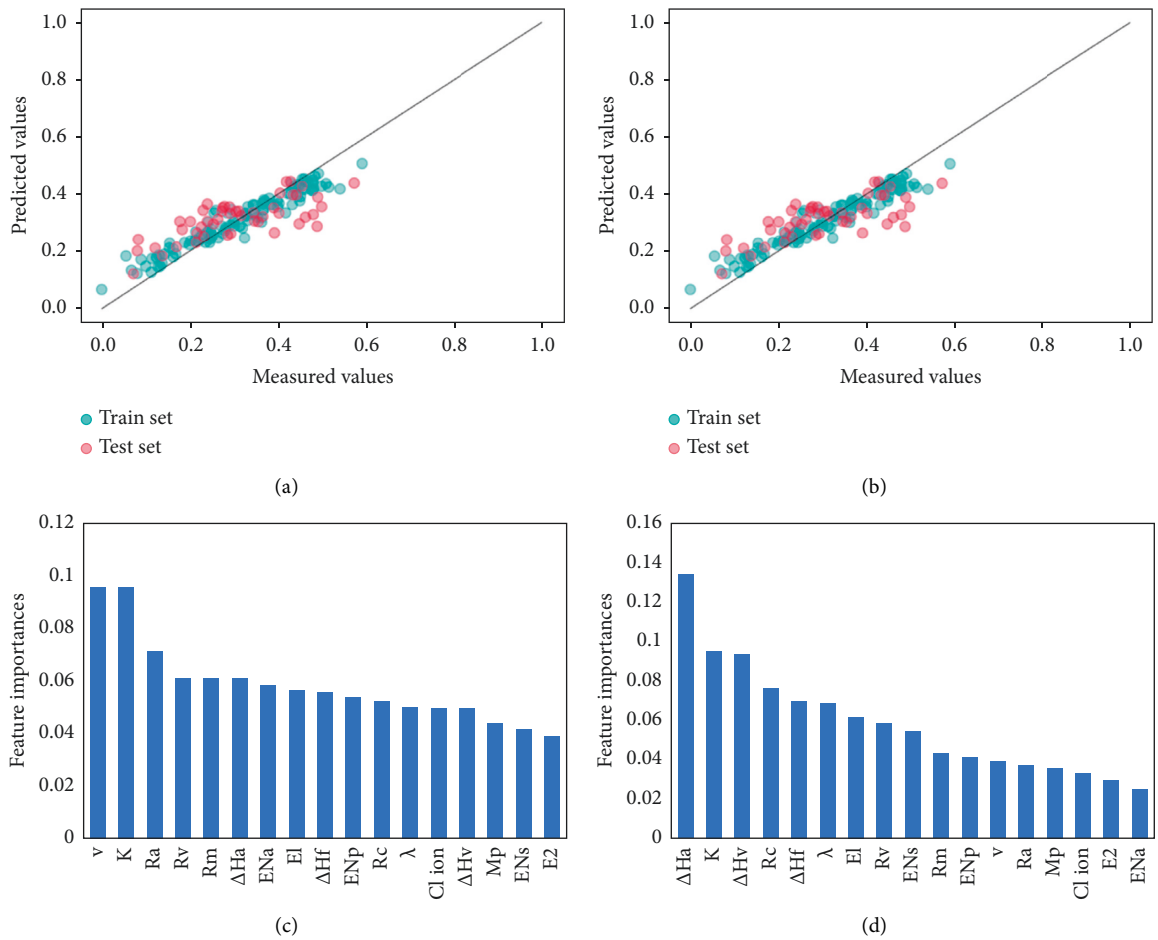

Figure 3: Predictive performance for corrosion potential and corrosion current using the RF model and corresponding characteristic importance.

The RF model evaluates the importance of each feature by measuring the influence of the feature value on the target attribute. Based on the excellent goodness of fit of the model, the prediction model mastered the law of the influence of each input on the corrosion potential and corrosion current. Thus, the model with the feature importance is considered reliable. The Al content is an important factor that affects the corrosion potential. The Mg-Al alloy had a higher corrosion potential than the pure Mg alloy [27]. $Mg_{17}Al_{12}$ (β-phase) and Al_8Mn_5 in Mg-Al alloys act as cathodes [28–30]. Moreover, iron is an impurity in magnesium alloys. Iron forms a second pure metal phase owing to its lack of solubility in magnesium alloys. Microcurrent coupling between the Mg matrix (α-phase) and this second phase leads to corrosion [31–33]. Zn and Mn have significant effects on the corrosion potential and corrosion current. Zn forms Mg_xZn_y phases and acts as a local cathode for the Mg matrix. With this process, the cathode reaction speed is accelerated, resulting in a higher corrosion rate [34, 35]. The addition of manganese can effectively reduce the Fe content in aluminum-magnesium alloys to a specific limit because the iron is isolated in AlMnFe intermetallic compounds, which significantly reduces the degree of micro-galvanic coupling [36]. Chloride ion is an environmental factor that affects the corrosion current. Chloride ions can

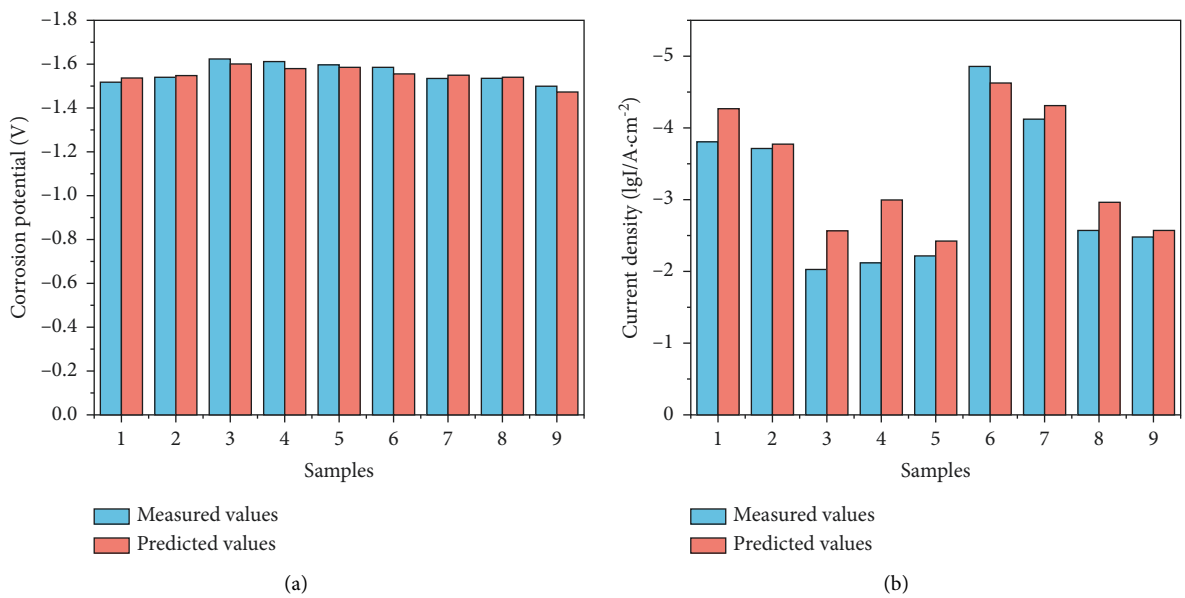

Figure 4: Comparisons of experimental measurements with predicted values using machine learning models: (a) comparison of corrosion potential results and (b) comparison of corrosion current results. Nine validation set samples were used.

dissolve the protective layer of magnesium hydroxide on the magnesium alloy, converting it to magnesium chloride, making the surface more active and more prone to corrosion [37, 38]. The importance of the input characteristics corresponding to corrosion potential and corrosion current prediction models is shown in Figure 2.

3.2. Prediction of Corrosion by Creating Feature Methods. Using the feature creation method, a new set of material features was created, and the above four methods were used to predict the corrosion potential and corrosion current. Table 5 lists the R^2 and MAE calculation results of each optimized model in the training and testing sets. The results showed that the fitting effect of RF regression was the best accuracy comparatively. Therefore, the RF model was used in the subsequent analysis.

Based on the excellent prediction accuracy of the RF model, the relationship between the corrosion potential and corrosion current is well fitted using the feature creation method. However, no specific study has proven the relationships between the corrosion potential, corrosion current, and the physical properties of these atoms. While this process faces challenges in explaining the model, the sample composition is still represented by its atomic and physical properties, which helps predict corrosion using the feature creation method [24]. The RF model and its corresponding characteristic importance are shown in Figure 3.

3.3. Generalization Ability of the Machine Learning Model. Nine rows of new corrosion data, comprising transition metal zirconium, nickel, and the rare earth element neodymium, were collected from the published literature as verification sets (Table S2) since none of the samples in our previous dataset contained three elements. We used this validation set to verify the model's generalization. After the chemical compositions of these samples were transformed into the previously selected atomic and physical parameters via the method created using the above features, the optimized stochastic forest model was used to obtain the prediction results for each sample. The methods are shown in Figure 4. The prediction model demonstrated a high level of accuracy.

4. Conclusion

This study proposed a model to predict the corrosion potential and corrosion current of magnesium alloys. After comparing different machine learning models, an RF prediction model was established. The influences of the chemical composition and environmental factors on each sample's corrosion potential and corrosion current were proved intuitively using the RF algorithm. Then, we used the feature creation method to transform the alloy composition into the specific atomic and physical parameters, which expanded the model application range. Finally, a verification set was used to confirm the high accuracy of the prediction model. Machine learning's robust data regression and data mining abilities are useful in analyzing magnesium alloy corrosion data, which could serve as a helping tool for researching magnesium alloy corrosion.

Data Availability

The data used to support the findings of this study are included within the article.

Disclosure

Zhenxin Lu and Shujing Si are co-first authors.

Conflicts of Interest

The authors declare that they have no conflicts of interest.

Acknowledgments

We thank Mr. Song for his support in this work.

Supplementary Materials

Table S1: the specific corrosion data. Table S2: nine rows of new corrosion data. (*Supplementary Materials*)

References

[1] N. Li and Y. Zheng, "Novel magnesium alloys developed for biomedical application: a review," *Journal of Materials Science & Technology*, vol. 29, no. 6, pp. 489–502, 2013.

[2] J. Chen, L. Tan, X. Yu, I. P. Etim, M. Ibrahim, and K. Yang, "Mechanical properties of magnesium alloys for medical application: a review," *Journal of the Mechanical Behavior of Biomedical Materials*, vol. 87, pp. 68–79, 2018.

[3] W. J. Joost and P. E. Krajewski, "Towards magnesium alloys for high-volume automotive applications," *Scripta Materialia*, vol. 128, pp. 107–112, 2017.

[4] J. Tan and S. Ramakrishna, "Applications of magnesium and its alloys: a review," *Applied Sciences*, vol. 11, no. 15, p. 6861, 2021.

[5] C. Zhong, F. Liu, Y. Wu et al., "Protective diffusion coatings on magnesium alloys: a review of recent developments," *Journal of Alloys and Compounds*, vol. 520, pp. 11–21, 2012.

[6] Q. Liu, W. Cheng, H. Zhang, C. Xu, and J. Zhang, "The role of Ca on the microstructure and corrosion behavior of Mg–8Sn–1Al–1Zn–Ca alloys," *Journal of Alloys and Compounds*, vol. 590, pp. 162–167, 2014.

[7] K. Gusieva, C. H. J. Davies, J. R. Scully, and N. Birbilis, "Corrosion of magnesium alloys: the role of alloying," *International Materials Reviews*, vol. 60, no. 3, pp. 169–194, 2014.

[8] T. T. T. Trang, J. H. Zhang, J. H. Kim et al., "Designing a magnesium alloy with high strength and high formability," *Nature Communications*, vol. 9, no. 1, p. 2522, 2018.

[9] J. Yang, J. Peng, E. A. Nyberg, and F.-S. Pan, "Effect of Ca addition on the corrosion behavior of Mg–Al–Mn alloy," *Applied Surface Science*, vol. 369, pp. 92–100, 2016.

[10] B. Mingo, M. Mohedano, C. Blawert, R. del Olmo, N. Hort, and R. Arrabal, "Role of Ca on the corrosion resistance of Mg–9Al and Mg–9Al–0.5Mn alloys," *Journal of Alloys and Compounds*, vol. 811, Article ID 151992, 2019.

[11] L. Wei, J. Li, Y. Zhang, and H. Lai, "Effects of Zn content on microstructure, mechanical and degradation behaviors of Mg-xZn-0.2Ca-0.1Mn alloys," *Materials Chemistry and Physics*, vol. 2020, Article ID 122441, 12 pages, 2020.

[12] Y. Song, E.-H. Han, D. Shan, C. D. Yim, and B. S. You, "The effect of Zn concentration on the corrosion behavior of Mg–xZn alloys," *Corrosion Science*, vol. 65, pp. 322–330, 2012.

[13] L. Yang, "Corrosion behaviour of AZ63 magnesium alloy in natural seawater and 3.5 wt.% NaCl aqueous solution," *International Journal of Electrochemical Science*, vol. 2018, pp. 8084–8093, 2018.

[14] N. D. Nam, M. Mathesh, M. Forsyth, and D. S. Jo, "Effect of manganese additions on the corrosion behavior of an extruded Mg–5Al based alloy," *Journal of Alloys and Compounds*, vol. 542, pp. 199–206, 2012.

[15] D. H. Cho, B. W. Lee, J. Y. Park, K. M. Cho, and I. M. Park, "Effect of Mn addition on corrosion properties of biodegradable Mg-4Zn-0.5Ca-xMn alloys," *Journal of Alloys and Compounds*, vol. 695, pp. 1166–1174, 2017.

[16] J. Wang, Y. Ma, S. Guo, W. Jiang, and Q. Liu, "Effect of Sr on the microstructure and biodegradable behavior of Mg–Zn–Ca-Mn alloys for implant application," *Materials & Design*, vol. 153, pp. 308–316, 2018.

[17] J. Ding, X. Liu, Y. Wang et al., "Effect of Sn addition on microstructure and corrosion behavior of as-extruded Mg-5Zn-4Al alloy," *Materials*, vol. 12, no. 13, p. 2069, 2019.

[18] Z. Yu, Q. Huang, W. Zhang et al., "Effect of Sn content on the mechanical properties and corrosion behavior of Mg-3Al-xSn alloys," *Materials Research Express*, vol. 7, Article ID 076505, 2020.

[19] S. Curtarolo, G. L. W. Hart, M. B. Nardelli, N. Mingo, S. Sanvito, and O. Levy, "The high-throughput highway to computational materials design," *Nature Materials*, vol. 12, no. 3, pp. 191–201, 2013.

[20] G. L. W. Hart, T. Mueller, C. Toher, and S. Curtarolo, "Machine learning for alloys," *Nature Reviews Materials*, vol. 6, no. 8, pp. 730–755, 2021.

[21] X. Wei, D. Fu, M. Chen, W. Wu, D. Wu, and C. Liu, "Data mining to effect of key alloying elements on corrosion resistance of low alloy steels in Sanya seawater environmentAlloying Elements," *Journal of Materials Science & Technology*, vol. 64, pp. 222–232, 2021.

[22] L. Yan, Y. Diao, Z. Lang, and K. Gao, "Corrosion rate prediction and influencing factors evaluation of low-alloy steels in marine atmosphere using machine learning approach," *Science and Technology of Advanced Materials*, vol. 21, no. 1, pp. 359–370, 2020.

[23] Y. Zhi, D. Fu, D. Zhang, T. Yang, and X. Li, "Prediction and knowledge mining of outdoor atmospheric corrosion rates of low alloy steels based on the random forests approach," *Metals*, vol. 9, no. 3, p. 383, 2019.

[24] Y. Diao, L. Yan, and K. Gao, "Improvement of the machine learning-based corrosion rate prediction model through the optimization of input features," *Materials & Design*, vol. 198, Article ID 109326, 2021.

[25] Webelements, "The periodic table of the elements," 2021, https://www.webelements.com/.

[26] T. Chen and C. Guestrin, "XGBoost: a scalable tree boosting system," in *Proceedings of the 22nd acm sigkdd international conference on knowledge discovery and data mining*, pp. 785–794, San Francisco CA, USA, August 2016.

[27] P. Hoyer, G. L. Angrisani, C. Klose, F.-W. Bach, and T. Hassel, "Influence of aluminium on the corrosion behaviour of binary magnesium–aluminium alloys in saline solutions," *Materials and Corrosion*, vol. 65, no. 1, pp. 23–30, 2014.

[28] M. F. Hurley, C. M. Efaw, P. H. Davis, J. Croteau, E. Graugnard, and N. Birbilis, "Volta potentials measured by scanning Kelvin probe force microscopy as relevant to corrosion of magnesium alloys," *Corrosion*, vol. 71, no. 2, pp. 160–170, 2015.

[29] M. Ben-Haroush, G. Ben-Hamu, D. Eliezer, and L. Wagner, "The relation between microstructure and corrosion behavior of AZ80 Mg alloy following different extrusion temperatures," *Corrosion Science*, vol. 50, no. 6, pp. 1766–1778, 2008.

[30] A. Bahmani, S. Arthanari, and K. S. Shin, "Corrosion behavior of Mg–Mn–Ca alloy: influences of Al, Sn and Zn," *Journal of Magnesium and Alloys*, vol. 7, no. 1, pp. 38–46, 2019.

[31] M. Liu and G.-L. Song, "Impurity control and corrosion resistance of magnesium–aluminum alloy," *Corrosion Science*, vol. 77, pp. 143–150, 2013.

[32] F. Pan, X. Chen, T. Yan et al., "A novel approach to melt purification of magnesium alloys," *Journal of Magnesium and Alloys*, vol. 4, no. 1, pp. 8–14, 2016.

[33] M. Liu, P. J. Uggowitzer, A. V. Nagasekhar et al., "Calculated phase diagrams and the corrosion of die-cast Mg–Al alloys," *Corrosion Science*, vol. 51, no. 3, pp. 602–619, 2009.

[34] N. T. Kirkland, M. P. Staiger, D. Nisbet, C. H. J. Davies, and N. Birbilis, "Performance-driven design of biocompatible Mg alloys," *Journal of Occupational Medicine*, vol. 63, no. 6, pp. 28–34, 2011.

[35] Y. Song, E.-H. Han, K. Dong, D. Shan, C. D. Yim, and B. S. You, "Effect of hydrogen on the corrosion behavior of the Mg–xZn alloys," *Journal of Magnesium and Alloys*, vol. 2, no. 3, pp. 208–213, 2014.

[36] H. Matsubara, Y. Ichige, K. Fujita, H. Nishiyama, and K. Hodouchi, "Effect of impurity Fe on corrosion behavior of AM50 and AM60 magnesium alloys," *Corrosion Science*, vol. 66, pp. 203–210, 2013.

[37] M. J. Liang, C. Wu, Y. Ma et al., "Influences of aggressive ions in human plasma on the corrosion behavior of AZ80 magnesium alloy," *Materials Science and Engineering: C*, vol. 119, Article ID 111521, 2021.

[38] M.-C. Zhao, M. Liu, G.-L. Song, and A. Atrens, "Influence of pH and chloride ion concentration on the corrosion of Mg alloy ZE41," *Corrosion Science*, vol. 50, no. 11, pp. 3168–3178, 2008.